University of Southampton

Faculty of Engineering and Physical Sciences

School of Engineering

**Unsaturated Polyester Microstructures:
Morphology and Relation to Electrical Properties by Current Sensing Atomic Force Microscopy (CSAFM)**

by

Sara Jacy Muhler

Thesis for the degree of Doctor of Philosophy

September 2020

University of Southampton

ABSTRACT

Faculty of Engineering and Physical Sciences

School of Engineering

Doctor of Philosophy

Unsaturated Polyester Microstructures:
Morphology and Relation to Electrical Properties by Current Sensing Atomic Force Microscopy (CSAFM)

by

Sara Jacy Muhler

Polymeric coatings offer a relatively simple and cost-effective method of protecting steel assets from corrosion. Without this protection, corrosion can weaken the structural integrity of the steel and jeopardise the lifespan of the asset. In some cases, corrosion can cause catastrophic failures that risk lives as well as economic and environmental damage. It has long been theorised that structural and crosslinking inhomogeneities in the cured polymer coating may represent micro- or nano-scale defects in the barrier properties of a coating, allowing the ingress of exogenous materials. This work confirms the feasibility of detecting these inhomogeneities with established analysis techniques, attempts to correlate the polymer structures found with electrical properties, understand the mechanisms that link polymer structure and electrical properties, and ultimately use this new understanding to enhance anti-corrosive coatings.

Samples of cured isophthalic unsaturated polyester are exposed to salt fog before examination using an Alicona InfiniteFocus 3D optical microscope and MAC III Agilent 5500 Atomic Force Microscope in various modes. Other studies have reported microstructural features in unsaturated polyesters; the expected structure was a three-dimensional cellular structure with microgels of unsaturated polyester connected by polystyrene branches. After only 15 minutes of salt fog exposure, the polymer began to show this structure. Current Sensing Atomic Force Microscope (CSAFM) scans attempt to correlate these structures with highly localised electrical properties but were unsuccessful. Theories of ion migration and conductivity in polymers are discussed with relation to CSAFM and a commercially available unsaturated polyester coating.

TABLE OF CONTENTS

TABLE OF FIGURES

RESEARCH THESIS: DECLARATION OF AUTHORSHIP

Print name: Sara Jacy Muhler

Title of thesis: Unsaturated Polyester Microstructures: Morphology and Relation to Electrical Properties by Current Sensing Atomic Force Microscopy

I declare that this thesis and the work presented in it are my own and has been generated by me as the result of my own original research.

I confirm that:

1. This work was done wholly or mainly while in candidature for a research degree at this University;
2. Where any part of this thesis has previously been submitted for a degree or any other qualification at this University or any other institution, this has been clearly stated;
3. Where I have consulted the published work of others, this is always clearly attributed;
4. Where I have quoted from the work of others, the source is always given. With the exception of such quotations, this thesis is entirely my own work;
5. I have acknowledged all main sources of help;
6. Where the thesis is based on work done by myself jointly with others, I have made clear exactly what was done by others and what I have contributed myself;
7. None of this work has been published before submission:

Signature: .....Date: 23 September 2020

PUBLICATION

This work has not yet been published in an academic journal. However, parts of this work have been presented at the poster sessions below:

- Improving Industrial Coatings by Mapping Electrochemical Properties. Poster presented at: Corrosion Chemistry. Faraday Discussions, Royal Society of Chemistry. 2015 April 13-15. London, UK (below, left)
- Unsaturated Polyester Microstructures: Mapping Coatings on a Nanometric scale by AFM. Poster presented at: European Technical Coating Congress. 2016 May 25-26. Birmingham, UK (below, right)

Consideration has been given to the possible publication of parts of this work in future. Potential themes include:

- Evidence of Reduced Hydrophobicity at High Film Thickness in Unsaturated Polyester Coatings
- Unsaturated Polyester Microstructure: direct visualisation by optical and AFM methods
- Mapping Inhomogeneities in Unsaturated Polyester Coatings by Atomic Force Microscope

The topics in this work are most suited for publication in Progress in Organic Coatings, however, other titles might include Polymer, Ultramicroscopy, or Surface and Coatings Technology

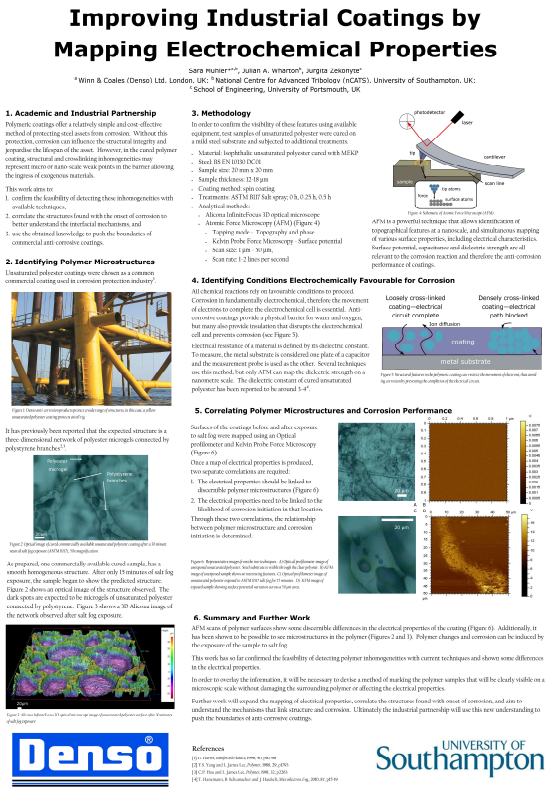

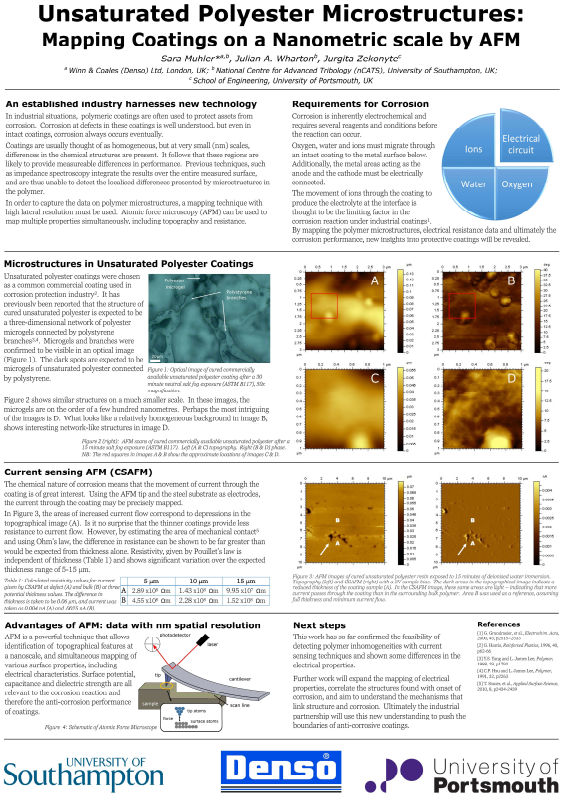

ACKNOWLEDGEMENTS

This work was undertaken part-time during 2013-2020 at the University of Southampton, UK with the funding and support of Winn & Coales (Denso) Ltd, London, UK.

It is a pleasure to thank those who make this thesis possible. Firstly, my supervisors, Dr Julian Wharton, for his guidance and patience through a long process; and Dr Jurgita Zekonyte for her invaluable insights into the temperamental workings of atomic force microscopy.

I would like to show my gratitude particularly to Stephen Crawley, Technical Director at Winn & Coales (Denso) Ltd for his support and patience, as well as to Winn & Coales (Denso) Ltd for the financial sponsorship that made this thesis possible. I am also deeply indebted my colleagues who have provided assistance, encouragement, and generally kept the lab running seamlessly during my absences.

Finally, I would also like to thank my friends and family who have offered encouragement and assistance, particularly to my sister Dr Janine Dutcher who is an inspiration and a wonderful source of information and advice

DEFINITIONS AND ABBREVIATIONS

AC:	alternating current
AFM:	Atomic Force Microscope
AM:	Amplitude modulation
ASTM:	an organisation providing voluntary technical standards and testing methods. www.astm.org (formerly the American Section of the International Association for Testing Materials, now ASTM International)
Catalyst:	a substance that increases the reaction rate without being consumed in the reaction [1]
CSAFM:	Current Sensing Atomic Force Microscopy
DMA:	dimethylaniline (see chemicals)
DSM:	manufacturer of resins and functional materials. www.dsm.com
EIS:	Electrochemical Impedance Spectroscopy
EU:	European Union
FM:	Force modulation
ISO:	International Standards Organisation www.iso.org
KPFM:	Kelvin Probe Force Microscopy (also KFM)
MEKP:	Methylethylketone peroxide (see chemicals)
NACE:	Formerly the National Association of Corrosion Engineers, NACE International is now an international body covering all aspects of corrosion management. www.nace.org
NPG:	Neopentylglycol (chemical)
OM:	Optical Microscopy
ppm:	parts per million
ppt:	parts per thousand
SEM:	Scanning Electron Microscopy
SSPC:	Formerly the Steel Structures Painting Council, SSPC (now the Society for Protective Coatings) is a “non-profit professional society concerned with the use of coatings to protect industrial steel structures”. www.sspc.org
STM:	Scanning Tunnelling Microscopy
T_g:	glass transition temperature (°C)

Thixotropy:	The behaviour of a material such that when a constant shear is applied, the viscosity is reduced over time (also called shear thinning). When the shear is removed, the original viscosity is recovered over a period of time. [2]
Topography:	a three-dimensional map of a surface
Unsaturated polyester film (or coating):	the solid produced by curing/crosslinking the resin
Unsaturated polyester polymer:	the unsaturated polyester polymer, prior to blending into a commercial resin Generally, a polyester is formed by the condensation reaction of a bifunctional alcohol (glycol) with a bifunctional acid [3]
Unsaturated polyester resin:	a commercially available mix of unsaturated polyester polymer and styrene, with or without additional additives
UP:	unsaturated polyester resin

CHEMICALS

1,2-propane glycol

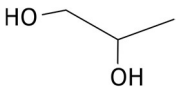

Cobalt (II) ethylhexanoate
(cobalt accelerator)

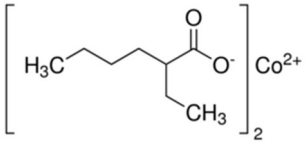

DMA (Dimethylanaline)

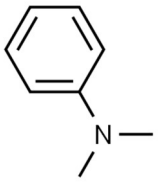

Isophthalic acid:

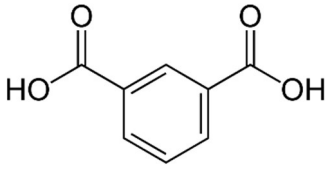

Maleic anhydride

Methylethylketone peroxide (MEKP)

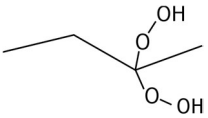

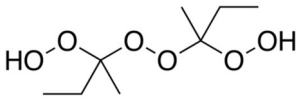

Orthophthalic acid

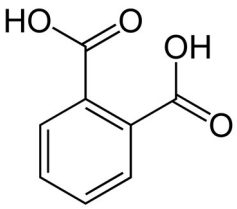

Styrene

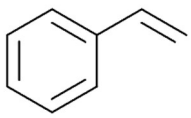

1 INTRODUCTION

1.1 CONTEXT

Global steel demand is projected to reach 1805 million metric tonnes in 2020 [4], though this has been reduced slightly from previous projections due to the global economic effects of Covid 19, the projections remain for steady growth. Steel is used in a wide range of goods and projects, including manufacturing, automotive and construction sectors [5]. This work will focus on the construction sector, primarily marine applications. Despite its popularity as a construction material, structural steel is unstable in most "real world" conditions and tends towards the reversion to its natural state of rust and ore. Corrosion can weaken the structural integrity of the material and jeopardise the lifespan of the asset. The global cost of this corrosion is often

Figure 1: An example of a commercially formulated system in the field: Orange Denso Unsaturated Polyester coating protects a support pile in a marine environment. (Photo courtesy of Winn & Coales (Denso) Ltd.)

estimated, with one recent assessment exceeding 1 trillion dollars in the US alone [6]. In addition to the financial costs of corrosion, in some cases it can cause catastrophic failures that risk lives as well as environmental and reputational damage. Due to the high potential costs of corrosion, technological efforts over many years have focused on the development of coatings that protect assets from corrosion, thus increasing the lifespan of the asset and reducing maintenance and replacement costs [7]. There are many types of corrosion and therefore many strategies to prevent corrosion- though most are outside the scope of this work.

Figure 2: Schematic of some generalised uses of coatings, including unsaturated polyesters. Zone A: Marine. Unsaturated polyesters are commonly used around marine areas including retaining walls, oil rigs, splash-zone of riser piles or jetty piles, tank exteriors, and some ship applications. Unsaturated polyesters can be used for water inlet/outlet pipes and tanks or reservoirs of water. However, tanks containing chemicals will generally require more chemical resistance and be coated with several layers of vinyl esters. Zone B: Underground. Epoxies make great protective coatings, but their tendency to chalk when exposed to light means they are best suited for underground applications (or under a UV resistant topcoat).

Polymeric coatings, including unsaturated polyester coatings based on an unsaturated polyester resin and normally cured with an organic peroxide, play a vital role in the protection of metallic materials around the world, from consumer goods to vast megastructures. Figure 1 is an example of an unsaturated polyester coating applied to piles in a marine environment. Figure 2 shows some areas of use of unsaturated polyester coatings and some other protective coating applications. Most automotive, aerospace, and domestic applications requiring performance coatings are coated in the factory whereas unsaturated polyesters are traditionally for structures

coated in the field where curing options are more limited. Zone A in Figure 2 shows some common uses of unsaturated polyester, marine retaining walls, riser piles, seawater inlets and offshore platforms. By contrast, underground areas like Zone B tend to be epoxies, or oil/wax/bitumen tape applications where UV stability is not required. Factory applied polymer coating technologies might include powder coatings, electrocoat, multilayer polypropylene, fusion bonded epoxies, heat-cured enamels, or oil, wax, and bitumen based liquids.

The advantages of polymeric coatings include a comparatively small equipment investment, relatively low expense, and the ability to apply them in a wide variety of locations and conditions. They provide a physical barrier and, in some cases, a chemical form of corrosion protection by the addition of corrosion inhibiting additives and pigments. These additions enhance the performance of the protective coating, but are often classified as hazardous to health and the environment. To ensure their protective properties over the coating lifespan, most use high quantities which can be released into the environment. Hence, novel approaches to the enhancement of corrosion protection without the use of hazardous materials are of tremendous interest to industry.

1.2 Relevance

Unsaturated polyester resins represent a large global industry. Within the composites industry, unsaturated polyester resins are the most commonly used thermoset resins, accounting for 66% of the global market in 2007 [8]. A 2013 market research study indicated that the global unsaturated polyester market was worth USD 6.54 billion in 2012. The same research estimated that figure would increase to USD 10.48 billion by 2019 [9]. In perhaps a warning on relying too heavily on market research, the same group indicated in 2018 that the global unsaturated polyester resins market was worth USD 5.7 billion in 2017, but would reach USD 7.3B by the end of 2022 of which isophthalic unsaturated polyesters would account for around 35% of the value. Another group predicted in 2019 that unsaturated polyesters would reach USD 12 Billion by 2020 and have one of the highest market shares of all thermoset resins [10]. Despite being an older technology, it is clear that unsaturated polyesters represent a large and growing market. Unsaturated polyesters are used globally for the manufacture of a wide assortment of products, including pipes, tanks, gratings and high-performance components for the marine and automotive industry. In addition to cast articles, unsaturated polyesters are a key technology for the protective coating industry.

Unsaturated polyester coatings are still widely used in industry [11] and performance is still of interest to coating formulators, manufacturers and others in the supply chain. However, many of the analytical techniques used today were not available when unsaturated polyesters were first developed. These techniques generally require significant investment that prevents its use by all but the largest coating formulators and academic institutions. In the academic sphere, interest is often focused on emerging technologies.

Historical research relied on instrumentation that could not resolve the micro and nano-scale features to investigate individual performance. These macroscopic studies contributed to the understanding and improvement of coatings by long-term performance studies and comparisons as well as some bulk studies of smaller samples in an attempt to isolate features. Although their presence could be inferred, direct measurement was not possible at that time.

Some more recent research has utilised the lateral resolution of the Atomic Force Microscope (AFM) to investigate the performance of unsaturated polyester systems. However, much of this research has focused on unsaturated polyester as part of a composite system. While this is undeniably how many unsaturated polyesters are used, the presence of the composite material is designed to affect the performance of the system and thus naturally obscures the performance of the polymer. While it is also important to consider how components work together, this work aims to consider the polymer itself. A polymer is literally a chain of monomers, if one of those links in the chain can be shown to be the weak link, future polymer development can be modified accordingly, and performance improved for both coatings and composite systems.

It has been hypothesised that extremely localised inhomogeneities in the crosslinking and structure of the polymer coating may contribute to the location of corrosion [12]. This work aims to correlate the location and type of microstructures in cured unsaturated polyester resin to the initiation of the corrosion reaction (Figure 3). Densely packed polymer chains are expected to be a stronger barrier to the water, ions, oxygen, and electrical current required for the corrosion reaction than a coating with free volume voids. Barrier properties are discussed further in Section 2.4.1.

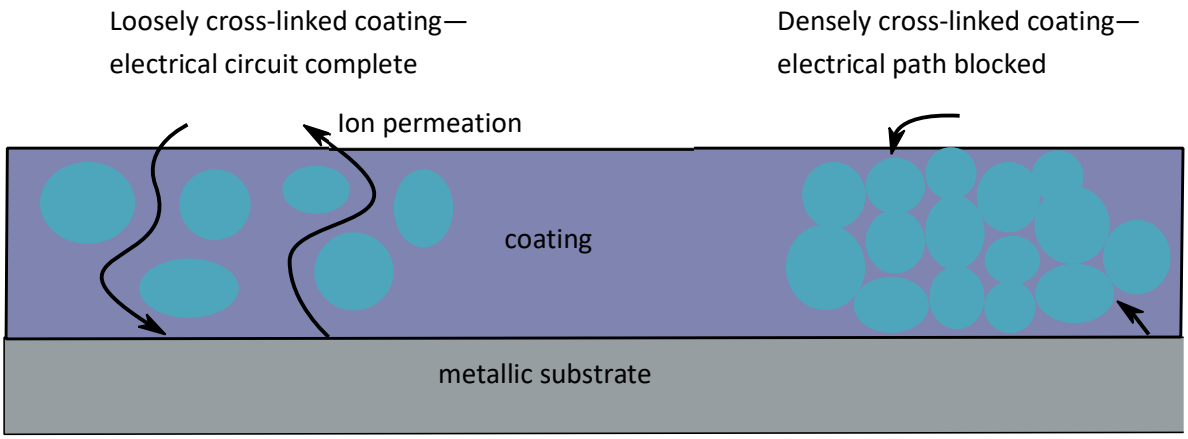

Figure 3: 2D Schematic of the possible effect of microstructure on ion diffusion through a coating.

Corrosion is an inherently electrochemical process, so the electrochemical properties of the coating are relevant to the corrosion prevention performance. It has previously been reported that reduced electrical resistance of an organic coating sample due to damage or ageing correlates with increased susceptibility of the substrate to corrosion [13]–[15]. Additionally, capacitance and dielectric constant should correlate with corrosion [16]. Electrical Impedance Spectroscopy (EIS) has confirmed the development of localised defects [17], but as the data is integrated over an entire surface [18] it is not possible to identify or map the defects with this method. By using the Atomic Force Microscope (AFM) in electrical modes, it is possible to map the electrical properties of the coating with high lateral resolution.

Current commercial unsaturated polyester coatings may be single or multiple coats, with or without primer. In order to look at the resin properties, the test system will be a comparatively thin layer of unsaturated polyester, without primer (Figure 4) or further additives. This work focuses on the resin properties, therefore additives such as anti-corrosive pigments and rheology modifiers will be avoided. It is important to use a reduced coating thickness rather than a commercially used thickness for two reasons: a thin layer will minimise the interaction of multiple microstructures above one point on the substrate, and a thin layer will presumably allow the rapid assessment of coating-substrate interactions. Commerically available coatings are designed to last years if not decades before defects occur, and this timeframe is beyond the scope of the project.

Although the simplified formulation and thin samples allow the work to progress within the time limits of the project, there are pros and cons to applying academic research to commercial coatings. A wider variety of tests and equipment are available in academic research, though modification to formulations, sample preparation, and test conditions may be required. All

deviations from commercial formulations risk having academic conclusions that are generalised. In some cases general conclusions on fundementals can be relevant across a wide range of commercial formulations. However, it is also possible for academic conclusions to be too generalised to be relevant or useful for any commercial formualtions. While it is not expected that performance could be extrapolated liniarly, the mechanisms governing the interaction of the microstructure with the environment (water, oxygen, and ions) were expected to remain relevant In retrospect, differences in the thickness and constraints from solid particles like glass flakes may have a significant affect on the way polymer microstructures form and perform.

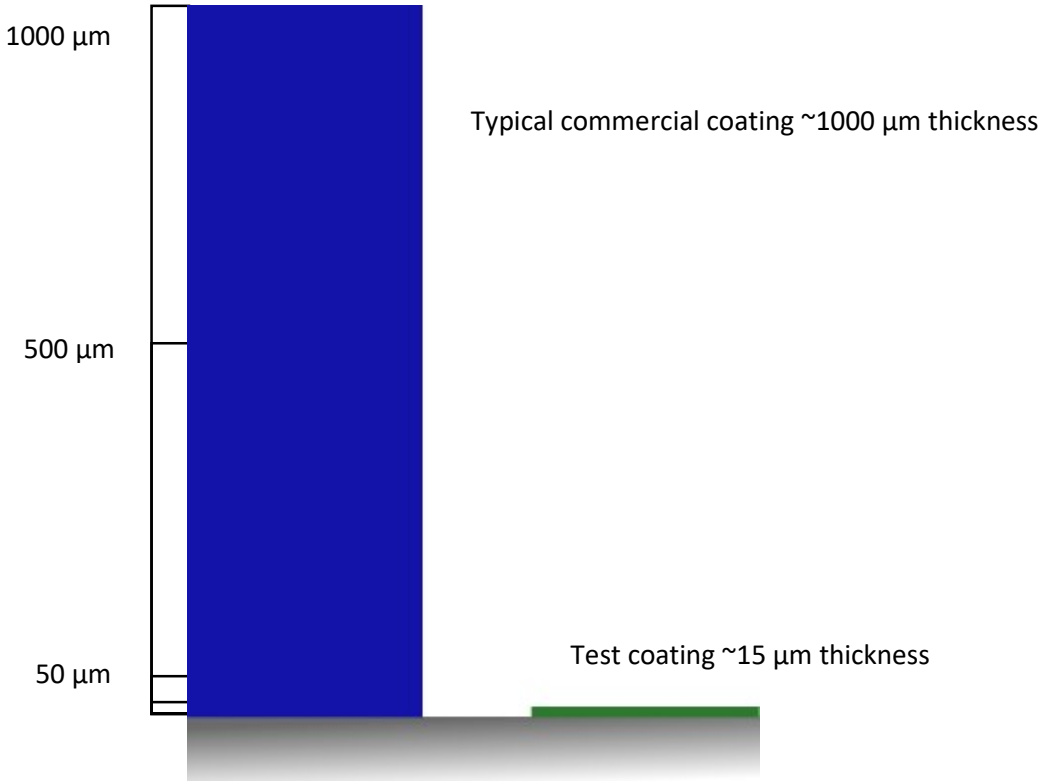

Figure 4: Schematic comparison of commercial coating thickness vs test coating thickness.

This work is comprised of several key stages:

1. Confirm the feasibility of detecting polymer microstructures with current techniques;
2. Map the polymer microstructures together with the electrical properties;
3. Understand the mechanisms that link morphology and electrical properties.

Polymers usually comprise the majority of a protective coating volume. They are therefore crucial to the overall performance of the formulated coating. It is possible to improve on a good commercial resin with carefully selected fillers and additives, but a poorly performing polymer will always be a weak link in the system. Unsaturated polyester polymers are copolymers with an additional polystyrene phase added to form the commercial resin. This complexity means that

information on the performance of the bulk polymer may not correspond to the individual components. The motivation of this work is to identify the chemical components that introduce areas of weakness in terms of corrosion protection, and therefore may be locations for the onset of corrosion. This new understanding will allow formulators to enhance anti-corrosive coatings to meet the new challenges of more extreme in-service conditions and extended durability.

1.3 Aims and Objectives

Improvement in the ability of unsaturated polyesters to protect metallic substrates from corrosion is motivated by commercial, industrial and environmental interests. As the polymer comprises the majority of the coating, it is logical to focus improvement efforts on the unsaturated polymer and commercially blended resin. Additionally, many of the latest advancements of analytical techniques have not yet been applied to the study of unsaturated polyesters.

Following on from the characterisation of the polymer network by Lee & Hsu in 1988 [19] and the understanding of how electrical properties of the coating affects the corrosion reaction by Leidheiser in 1980 [14], the ultimate aim of this project is to investigate the relationship between the microstructure and the corrosion protection of unsaturated polyester coatings. To achieve this aim, the following objectives are explored in this thesis:

- Atomic Force Microscopy (AFM) will be the main method of interrogation of the samples on a nanometre scale. Several analytical techniques will need to be used together to produce a meaningful correlation.
    - Current sensing AFM and Kelvin probe AFM will be used to investigate and map the electrical properties of the cured polymer sample.
    - 3D optical microscopy will be used to provide an overview of the sample and assist in orienting samples and overlaying correlations.
- Where it is necessary to expose the samples to environmental stresses in order to obtain a measurable response from the samples, water and sodium chloride salt solutions will be used.
- Once all of the data are collected, theories of conductivity in polymers and ion migration will be discussed with reference to CSAFM and a commercially available unsaturated polyester coating.

It is expected that several research questions will be answered during the course of this work.

1. Are polymer microstructures visible with current techniques?
    a. What methods are available and suitable for distinguishing microstructures?
    b. What sample treatments are necessary to produce consistent results?
    c. Can the unsaturated polyester be distinguished from the styrene?
2. What electrical properties can be measured in the microstructures?
3. What are the features in the microstructure (physical, chemical) that allow ion migration (and therefore corrosion) to proceed before other areas?
4. Can the electrical properties of a microstructure type or polymer chemistry be correlated with the onset of corrosion?

1.4 Overview

This thesis comprises ten sections. Background information is given in Chapter 2 and covers the industrial and academic aspects of corrosion and unsaturated polyesters. Chapter 3 explores the background and relevance of instrumentation used in this work. Specific methodology used for testing is recorded in Chapter 4. Chapters 5 and 6 present and discuss the results of the testing performed. Chapter 7 discusses and summarises results from the full thesis, with conclusions in Chapter 8 and possible future work in Chapter 9. References may be found in Chapter 10.

2 BACKGROUND

As with most modern research, this work combines a number of concepts from distinct branches of science and engineering. In view of this, some introductory information for several key areas is presented here drawing on knowledge from both academia and industry in order to establish the underlying principles necessary for the on-going investigation. Section 2.1 covers unsaturated polyesters. Section 2.2 contains a brief summary of the relevant characteristics of the carbon steel used in this work. In Section 2.3 mechanisms of corrosion protection by organic coatings are discussed. Section 2.5 gives general information on the way unsaturated polyester coatings are selected and used in industrial settings. Ways in which academic usage differs from industrial usage are highlighted in Section 2.6. Section 2.7 briefly summarises this section.

2.1 UNSATURATED POLYESTERS

While polyesters as a whole are a very common type of polymer for a wide variety of uses, unsaturated polyesters represent a much smaller subsection. Additionally, the polymer goes through several stages during this work, so the following nomenclature will be used to help differentiate where necessary. 'Unsaturated polyester polymer' refers to the polymer itself before it is blended into a commercial resin. 'Unsaturated polyester resin' denotes to the commercially available mix, including styrene, before it is cured. 'Unsaturated polyester film' (or coating) means the solid produced by curing (i.e. crosslinking) the resin.

2.1.1 Commercial development

Unsaturated polyester resins have wide acceptance and potential for growth due to their proven performance over the past 70 years. Unsaturated polyester resin technology was patented in 1942 by Cyanamid Company, USA [20]. Demand for metal outstripped supply during the war, so unsaturated polyesters found use as composites in marine and aviation industries. Over the years, the use of unsaturated polyesters expanded into mouldings, pulltrusion, and coatings. Each of these new industries came with technical challenges which ultimately pushed the boundaries of what could be achieved with unsaturated polyester resins [21]. Over 1000 patents relating to various aspects of unsaturated polyesters have been granted [22].

In the late 1940s vinyl esters were introduced [6][7][24], though they would not be commercialised until 1965 [25]. By using a bisphenol A condensation polymer with methylmethacrylate acid as a cap end, the hydrolytic stability was improved over previous unsaturated polyester polymers [26]. Further developments included reduced styrene levels and

flame retardancy [11][27]. Due to cost pressures, unsaturated polyesters are still chosen over vinyl esters in all but the most demanding applications.

In order to increase curing rates and properties to commercially valuable levels, unsaturated polyester resins are generally cut with styrene monomer; this brought additional challenges. Prior to 1947, unsaturated polyester resins were frequently shipped in dry ice to prevent the premature reaction of the styrene monomer [22]. This disadvantage was initially overcome in 1944 by adding a small amount of a blend of selected phenolic material and a base [28]. This stabilization of the styrene allowed the cost of storage and transportation to decrease considerably.

By modifying the components of the polyester polymer, scientists were able to alter the properties of the resin itself. Using isophthalic acid instead of orthophthalic acid improved the resistance to degradation caused by water [29]. Orthophthalic acid has a solubility in water of 5.74 g L^{-1} at 20 °C [30] whereas isophthalic acid has a solubility in water of only 120 mg L^{-1} at 25°C [31]. The reduced solubility of the isophthalic acid reduces the hydrophilicity caused by residual monomers and is expected to reduce monomer washout when exposed to water as well.

The addition of certain copolymers have been shown to increase the toughness and flexibility of the cured polymer [32][33][34]. As with any commercial product, financial pressures are ever-present. However, in some cases, cost of the system could be offset by longer lifespans or reduced maintenance. A thorough understanding of performance capabilities is essential for making the case to the customer. In addition to understanding the limits of current products, every producer aims to improve the performance of their products – giving them an edge in the marketplace. For example, as industry becomes more global there is demand for products that work in more challenging climates and environmental conditions.

2.1.1.1 *Legislative situation*

Historically, each country would make its own regulations regarding hazardous chemicals. Although the UK introduced a series of statutes beginning in 1993 on Chemical Hazards Information Packaging and Supply (CHIP) in line with the European Union, the United States relied on its own system, Toxic Substances Control Act (TSCA). These systems were substantially different, with the USA taking the approach of assuming all existing chemicals did not produce undue risk and requiring the registration of new chemicals not already listed. In this system, the burden of proof of potential harm lies entirely with the Environmental Protection Agency (EPA).

The TSCA system was reformed in 2016 with a risk-based approach and prioritizing evaluation of existing chemicals.

As far back as 1992, the United Nations began discussing the need for harmonisation in the classification of chemicals at the United Nations Conference on Environment and Development (UNCED, 1992 - Chapter 19 of Agenda 21). The first revision of the Globally Harmonised System (GHS) was published in December 2002 and is updated every two years. Though not a legally binding treaty, the GHS forms a framework from which countries adopt criteria and endpoints as desired. Unfortunately, this "pick-and-mix" approach has not yet resulted in the harmonisation of classification originally envisioned and some products will still have vastly different classifications in different jurisdictions (Figure 5). However, pictograms and phrases are generally uniform and physical classifications generally follow the European Agreement concerning the International Carriage of Dangerous Goods by Road (ADR).

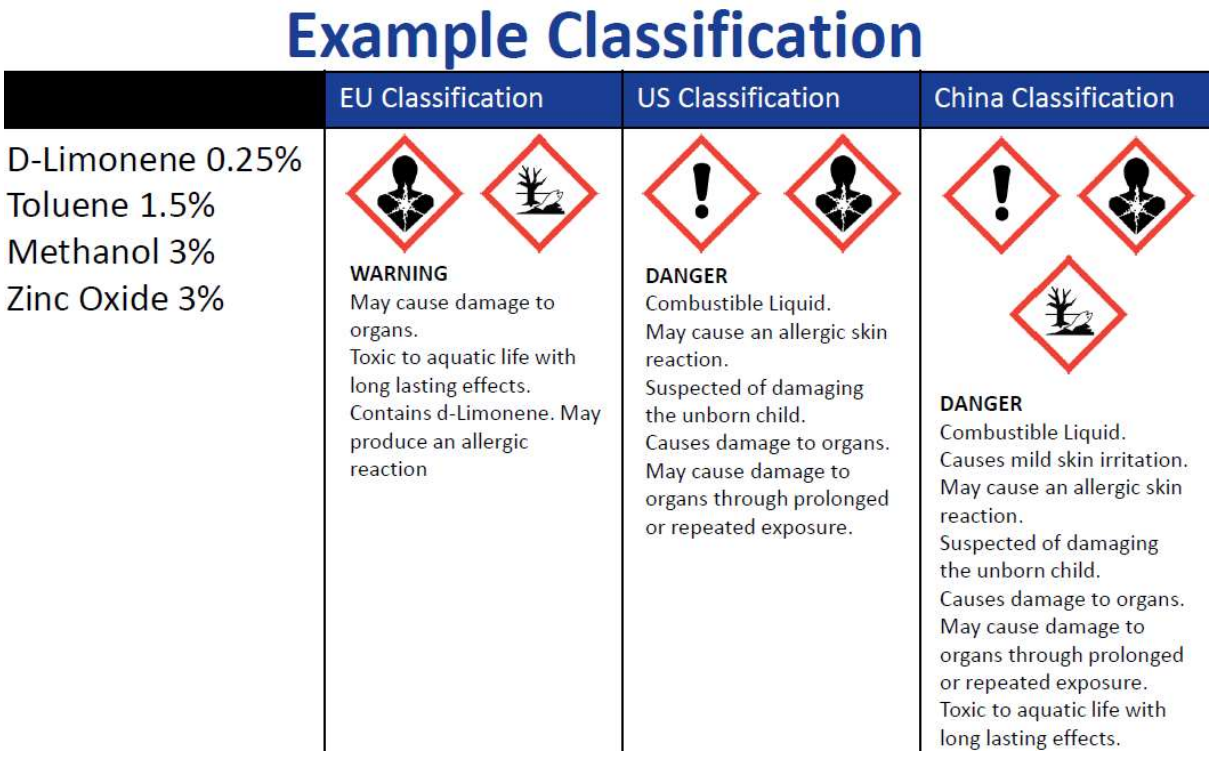

Figure 5: Example mixture classified in three GHS jurisdictions. Note differences in pictogram, signal word, and hazard statements in each jurisdiction. Courtesy of Safeware Quasar (now UL) [35]

The European Union implemented the GHS framework within Regulation (EC) No 1272/2008 of the European Parliament and of the Council of 16th December 2008 on classification, labelling and packaging of substances and mixtures (CLP). In the EU, this legislation is implemented alongside Regulation (EC) No 1907/2006 of the European Parliament and of the Council of 18th December 2006 concerning the Registration, Evaluation, Authorisation and Restriction of Chemicals (REACH)

which established a European Chemicals Agency (ECHA) and introduced a broad registration scheme. In contrast to the TSCA scheme, REACH puts the onus on chemical producers and importers to prove chemicals do not present undue risk. These two pieces of legislation are closely related and form the foundation of chemical regulation in Europe.

Under REACH [36], the EU has begun to restrict the use and limit the exposure to harmful chemicals. Though many are classified as hazardous, none of the main components of unsaturated polyesters are yet restricted for use in coatings [37]. This is a shifting situation and many companies are developing less hazardous solutions in advance. Cobalt compounds are commonly used as promotors in the cure. DSM has recently patented the use of some copper compounds, avoiding the use of the heavy metal [38] while AkzoNobel has commercially available promotors using copper, manganese and iron [39]. Additionally, the harmonized classification of styrene in the EU, a major component of nearly all unsaturated polyester coatings, has been amended to include "suspected of damaging the unborn child" [40] and other hazard statements have followed. The industry has responded by developing styrene-free unsaturated polyesters [41]. Despite these technological advances, there are still fundamental challenges to overcome. For instance, coating inhomogeneity has been shown to exist in free-radical cured polymers, such as unsaturated polyesters [42]. Changes in the polymer formulation have also been shown to result in variations in the molecular polarity – causing differences in the resulting polymer structure [43] and ultimate performance.

2.1.2 Resin production

Commercially, unsaturated polyester polymers are produced by a condensation reaction of a di-acid and a glycol. Various reagents may be used depending on the properties desired, but some common ones include propane diol, ethylene glycol, and isophthalic or orthophthalic acid [29]. The acid or anhydride is reacted with the diol to form an ester (Reaction 1). This condensation reaction produces water, which may be removed to control the hydrolysis of the ester. From a commercial standpoint, the water must be removed for the reaction to progress [44]. By using di-acids and glycols, the esterification reaction can proceed beyond the single reaction (monoester) shown in Reaction 1 to produce polyester chains. The formation of monoesters proceeds at 60°C to 130°C, while the polycondensation occurs above 160°C [25]. Progression of the polymerisation in Reaction 1 would result in a polyester, but without the unsaturation required for crosslinking later. In order to produce an unsaturated polyester, another reagent must be introduced to provide double bonds in the backbone of the polymer [45]. The commercial resin used in this work is understood to use maleic anhydride for the unsaturation. However, other molecules may also be used. To avoid unwanted gelling, unsaturated polyester polymers are generally limited to

a molecular weight of around 3000 g mol^{-1} [25], which equates to approximately 14 repeating units. Figure 6 shows a possible unsaturated polyester molecule resulting from the polymerisation of isophthalic acid, maleic anhydride and propylene glycol.

Reaction 1: Esterification of isophthalic acid with propylene glycol.

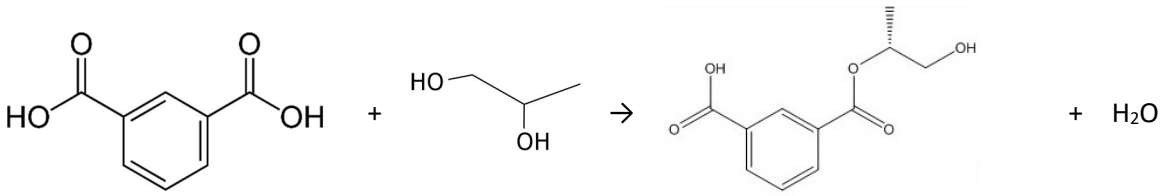

The choice of reagents can affect the properties of the final resin and cured coating. One of the most well-known differences, is the performance variation between orthophthalic and isophthalic acid [29]. The orthophthalic acid can be introduced as an anhydride, which reduces the reaction time and thereby the cost. However, the orthophthalic acid is soluble in water. Any unreacted monomer would remain soluble, contributing to osmotic pressure differences thereby causing blisters and reducing corrosion protection [26]. Additionally, any soluble components might be washed out of the cured film, leaving voids through which corrosion reactants may enter. For this work, commercially available isophthalic unsaturated polyester resin is used.

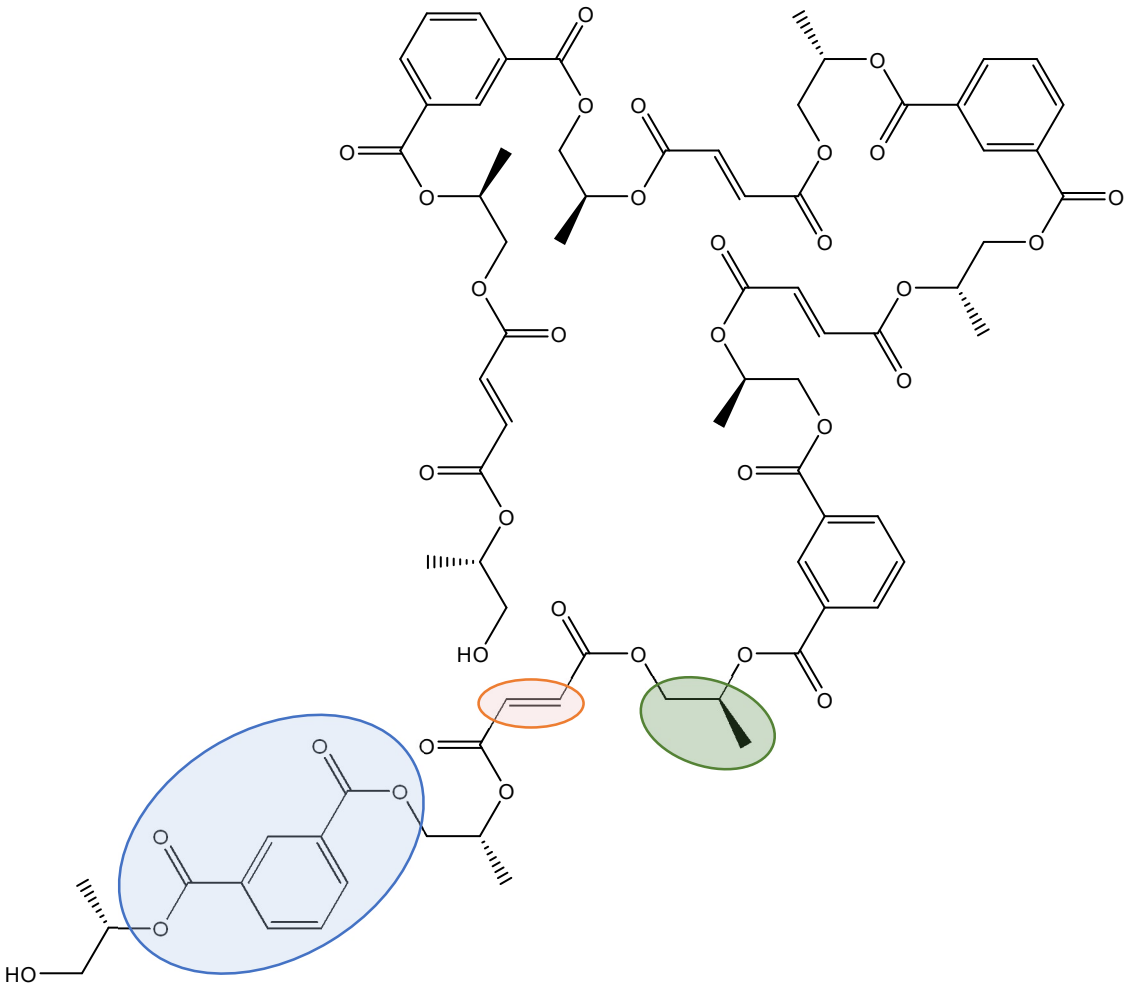

Figure 6: One possible chemical structure of an unsaturated polyester molecule produced from the polymerisation of isophthalic acid, maleic anhydride and propylene glycol. The unsaturation (example highlighted in orange) that gives these resins their common name (i.e., unsaturated polyesters) is produced by a ring-opening step during the reaction with maleic anhydride. In contrast, the isophthalic acid monomer (example highlighted in blue) retains its ring structure after polymerisation. One instance of carbon atoms from the propylene glycol are highlighted in green.

Unsaturated polyester polymers are rarely used on their own due to their low T_g – around 25°C [46]. Their soft and ductile nature makes unsaturated polyester polymers unsuitable for most industrial applications; fortunately, the introduction of styrene monomer has a dramatic effect. In general, increasing the content of styrene monomer increases the T_g of the final polymer [47]. In commercially available resins for industrial use, the typical styrene content is around 40-45%. These figures vary due to target viscosity, though additional variation occurs post-production – primarily due to evaporation [48]. Styrene content has been found to affect several physical properties of the cured film. In addition to the variation in T_g, styrene has been found to affect the storage modulus, crosslink density and volumetric contraction on curing [48] as well as the size of microgels formed during curing [19]. In some cases, the lack of a full cure can make styrene behave more as a plasticiser than copolymer [49].

Additionally, the chain length and quantity of the reagents used can be tailored to produce an unsaturated polyester backbone with the desired proportion of reactive sites which affects the cross-link density and hence the macroscopic properties of the cured film. Table 1 shows some properties of commercially available unsaturated polyester resins. It is clear from this data that the performance characteristics of unsaturated polyesters vary, and must be selected with the project parameters in mind. Simply specifying an Isophthalic unsaturated polyester from a particular supplier might result in a resin that resists heat up to 120°C or only 65°C. This wide range of properties should not be considered a disadvantage as it allows customers greater scope of choice within the cost/performance balance.

Table 1: Typical properties of various unsaturated polyester resins, as cured (note: not all data is provided by manufacturers for all products; Resin types: Ortho – produced with orthophthalic acid, Iso – produced with isophthalic acid, NPG- produced with neopentylglycol)

Brand	**Reichhold (Polylite)**				**Polynt (Norsodyne)**				**DSM**			
Product	**480**	**250**	**680**	**720**	**23100**	**46100**	**36238**	**44281**	**P69** [50]	**1717** [51]	**0288** [52]	
Type	Ortho	Iso-NPG	Iso	Iso	Ortho	Iso-NPG	Iso	Iso	Ortho	Iso	Iso	
Styrene content	34	43	34	34	-	-	-	-	45	45	-	%
Tensile strength	70	70	45	78	60	60	70	70	75	65	75-80	MPa
Tensile elongation	3	2.5	1.4	3.5	1.8	2.1	4.1	2.6	3.4	3.5	2.5-2.6	%
Tensile modulus	3700	3600	3800	3650	4050	3330	3633	3530	3800	3600	3800-4100	MPa
Flexural strength	135	140	90	140	70	125	112	140	120	120	-	MPa
Flexural modulus	3600	3500	3700	3500	3250	3725	3125	3460	3700	3600	-	MPa
Heat distortion temp.	86	102	125	86	72	92	93	95	90	105	65-75	°C

2.1.3 Coating formulation

Resins are rarely used alone. Generally, they are formulated into coatings with other materials that fall into four broad categories; resin, solvent, pigments, and additives [53]. Details of typical systems are outlined in this section. Much of the recent work published relates to composite systems. While these are closer to the actual usage, the addition of fibres and other ingredients can mask the performance of the polymer. By returning to the fundamental base structure of the system and focusing on the polymer performance, it is envisioned that the whole system will be improved.

2.1.3.1 *Resin*

As mentioned in Section 2.1.2, the commercial unsaturated polyester resin is already a copolymer blended with styrene. The monomers chosen and the styrene content contribute to the properties of the resin as a whole. However, there is little data available showing the effects of each chemical species. The absence of mapping and modelling data from the cured polymer has left a gap in the knowledge. The "weak link" in unsaturated polyester resins is unknown.

In some cases, the resin (also called the binder) is blended with other polymers to enhance the properties. Unsaturated polyesters are occasionally blended with more flexible polymers to improve elasticity. However, this can reduce the chemical resistance and other properties as increasing flexibility often reduces the crosslink density.

2.1.3.2 *Solvent*

Many coatings rely on solvent to reduce the viscosity during application. For unsaturated polyesters, the styrene monomer behaves as a solvent to reduce viscosity, but it is generally considered a reactive diluent as most of it reacts to become polystyrene and copolymers. In this work, additional styrene is not added to optimise viscosity as styrene content is known to affect the properties of the cured resin.

2.1.3.3 *Pigments*

Pigments are a wide group, generally comprising small solid particles. The most well known group of pigments are colourants; however, pigments may also be functional. For example, zinc phosphate might be added to improve the corrosion performance or aluminium tri hydride might be used to improve the flame resistance. Fillers are also generally considered to be part of the pigment category. Depending on the formulation, several colourants and even multiple functional pigments or fillers might be used. Unsaturated polyesters are often used with glass flake primarily to slow water ingress through the coating.

2.1.3.4 *Additives*

The category of additives generally comprises all the materials added in small quantities (typically <5 wt.%) to make relatively small adjustments to the coating performance. As such, this category can have some overlap with functional pigments. Additives represent a wide range of chemistry and attributes. Some of the more common additives include wetting agents, defoamers, and rheology modifiers.

2.1.3.5 *Model system*

In this work, the resin is tested with a minimum of extra materials- just what is required to cure the resin (Cobalt (II) ethylhexanoate, dimethyl analine, and methylethylketone peroxide). As many of the additional raw materials in a formulation are generally designed to improve the corrosion performance, any additional components would change the results and lengthen the testing time by an unknowable amount. The aim of this work is to determine the performance of unsaturated polyester resin without the obscuring effect of other additions.

Unfortunately, restricting the work to the polyester resin does introduce some other challenges. Many researchers who work with thin polymer films rely on solvents to reduce the viscosity and achieve a thinner film during spin coating. In this case, adding solvents or additional styrene would change the microstructure and invalidate the results for the commercial resin.

2.1.4 Curing

2.1.4.1 *Formulation and Reaction*

In contrast to the condensation polymerisation used to form the resin polymer, curing uses a free-radical copolymerisation of the unsaturated polyester and styrene monomer [54]. Although a range of organic peroxides can be used to initiate the cure of unsaturated polyester resin, methylethylketone peroxide (MEKP) is widely used commercially, and will be used in this work. However, pure MEKP is explosive, so all commercially available MEKP is desensitised (see **Aside 1** [55]). In this work, the MEKP is desensitised with aliphatic esters. In addition to the MEKP, accelerators, promotors, and inhibitors can be used to control the reaction kinetics.

Colloquially, organic peroxides are often imprecisely referred to as catalysts. In this context, organic peroxides are not true catalysts as they are consumed in the redox reaction;

Aside 1: Properties and Hazards of Organic Peroxides [55]

"Organic peroxides are organic chemicals which contain the unstable -O-O peroxy linkage in their molecular structure. They are highly reactive, combustible and thermally unstable substances which may undergo self-accelerating decomposition. They also possess oxidising characteristics and will react, often violently, with organic matter and chemical reducing agents. A limited number of liquid compositions are low flash point, highly flammable liquids."

"In the pure state some are detonable and easily initiated. These properties are suppressed or removed by dilution or phlegmatisation (desensitisation) with liquids such as water and phthalates. Even so, commercially available organic peroxides are capable of self-heating and runaway decomposition."

however, they may be referred to as initiators as they initiate the curing reaction. The unstable peroxy linkage in the organic peroxide is broken (either by a metal promotor, as in Reaction 2, or by heat and ageing) resulting in free radical species which initiate the crosslinking reactions. Although organic peroxides will eventually initiate the curing reactions alone, it may take elevated temperatures or many days. These reaction rates are impractical for commercial use. In order to increase the reaction kinetics at room temperature, one or more promotors are used. As mentioned previously, cobalt compounds are often used to promote ambient curing. In this system, the role of the promotor is to accelerate the redox degradation of the organic peroxide (Reaction 2). Paradoxically, as the cobalt is not consumed in the reaction, it could be considered a catalyst.

Reaction 2: Redox degradation of the organic peroxide [56]. "R" in chemical reactions commonly denotes a general organic structure where variations may be possible. In this work, methylethylketone peroxide was used.

1) $\mathrm{ROOH} + \mathrm{Co^{2+}} \rightarrow \mathrm{RO}^{\cdot} + \mathrm{OH^{-}} + \mathrm{Co^{3+}}$

2) $\mathrm{ROOH} + \mathrm{Co^{3+}} \rightarrow \mathrm{ROO}^{\cdot} + \mathrm{H^{+}} + \mathrm{Co^{2+}}$

There are many MEKP solutions commercially available to control cure speeds and ensure optimum performance for a wide variety of chemistries and conditions. For example, the MEKP designed for vinyl ester resins are mostly MEKP dimer to avoid the foaming caused by MEKP monomer and hydrogen peroxide [57]. The MEKP used in this work is a common commercial grade comprised of the dimer as well as the monomer and a small amount of hydrogen peroxide.

2.1.4.2 *Cured Structure*

Considerable work has been done to characterise the curing and structure of these polymers. There are six possible crosslinking structures: *(i)* intermolecular unsaturated polyester with a styrene bridge (Figure 7), *(ii)* direct intermolecular crosslinking (Figure 8), *(iii)* intramolecular crosslinking with a styrene bridge (Figure 9), *(iv)* direct intramolecular crosslinking (Figure 10), *(v)* branch growth, *(vi)* and styrene polymerisation (Figure 11) [19][58][59]. Using reaction kinetics, it has been shown that polyester microgels form first, then a styrene network forms around the microgels [19] (Figure 12) which may be a result of phase separation during the cure [60]. It is unclear from the literature if this curing mechanism leaves gaps in the film between the microgels and polystyrene bridges. Voids are most likely to be formed at the end of the cure, when the polymers have the lowest mobility due to crosslinking that has already occurred. Sample preparation methods that fracture and wash the samples cannot be relied on to answer this question, but large gaps are not expected in a protective coating that has been used commercially for many years. Previous work has relied heavily on the use of Scanning Electron Microscopy

(SEM). While this is able to achieve the resolution required (micrometre scale), the extensive sample preparation required (fracturing and coating with conductive metal) may have distorted the microstructures found – especially for the partially cured samples. Additionally, no information regarding the individual performance of the structures is provided.

Multiple mechanisms have been proposed: ring formation by intramolecular reactions, reduced reactivity of pendant vinyl groups, and steric hindrance of the vinyl groups due to microgel formation [61]. However, temperature has been shown to influence reactivity of the components; at room temperature styrene monomer plays less of a role at the outset of the reaction, whereas, at 90°C the difference is much smaller [62]. This may be due to an increased activation energy for high styrene content [47]. Measuring the effect of temperature on the cure is complicated by the significant exotherm of the curing reaction. Though the cure has been monitored by FTIR [62] and Raman Spectroscopy [63][64], the microstructure evolution has not been directly observed *in situ*.

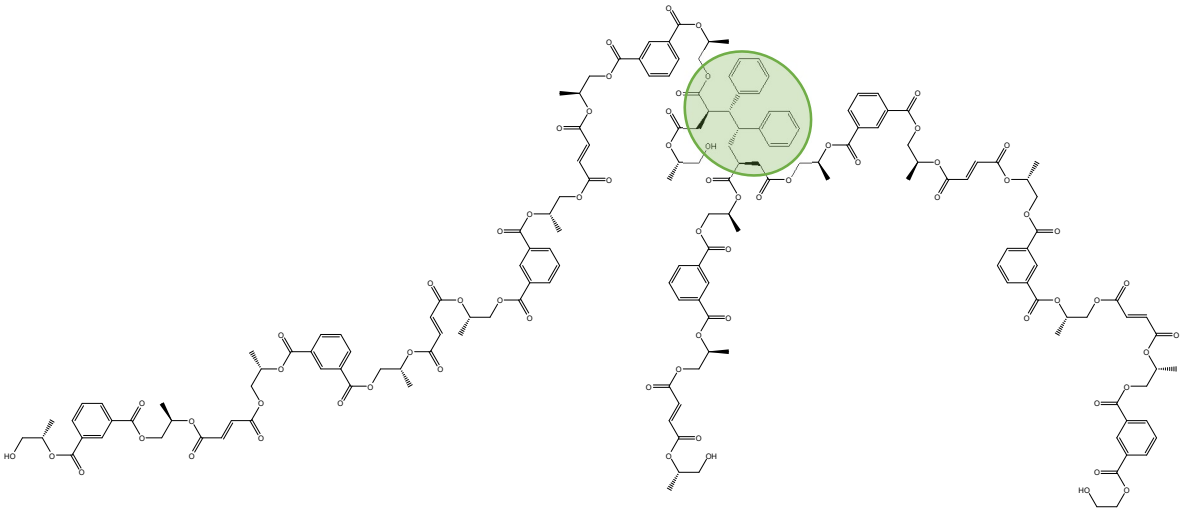

Figure 7: Two unsaturated polyester molecules crosslinked by a styrene bridge (2 molecules). The crosslinked area is circled in green.

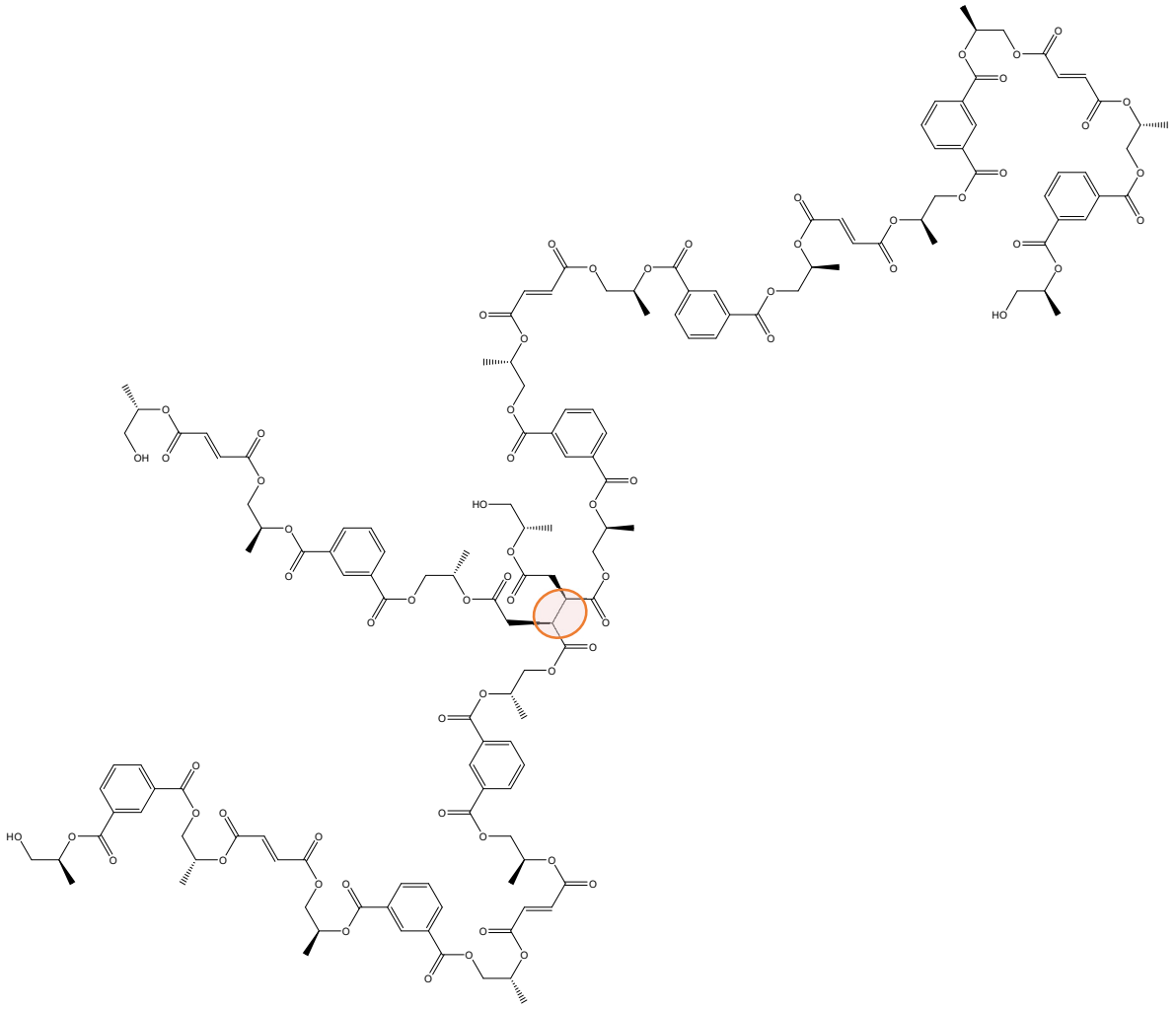

Figure 8: Direct intermolecular crosslinking of two unsaturated polyester molecules. New bond is highlighted in orange

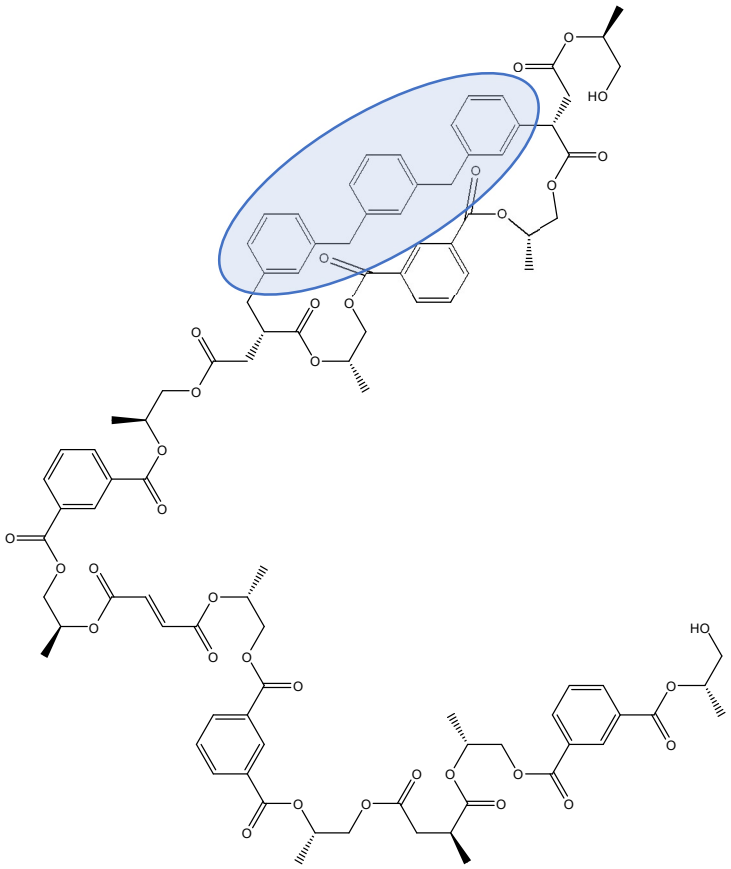

Figure 9: Intramolecular crosslinking of an unsaturated polyester molecule via a styrene bridge. The styrene bridge (3 monomers) is highlighted in blue.

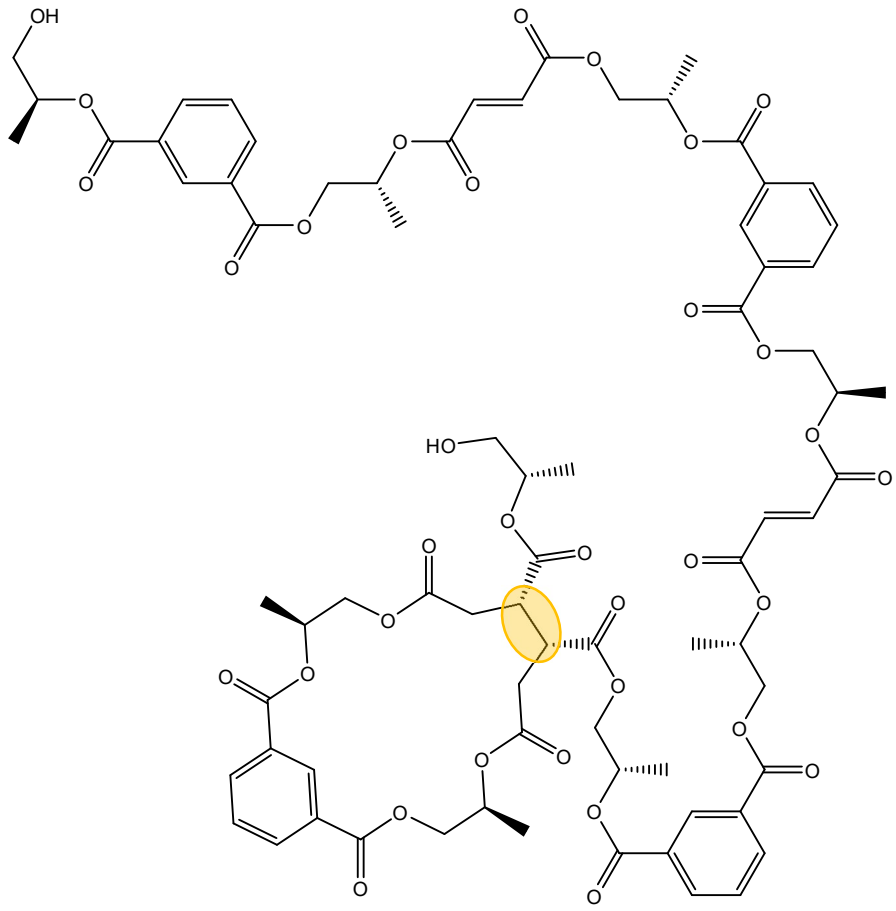

Figure 10: Direct intramolecular crosslinking of an unsaturated polyester molecule. Crosslinked area is highlighted in yellow.

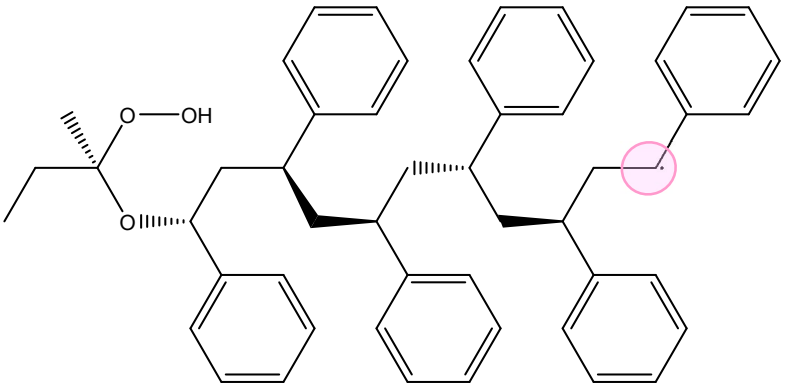

Figure 11: Polystyrene with six monomers. The MEKP from the free radical generation can be seen on the left, and the latest free radical is highlighted in pink.

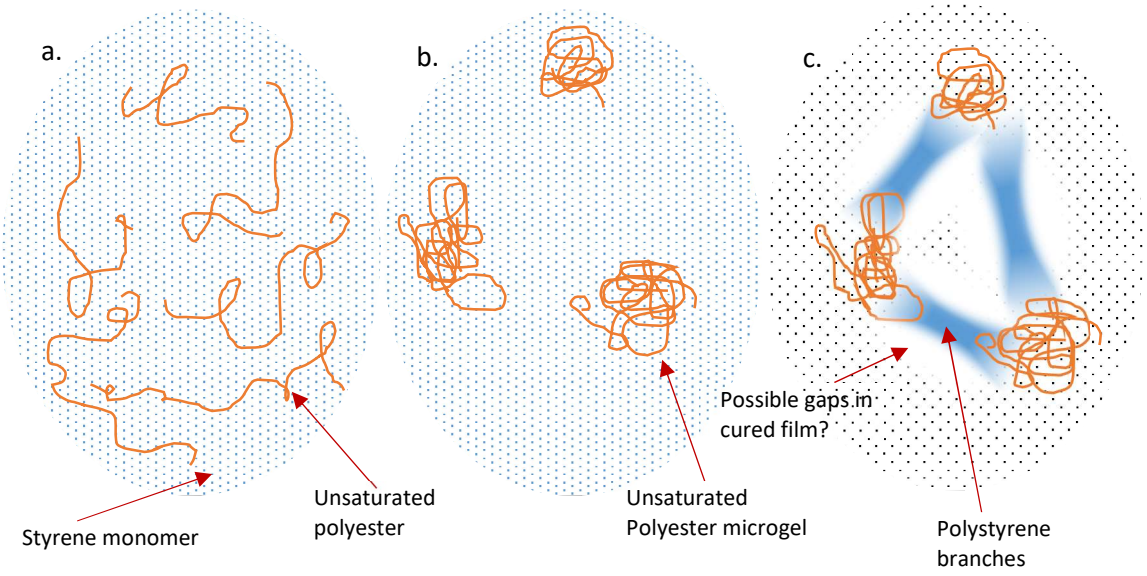

Figure 12: Schematic of the cured polymer. (a.) Unsaturated Polyester resin: chains of unsaturated polyester (orange) surrounded by styrene monomer (blue dots). (b.) Unsaturated polyester (orange) form concentrated microgels first. (c.) As the cure progresses, the styrene monomer (shown as blue circles) polymerise to form polystyrene branches. It is not clear if this curing process leaves gaps in the film between the microgels and polystyrene branches.

Variations in the curing reactions can have measurable effects on the properties of the resultant polymer [65]. When it was shown that temperature changed the reactivity of the styrene, it was also revealed to have a large effect on the tensile strength and size of the microgels [62]. These differences in the microstructure may contribute to the differences in T_g. Polystyrene has a higher density of aromatic rings which restrict the molecular movement, thus increasing the temperature required to transition from vibrational movement to rubbery movements [3]. Size, shape, and distribution of the different polymers could affect the final properties. Because unsaturated polyester itself is comparatively soft at room temperature (T_g around 25°C), styrene contributes a great deal to the final properties of the polymer. Indeed, it has been concluded that styrene concentration has a greater effect on the microstructure of the polymer than variations in the composition of the unsaturated polyester [46]. These microstructures have been shown to be affected by styrene content and curing temperatures [62]. Additional work has been done to demonstrate the effect of styrene content [43][44] and curing temperature [62] on the mechanical properties. Little work has been done to determine the relationship between the morphology and the properties of resins [48]. While mechanical information is important, it is only part of the complete performance required of anti-corrosive coatings.

2.1.5 Summary

Though the curing of unsaturated polyester resins has been studied by modern techniques, there are fewer data on the open published literature relating the type and formation of the

morphologies of polymers and the ultimate performance of the coating. Recent advances in optical microscopy (OM) and atomic force microscopy (AFM) have allowed additional insight into the nano- and micro-structures formed during polymer curing. Serre, Vayer & Erre identified microgels, nanogels and voids by tapping mode AFM [66] after fracturing and soaking in dichloromethane. These were connected by aggregated nanogels. However, the chemical nature of these was not determined. There is still work to be done to characterise the structures and link them with localised performance.

2.2 Carbon Steel

Steel is an alloy primarily made up of iron with up to around 1.5% carbon [1]. A wide range of steels can be produced by varying the amount of carbon and other elements. In general, higher carbon content indicates more brittle steel. In structural projects, where a large amount of steel is required, carbon steel is generally chosen for its low cost [67]. BS EN 10130 DC01 steel was chosen for this work as it is a basic carbon steel without large amounts of elements that improve the corrosion resistance. The chemical composition as dictated by the standard is a maximum of 0.12% carbon, 0.045% phosphorus, 0.045% sulphur and 0.60% manganese by ladle analysis [68]. Generally, carbon and phosphorus are thought to have a positive effect on corrosion resistance, whereas manganese is neutral and sulphur has a large negative effect on corrosion resistance [69]. Specific rates of corrosion and effects of alloy elements may vary with environmental conditions [70].

2.3 Corrosion

There are many types of corrosion that occur in different conditions, but only those that are relevant to this work will be presented here– namely aerobic corrosion in atmospheric or submerged conditions.

As with all structural materials, considerable energy is used to convert the raw iron ore to steel. This conversion imbues the materials with necessary and desirable properties, but introduces thermodynamic instability [71]. Steel is unstable in most “real world” conditions and tends towards the reversion to its natural state of rust and ore. The chemical reaction of steel with oxygen and moisture to form hydrated oxides is generally called corrosion. There are many strategies employed to control (i.e., reduce to an acceptable level) this corrosion. Control of corrosion by means of organic coatings forms the basis of this work and will be discussed in Section 2.4 and throughout, while this section covers the basic concepts of corrosion.

2.3.1 Atmospheric and Aerobic corrosion

Corrosion is an electrochemical process requiring an anode and cathode to be electrically connected. Real-world corrosion bears little resemblance to the standard laboratory electrode set-up. In practice, the metal surface becomes both the cathode and the anode in localised areas. Though these electrochemically active areas may be relatively distant, they must be connected by an electrolyte. Therefore, an aqueous environment with water and soluble ionic species (an electrolyte) are often necessary for corrosion to occur. Although chemical reactions can occur anaerobically, oxygen is also necessary at the anode for the oxidation reaction that results in the familiar red corrosion products. Aerobic corrosion is more energetically favourable, and will occur preferentially over anaerobic corrosion [72].

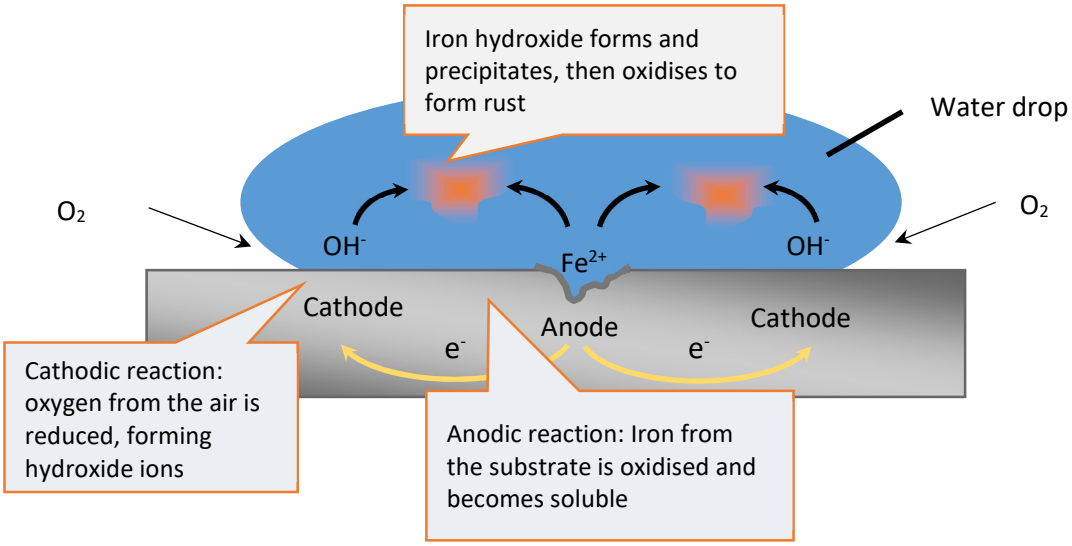

Figure 13: Diagram of aerobic corrosion [1]. Once the electrical circuit is connected, the corrosion reactions are favourable and proceed. At the interface of the electrolyte and steel, oxygen is dissolved into the electrolyte, producing hydroxide ions and carrying electrons away from the iron surface. Iron is oxidised at the anode, allowing electrons to move towards the cathode. The iron hydroxide forms and the surface and diffuses into the bulk of the electrolyte, where it precipitates and oxidises further to the familiar red rust.

Figure 13 shows a schematic of the aerobic corrosion of iron in water condensation, though the process is the same for immersed conditions as well. Atmospheric oxygen dissolves in the water producing hydroxide ions at the cathode (see Reaction 3) as electrons move from the anode to the cathode.

Reaction 3: Production of hydroxide ions at the cathode [1].

$$O_{2\,(g)} + 2H_2O_{(l)} + 4e^- \rightarrow 4OH^-_{(aq)}$$ E^0 = 0.401 V vs Standard hydrogen electrode (SHE) [73]

it

Metallic iron is oxidized to Fe^{2+} as shown in Reaction 4.

Reaction 4: Iron moves into solution at the anode [1].

$$Fe_{(s)} \rightarrow Fe^{2+}_{(aq)} + 2e^{-} \qquad E^0 = -0.447 \text{ V vs SHE [73]}$$

The iron ions and hydroxide ions meet in the aqueous solution and react to precipitate iron (II) hydroxide according to Reaction 5. This precipitate is then oxidised by dissolved oxygen to form hematite, which is expected to be the predominant deposit in aerobic corrosion [67] (Reaction 6).

Reaction 5: Formation of the precipitate [*1*].

$$Fe^{2+}_{(aq)} + 2OH^{-}_{(aq)} \rightarrow Fe(OH)_{2\,(S)}$$

Reaction 6: Conversion to rust [*1*].

$$4Fe(OH)_{2\,(s)} + O_{2\,(g)} \rightarrow 2Fe_2O_3 \cdot H_2O_{(s)} + 2H_2O_{(l)}$$

2.3.2 Reaction rates and relevant factors

While industry may talk colloquially of stopping or preventing corrosion, it is generally accepted to mean reduced to a negligible level over a time period. Corrosion is difficult to prevent entirely; it is important to note that the rate of the reaction is highly dependent on local conditions [71].

2.3.2.1 *Pourbaix Diagram (potential/pH)*

In addition to corrosion protection by coatings, some metals can be protected by electrochemical methods. In some cases, the corrosion product itself forms a protective film (passivity), the other method is to reduce the driving force to a level such that the reaction does not occur (immunity) [74].

Some alloys are protected by the initial corrosion product. These “passive layers” provide a barrier to the environment, and must be chemically stable and strongly adhering to provide protection [71]. Aluminium and stainless steels can significantly reduce corrosion this way. However, aside from pickling reactions, mild steel forms a loosely adhering layer of oxide that does not form an effective atmospheric barrier.

Cathodic protection, which is commonly used industrially, uses current to protect the asset.

> *“A metal can be prevented from corroding in a liquid by impressing a sufficiently negative potential so that its ions are restrained from entering the ambient liquid.”* [*75*]

As shown in Figure 13 (p25), metal loss occurs at the anode and electrons flow from the anode to the cathode. For cathodic protection, electrons are provided from another source (either as current directly or from a sacrificial anode) preventing the protected area from becoming the anode and therefore averting corrosion and metal loss. This is considered immunity from corrosion.

In considering the potential required to confer immunity to an area of metal, pH also has a role. To quickly visualise this information, potential-pH diagrams (also called Pourbaix diagrams) are used [76]. These can be very complex, but Figure 14 (taken from [74]) gives a simplified Pourbaix diagram for iron in aqueous solution. Immunity is achieved across all pH levels at a potential of less than about -0.7 V, whereas passivity can only be achieved at higher pH. Lines A and B relate to the stability of water. At potential-pH values above line A, O_2 is generated, whereas below line B H_2 is generated. According to the data in this diagram, it is not possible to provide immunity to the metal without also generating H_2 gas. This could be an issue due to flammability and concerns over hydrogen embrittlement, which will not be covered here.

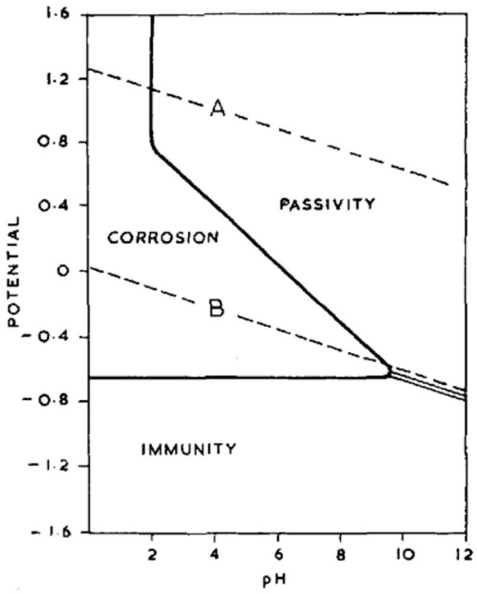

Figure 14: Pourbaix diagram for iron at 10^{-6} M ferrous ions in aqueous solution (taken from [74])

2.3.2.2 *Environmental factors*

Industry has endeavoured to define and classify the corrosivity of environments to which steel structures may be exposed [77]. This improves the understanding of the severity of the environment and the potential performance of coatings by those who specify coating systems for the steel structures.

Table 2 summarises information on some standardised corrosivity classifications.

Table 2: Corrosivity of environments, summarised from [71][77]

Class	ISO category	Annual metal loss (low carbon steel)	Exterior
Very low	C1	<10 g/m^2	Heated buildings with clean atmospheres, eg, offices, shops, schools, hotels, etc
Low	C2	10–200 g/m^2	Rural areas, low pollution, dry
Medium	C3	200–400 g/m^2	Urban and industrial atmospheres Moderate SO_2 pollution Moderate coastal Cl^-
High	C4	400–650 g/m^2	Industrial and coastal
Very high industrial	C5	650–1500 g/m^2	Industry with high humidity and aggressive atmosphere
Very high marine (ISO updated to "extreme corrosivity")	CX	650–1500 g/m^2	Marine coastal, offshore, high salinity

As moisture is required for the reaction, it should not come as a surprise that humidity is relevant to the reaction rates. However, it has been shown that corrosion rates of iron in pure, unpolluted air, even at 100% humidity are relatively low [71][78]. Unfortunately for those attempting to protect metals, even 0.01% sulphur dioxide increases the corrosion dramatically at humidity over 60%-70% [71][78] (see Figure 15). Additionally, precipitated solid particles were found to increase the corrosion rate by providing nucleation sites for the reactants. These contaminants are common, particularly in urban areas where concentrations of atmospheric pollutants are greater. They may be dirt, sand, or chemical precipitants. In addition to atmospheric pollutants, soluble salts such as sodium chloride are ever-present in marine and coastal areas. These increase corrosion rates by hygroscopically attracting water to the surfaces, as well as providing the electrolyte [71].

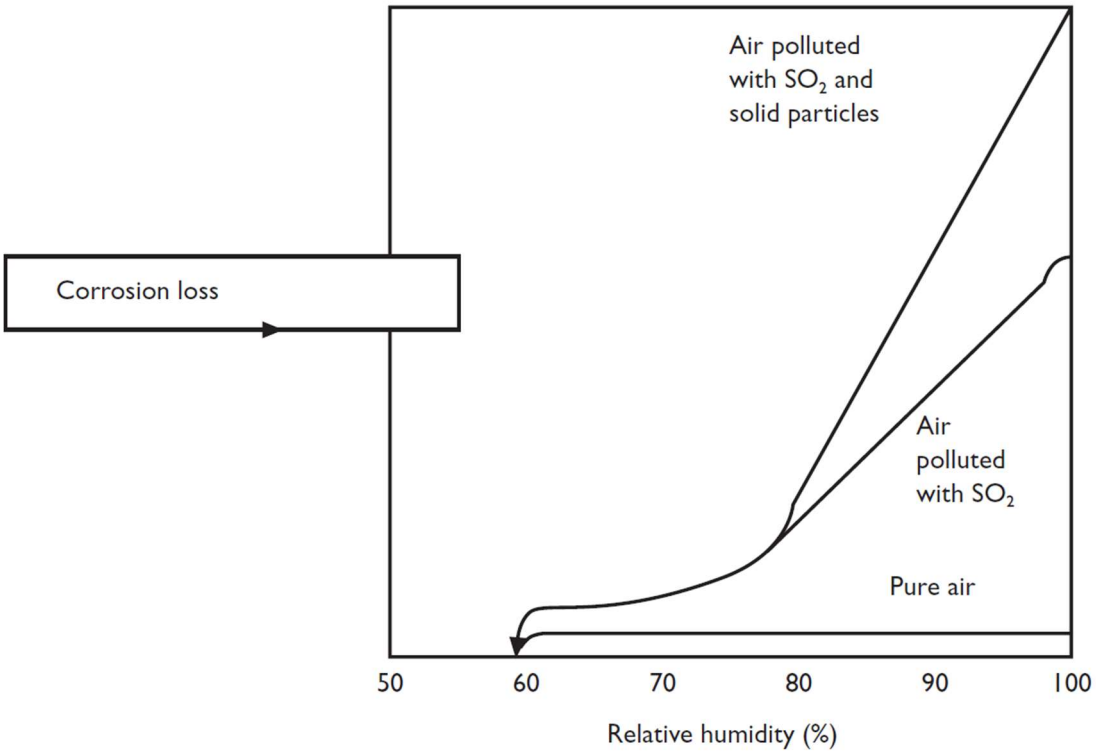

Figure 15: at humidity levels above 60-70%, corrosion rates of steel in a polluted environment increase dramatically, taken from [71].

Pollution is also a concern in submerged conditions. It is well known that sodium chloride and acidic conditions increase the rate of corrosion, but the hardness of water (carbon dioxide, calcium carbonate, bicarbonate) is also relevant [71]. Marine growth and biological corrosion are outside the scope of this work and will not be discussed. As with any chemical reaction, temperature is a factor in the rate of reaction.

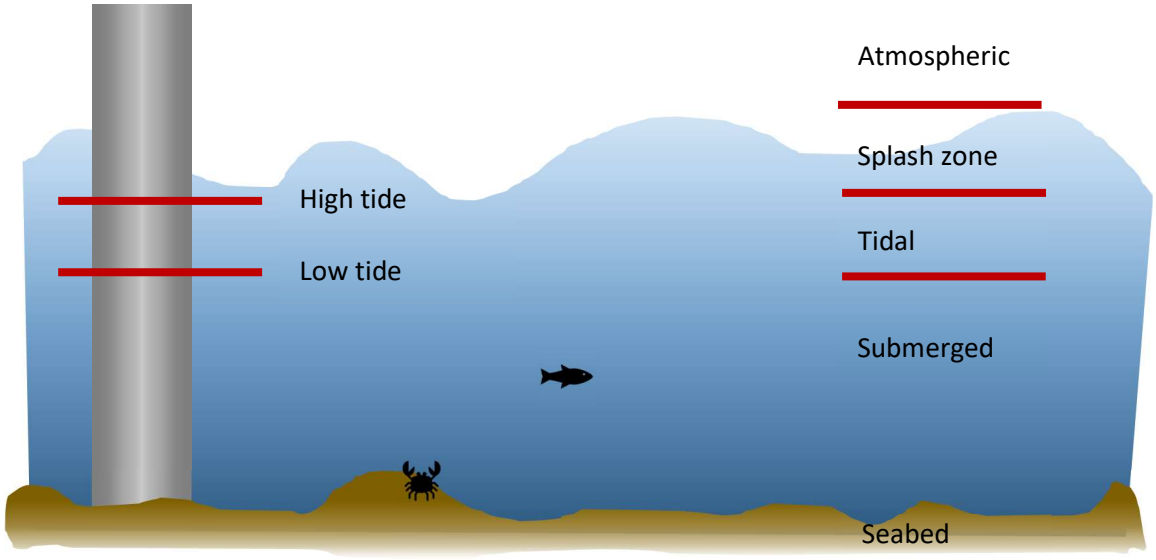

Figure 16: Zones of marine corrosion; Sea Bed: covered by sea bed, but may still be wet; Submerged: constantly underwater; Tidal: slow cycle of wet and dry; Splash zone: fast cycles of wet and dry; Atmospheric: never submerged, but prone to condensation

Typical steel structures that are exposed to marine environments are piles, offshore platforms, vessels and other structures that are immersed in seawater. A steel structure in a marine environment may be exposed to five different corrosion zones depending of the position of its parts relative to the sea level: namely atmospheric, splash, tidal, submerged and seabed-embedded zones (Figure 16). Overall, the corrosion performance and characteristics of steel is different in each zone [79]. The main factors that affect the corrosion rate of steel are salinity, dissolved oxygen concentration, temperature, pH carbonate, pollutants and biological activity. The characteristics of seawater with respect to these factors is summarised in Table 3.

Table 3: Environmental factors in seawater corrosion [79]

Salinity	**Open sea**: Variation with horizontal location is small, 32-36 parts per thousand (ppt). Near river outlets: Lower Variation with depth: very small
Dissolved oxygen concentration	**Surface water**: **(1)** Near the equilibrium saturation concentration with atmospheric oxygen at a given temperature [6 ppm (in the tropics), 11 ppm (in the Arctic)]. **(2)** Can be supersaturated due to photosynthesis by microorganisms (up to 200%) and entrainment of air bubbles (up to ~10%). **Variation with depth**: **(1)** Tends to be undersaturated due to consumption by the biological oxidation of organic matter. **(2)** Goes through a minimum at intermediate depths (400-2400 m deep).
Temperature	Surface water: In the open ocean, variations are in the range of -2°C to 35°C depending on the latitude, season, currents, etc. Variation with depth: Drops with depth. The difference with depth and season may be large or small depending on the location.
pH	**Surface water**: **(1)** Lies between 7.5 and 8.3 in the open ocean depending on the concentration of dissolved carbon dioxide determined by air-sea exchange and photosynthesis activity. **(2)** Microbiological activity affects the pH; e.g., lower pH by the formation of carbon dioxide through the process of biochemical oxidation and higher pH values by the reduction of carbon dioxide through the process of photosynthesis. **(3)** Affected by pollutants in the coastal waters. **Variation with depth**: Tends to show a profile similar to that of dissolved oxygen (the biochemical oxidation that consumes dissolved oxygen generates carbon dioxide, reducing the pH value).
Carbonate	**Surface water**: Nearly always supersaturated with respect to $CaCO_3$ (200-500 %) favoured by high pH values and moderate temperatures. **Variation with depth**: Saturation state with respect to $CaCO_3$ decreases as the result of lower temperature and pH. Undersaturated in deep waters (e.g., below 200-300 m).
Pollutants	H_2S may be 50 ppm or higher in polluted waters in estuaries, harbours, ports and basins. Ammonia may be high in inshore and harbours.
Biological activity	Bacteria form biofilms (slime) Weeds grow from spores Animals (e.g., barnacles, tubeworms and hydroids) adhere.

2.4 CORROSION PROTECTION BY ORGANIC COATINGS

The comprehensive mechanism by which organic coatings protect reactive metal substrates is not yet fully understood. It is generally agreed that the organic coating provides a physical barrier to water, ions and oxygen [80][81] – insulating the metallic surface from the corrosive environment

– thus preventing the cathodic reaction. However, the fallacy of the barrier model was revealed in the late 1940s, when researchers determined that most practical paint films (including those known to provide protection in the field) allowed far more moisture (and, in most instances, more oxygen) through the coating to the metallic surface than those levels of such reactants that would be necessary to sustain the cathodic reaction (see Table 4, Table 5) [82]. Thus, additional mechanisms must also be considered.

Table 4: Transmission of water and oxygen through protective coating films [82]

Coating type	**Transmission of water †**	**Transmission of oxygen ‡**
Chlorinated rubber primer	20±3	30±7
Chlorinated polymer	26±5	33±2
Coal tar epoxy	30±1	213±38
Aluminized epoxy mastic	42±6	110±37
Titanium dioxide pigmented alkyd	258±6	595±49
Red lead/linseed oil primer	214±3	734±42

†g of water m^{-2} day^{-1}, 25 µm film, 95% RH and 38°C
‡ mL of oxygen m^{-2} day^{-1}, 100 µm film, 85% RH, 38°C and 1 atmosphere O_2

Table 5: Threshold quantity necessary to support corrosion rate of 70 mg Fe cm^{-2} y^{-1}, which is the corrosion rate of unprotected mild steel in a typical industrial environment (unprotected or maximum corrosion rate)

	Transmission of water †	**Transmission of oxygen ‡**
Required reactants	0.93	575

†g of water m^{-2} day^{-1}, 25 µm film, 95% RH and 38°C
‡ mL of oxygen m^{-2} day^{-1}, 100 µm film, 85% RH, 38°C and 1 atmosphere O_2

2.4.1 Barrier properties

It seems to be fairly obvious that organic coatings provide some corrosion protection by presenting a physical barrier - baring migration of water, oxygen, and/or ions to the surface [17]. Intuitively, the thicker the coating, the better the barrier properties, as it takes longer for the water, oxygen, and ions to penetrate the organic coating [83]. No organic coating is a complete barrier to water, oxygen, and ions. In general, water and oxygen diffusion rates of organic coatings are far too high to be the limiting factor in the corrosion reaction (Table 4, Table 5), but ion solubility is typically quite low [80][84]. Early hypotheses also suggested that carbonyl groups in the polymer backbone could become negatively charged in the presence of water, thus preventing the penetration of anions [84].

Further investigation into the nature of the barrier properties of organic coatings led to two possibilities. The first, that the eventual penetration of water, oxygen, and ions facilitated the development of conductive pathways through the organic coating. Prevention of ion migration is

key requirement of a corrosion resistant coating, but it is believed that migration of ions is linked to the migration of water [17]. It has been proposed that after a period of time, small, localised "pores" form, allowing water and ions through the coatings [17] though further work has cast doubt on this theory [85][86].

Another proposed mechanism suggests that ions move through the bulk of the polymer, but this migration is favoured in areas of localised ionic character [18][86][87]. Recent work using fluoroprobes seem to confirm this mechanism [87], though it does not rule out the above theory of pores. Additionally, ionic species were detected moving through the epoxy coating, but this was not confirmed to produce conductivity.

2.4.2 Insulation properties and "D" and "I" areas

It is generally understood that corrosion begins at the areas of a coating where the electrical resistance is lower than the rest of the film [12]. Early studies cut samples into small squares (approximately 1 cm^2) and measuring the resistance over that area. While this allowed the determination that samples with lower resistance were more susceptible to corrosion than those with higher resistance, it did not allow investigation into the size or location of the areas of lower resistance. The samples were classified as either "I" (indirect, high resistance) or "D" (direct, lower resistance). Later work improved the resolution to a few square mm via the wire beam electrode [12]. Although they cite Mayne et al. for the assertion, "most inhomogeneity of coatings is not due to pores or fissures but instead due to the inhomogeneous bonding within the polymer film", polymer bonding cannot be investigated on this scale. Clearly, lateral resolution must be vastly improved to investigate and map defects in molecular bonding. By working in electrical modes of AFM, this work attempts to reduce the lateral resolution to investigate electrical differences in the polymer bonding.

Corrosion is an electrochemical process, and therefore the electrical properties of the corrosion-prevention coating are expected to be of utmost relevance. In some cases of pipeline coatings, compatibility of a failed coating with cathodic protection systems is believed to be an electrochemical property of the coating [88]. For a coating to perform well with cathodic protection, any eventual failure must be in such a way to allow the cathodic protection to operate. Additionally, each coating has a breakdown voltage that, if exceeded would risk damage to the coating. While this is not usually a danger in cathodic protection, it should be considered before performing holiday testing. Laboratory electrochemical techniques offer an opportunity to identify areas vulnerable to corrosion before they would be visible [89]. Electrochemical

Impedance Spectroscopy (EIS) has confirmed the development of localised defects [17], but as the data is integrated over an entire surface [18] it is not possible to identify or map the defects with this method. Other groups have previously used wire-beam electrodes as well as cutting up individual samples to measure the electrical inhomogeneity of polymer coatings [12]. Using these methods and conventional kelvin probes, the resistance is integrated across the whole surface of the coating, and mapping of the electrical properties is not possible. The difficulty with these techniques is that they only indicate if an inhomogeneity exists, not the size, number or location. A technique with improved spatial resolution is desirable. In this work, CSAFM and KPFM (Sections 3.2.3.5 and 3.2.3.4) have been used to attempt to improve the understanding in this area.

2.4.2.1 *Cathodic disbondment*

Once the corrosion reaction has begun, further coating degradation occurs from the production of hydroxide at the cathode [81]. Indeed, hydroxide production at a defect in the coating has long been known to cause de-adhesion [90], also known as cathodic disbondment [91]. Cathodic disbondment reduces the effectiveness of the organic coating by accelerating the loss of adhesion and thereby the loss of barrier properties [67]. Additionally, there is risk of deep localised corrosion under disbonded coatings [92]. (see Section 2.5.6.3)

2.4.3 Adhesion

If an organic coating is going to provide a barrier and protect the surface from corrosion, it is fairly obvious that the coating must remain in contact with the surface. Adhesion is of key significance and is affected by many of the other concepts presented throughout this section. The basics will be presented here, while interactions will be discussed where relevant. Importantly within the chemical curing process internal stress may develop, arising from solvent release and/or polymerisation, which will increase as film thickness increases. The stress produced may be capable to overcoming the adhesion of the coating, even over abrasive blasted surfaces. In less extreme cases, residual internal strain remaining within the coating after curing will inevitably reduce the amount of tensile stress from of sources (in service stress, thermal stresses, etc.) that the coating is able to withstand before delaminating.

As corrosion occurs at the surface of the metal substrate, the interface of the metal with the polymer is of great importance. Adhesion has long been identified as an important characteristic in protective coatings, but there is not a straightforward relationship between adhesion strength and corrosion protection [93]. Some studies concluded that wet adhesion strength is key to

improved performance though this does not seem to be generally agreed [94]. While it is important that the coating remain in place, some purposely low-adhesion (by traditional test methods) systems are successful by utilizing low cohesive forces as well. When these coatings are subjected to "traditional" adhesion tests, the coating purposely fails cohesively, leaving some material on the surface and some on the test grip. As long as material remains on the surface, there is some corrosion protection. Typical coating protections that successfully employ this method include grease tapes, petrolatum tapes, and viscoelastic materials.

Previous research has reported that polymers in a blend can have preferential adsorption characteristics to the substrate [95][93]. As unsaturated polyesters also have a polystyrene portion with different characteristics, adsorption may contribute to differences in corrosion protection.

2.5 Industrial Application, Use, and Testing of Protective Coating Systems

This section follows the procedures of a typical industrial application of unsaturated polyester coating, including alternative methods. Some of the common test methods used for unsaturated polyester coatings in the UK are also described.

2.5.1 Overview of Industrial Coatings Projects

Industrial coatings projects can span multiple phases over many years and involving several stakeholders. Some of the common roles and responsibilities are mentioned here.

2.5.1.1 *Asset Owner*

The owner of the asset (e.g. pipeline, oil rig, refinery, etc) may specify the parameters of the project, or may contract that work to a specifier.

2.5.1.2 *Specifier*

The specifier may be employed directly by the asset owner for companies with a large number of assets (e.g. BP) or may be a specialist consultancy hired for the project. The role of the specifier is to write and agree the job specification, including what materials to use, application parameters, inspection schedule, training requirements, etc. Deviations from the job specification are generally agreed with the specifier.

2.5.1.3 *Manufacturer*

The company that has manufactured the coatings. The manufacturer provides technical properties, application recommendations, and performance test data. They may also participate

in a pre-qualification trial, and/or a pre-production trial. In some cases, the coating materials may be supplied by another company handling procurement (supplier).

2.5.1.4 *Contractor*

In large projects the asset owner may employ a contractor to oversee all aspects of the work. The contractor would then contract portions of the job with specialists. This is more common on jobs that require multiple specialties (e.g. pipelaying, coating, construction, etc).

2.5.1.5 *Applicator*

The application is responsible for applying the coating materials according to the job specification (which overrules, but generally follows the manufacturers recommendations). The applicator would participate in a pre-production trial to ensure the applied coating meets the job specification.

2.5.1.6 *Coating Inspector*

The role of the coating inspector is to represent the interests of the asset owner in verifying that the job specification has been followed. The coating inspector is normally onsite daily, recording materials information: batch numbers, usage rates, etc. Additionally, the coating inspector will perform tests on the applied coating in accordance with the job specification. To avoid conflicts of interest, the coating inspector should be employed by the asset owner.

2.5.1.7 *Pre-qualification trial (PQT)*

A pre-qualification trial enables manufacturers to demonstrate that their coating material is expected to perform well within the scope of the job.

2.5.1.8 *Pre-production trial (PPT)*

A pre-production trial is a further test designed to ensure all parties and materials can work together to provide the coating performance expected. A pre-production trial is normally specified material applied by the applicator in a test area representative of the job conditions.

2.5.2 Considerations for coating selection

During the development of a coating and during validation for various projects, coatings are subjected to a variety of standardised test methods to help determine the suitability of the coating. Formulated industrial coatings are generally supplied with a technical data sheet indicating typical properties. Some are important to the application and use of the coating, and some are important to the final performance. It is common for a coating to be selected from a group of potential products via a pre-qualification trial (PQT) [96].

Gel or cure time of unsaturated polyester coatings is particularly difficult to quote due to the overwhelming influence of sample size and shape, temperature as well as commercial initiator. In practice, a manufacturer will typically follow an internally set method. This ensures comparability with other internal measurements, but not with external measurements or on-site conditions. The cure kinetics has been studied by DSC [97][98] but this type of equipment is not available for many coatings formulators and impractical for on-site use. The decomposition of the peroxide initiator begins a small exotherm which is soon overwhelmed by a larger exotherm from the reaction of polyester and styrene double bonds [97]. The cure time is often inferred by monitoring the heat generated by the exothermic reaction using only a thermocouple. The reported value might be time to peak temperature or time between two specified temperatures (e.g., 35°C to peak) depending on the method.

Flashpoint is generally a safety concern. In some situations, unsaturated polyesters cannot be used due to the flashpoint of the styrene monomer (26-32°C). In the past, some open-cup methods have been used, but the industry has started to move towards closed-cup methods. There are many methods used, including ASTM D93, EN ISO 1516, EN ISO 2719, etc. [99].

Depending on the service conditions, strength and flexibility of the final coating may be relevant. Most of the final properties are heavily influenced by the resin selection. A selection of properties of various unsaturated resins is shown in Table 1, p 15.

Although more common in vinyl ester coatings, the chemical resistance can also be important for considering unsaturated polyester coatings. Indeed, strong chemical resistance requirements will generally direct a specifier from unsaturated polyester coatings to vinyl esters for tank linings.

Once a coating system is selected, its performance and application is often trialled in conditions as close to the intended use as a pre-production trial (PPT) [96].

2.5.3 Surface preparation and testing

For all industrial coatings, surface preparation is an important part of the process. However, as this work is focused on the defects in the coating, it will not address issues arising from poor surface preparation or engineering design, e.g., sharp edges, hard to reach corners, bolts or welds.

Surface contaminants such as dirt, soluble salts, oils, greases and metalworking fluids must be removed from the surface prior to work, or they risk being spread further [100]. Proprietary

detergents and cleaning solutions [101][102] are available, as well as solvent cleaning processes. It is important not to skip this step as the following "cleaning" processes do not remove chemical surface contaminants such as salts and oils.

Once the surface is free of contaminants, the surface itself must be considered. If the steel substrate is newly manufactured, it is likely to have mill scale. This is a serious problem as mill scale tends to be loosely adhering and increases the corrosion rates, though the mechanism is not fully understood [103]. If the coating were applied on top, it could lead to delamination of both the mill scale and the coating. Additionally, mill scale has a more positive galvanic potential than carbon steel and can therefore set up a galvanic cell – causing corrosion [71][104].

2.5.3.1 *Tool cleaning*

Tool cleaning is necessary in some cases where conditions prohibit the use of abrasive blast cleaning. However, it is considered less effective that blast cleaning as it is not generally useful for adherent material [105]. Tool cleaning is separated into two types; hand and power. Hand tool cleaning involves the use of a wire brush or other scraper to manually remove loose scale rust and paint. It also provides very little surface profile and takes a long time. Common inspection standards include ISO 8501-1, St2 or St 3, SSPC-SP2.

Power tool cleaning is more efficient than hand-tool cleaning, but it requires more equipment, and a power source – usually either electricity or compressed air. Some common power tools include rotary wire brushes, impact tools and grinders. Common inspection standards include SSPC-SP 3, SSPC-SP 11 and ISO 8501-1 [105].

2.5.3.2 *Abrasive blast cleaning*

Abrasive blast cleaning utilises high pressure air to accelerate an abrasive particle toward the substrate. The abrasive can reach speeds of around 720 kph [105]. The impact of the abrasive on the substrate removes adherent contaminants as well as loosely adherent material and some base metal. Common abrasives include crushed slag, natural mineral grit, and ceramic grit. Contrary to popular terminology, sand is no longer commonly used in the EU as a blasting abrasive due to the content of silica which can cause silicosis of the lungs. However, it may still be in use in some parts of the USA.

2.5.3.3 *Water cleaning*

Water blast cleaning has two advantages over traditional abrasive blast cleaning. It avoids dust formation and helps wash away soluble surface contamination. Water jetting uses only water, whereas water blast cleaning uses water combined with an abrasive. Water jetting can use a

wide range of pressures from low (below 34 MPa) to ultrahigh (above 210 MPa) depending on the cleaning and surface preparation required. However, even ultrahigh pressure water jetting will not produce a surface profile [105]. Water blasting does produce a surface profile, but it is generally less than the dry equivalent [105]. As the freshly cleaned metal surface will be particularly active, it is common practice to add inhibitor (often nitrites or amines) to the water to avoid "flash rust".

2.5.3.4 *Surface testing*

There are three main criteria specified for surfaces. The first is the type and degree of cleaning. ISO 8501-1 is a commonly used visual standard of cleaning by abrasive blast and takes into account the condition of the steel after removal of previous coatings and mill scale. This scale is differentiated by the condition of the steel. New steel looks significantly different to previously corroded steel and cleaning will not make refurbished steel look visually like new steel. Additionally, the NACE/SSPC and Swedish Standards are also commonly used. A grade of Sa 2 ½ by the Swedish Standard (SIS 055900) is approximately equivalent to NACE/SSPC of Near-white Metal (NACE No 2, SSPC No 10). This is the most common rating required by polymeric coatings, though some are marketed as particularly tolerant to poor surface preparation.

In addition to the condition of the steel, the surface profile may be specified. Surface profile is thought to enhance adhesion by increasing the contact area and providing a mechanical anchor. In the field, the surface profile may be measured by replica tape which uses a conformable foam layer on a PVC backing. The foam layer is pressed into the surface and is an imprint of the surface is created. This method produces a record which can be taken away and referred to at a later date. Relevant standards include: ASTM D4417, NACE RP0287, and ISO 8503-5. Other methods, such as the needle profilometer measure the distance from peak to valley (ASTM D4417-B, SSPC PA17) (see Figure 17). All of these methods require multiple measurements to achieve an average profile. However, the surface comparator is a physical reference standard used to qualitatively compare a graded surface with the surface to be measured. These are quick and easy, but require more experience and judgement than quantitative methods. Relevant standards include: ASTM D4417-A, ISO 8503-1, and SSPC 17. A typical profile for unsaturated polyester coatings would be on the order of 50-100 µm. This is normally a figure that the manufacturer is comfortable with based on industrial consensus and experience.

Figure 17: schematic of a profile measurement by profilometer. Several measurements of peaks to valleys are taken and the average is reported.

Once the substrate has been confirmed to be sufficiently abraded and profiled, surface contaminants may be measured. Oils are difficult to measure quantitatively, but as they can cause loss of adhesion some qualitative detection may be employed. Methods include using ultraviolet light or solvents to detect oils and other hydrocarbon contaminants.

Soluble salts are often measured to reduce the likelihood of osmotic blistering (described in Section 2.5.6.1). A common method of measuring soluble salts is the Bresle test. This involves using a patch of known area to contain a known volume of distilled water. The water dissolves the soluble salts and is then removed for conductivity testing. Although no information on type of salt is given, the test is relatively easy to perform in the field. Relevant standards include ISO 8502-6 and ISO 8502-9. There is significant debate regarding the merit of testing for all salts indiscriminately vs testing specifically for chlorides – which are known to have a greater effect on the corrosion performance [106][107][108].

2.5.4 Application

Unsaturated polyester coatings are generally applied by spray, though they may also be applied by brush, roller, or lay-up. Spray application involves using high pressure to force the liquid coating through a small orifice in the spray gun tip, thus “atomising” the paint, i.e., reducing it to very small liquid droplets [105]. The liquid droplets land (mostly) on the substrate and ideally flow together to form a continuous film of uniform thickness. In practice, this is not always the case as surface contaminants or other factors can change the ability of these droplets to flow; see Sections 2.5.5 and 2.5.6. However, most application defects can be identified and corrected prior to the conclusion of the project.

2.5.5 Application Defects

Industrial coating projects often employ coating inspectors to provide an impartial record of the process to the asset owner, thus helping ensure that the project specification is followed. Inspection methods are limited by the location of the structure. In some cases, this can be a remote pipeline or offshore installation without easy access to utilities.

2.5.5.1 *Macro defects*

Due to the high costs associated with coating failure, many projects employ specially trained coating inspectors to monitor surface preparation and atmospheric conditions as well as examine the coating for application and cure defects. Macroscopic failures are usually visible or detectable during the installation process. These could be insufficient coating thickness or "holidays", blisters, pinholes, cracks, sags or runs, craters or insufficient cure. To prevent the failure at these defects, they must be repaired before the job is complete. As these defects are well established as focal points for the initiation of corrosion, this work will consider only samples without macro defects.

2.5.6 Failure modes

2.5.6.1 *Osmotic blistering*

While substrate cleanliness usually does not present a problem in small, lab-scale samples, it can be a serious issue in an industrial setting causing osmotic blistering. Osmotic blistering is not yet completely understood, but it is generally agreed to require four conditions: (1) a semi-permeable membrane (paint film), (2) a relatively impermeable substrate, (3) water-soluble solids or salts that cannot pass through the membrane, and (4) a concentration gradient [109].

As coatings have a low permeability to ions [80][84], they behave as a semi-permeable membranes [110]. Water passes through the coating and dissolves any soluble salt contamination on the substrate surface. When the salts or solids are too large to diffuse through the paint film, but water is able to move through the film, this sets up a concentration gradient across the paint film. In order to balance the difference in concentration, water flows through the paint film from the dilute side (coating surface) to the concentrated side (coating-substrate interface). This concentration gradient drives more water across the paint film, towards the substrate [109]. As water acumulates at the substrate-coating interface, the coating is forced away from the substrate, causing blistering or cracking (Figure 18). This does not continue indefinitely as the forces will eventually equilibrate [111].

The main ion of concern in an industrial environement is chlorides – mainly due to their high corrosion activity. Other ions such as sulphates and some water-soluble solvents may also cause osmotic blistering [109].

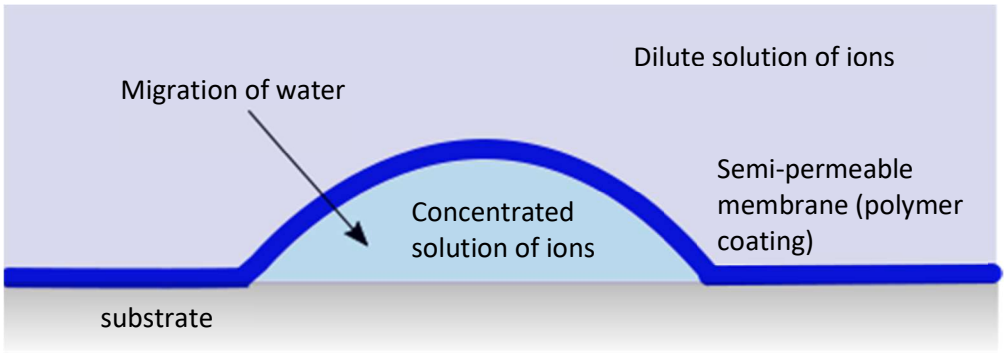

Figure 18: Schematic of osmotic blister. A membrane that is permeable to water but not permeable to ions or other contamination creates a concentration gradient causing water to move towards the higher concentration of ions at the coating-substrate interface.

Although the blister is visually undesireable, the consequences of blistering go beyond visual. Under the blister, corrosion may occur. In some cases, the blister can still form enough of a barrier to electrical current to prevent cathodic protection from functioning [88], see Section 2.5.6.3.

2.5.6.2 *Cracking*

Cracking defects are generally visible and can penetrate fully or partially through the coating [105]. In either case, they reduce the distance reactants must penetrate to reach the substrate and engage in the corrosion reaction. Cracking can be due to curing defects, substrate movement or coating ageing. In service, the area must be removed and re-coated.

2.5.6.3 *Cathodic disbondment*

In high-value or high-consequence situations, the risk of failure prompts investment in complementary corrosion protection. In submerged or buried conditions, cathodic protection is commonly used in conjunction with coatings. In the event that the coating fails or is damaged, the cathodic protection becomes active to protect the substrate (Figure 19). The principle of cathodic protection is to supply a current to the structure such that any exposed substrate becomes cathodic rather than anodic [112]. The electrical potential of the metal is made negative by the application of a voltage, such that positively charged cations (such as Fe^{2+} cations) are unable to leave the metal lattice [84]. Cathodic polarisation has also been observed as the pH of the solution rises, decreasing the corrosion reaction [113].

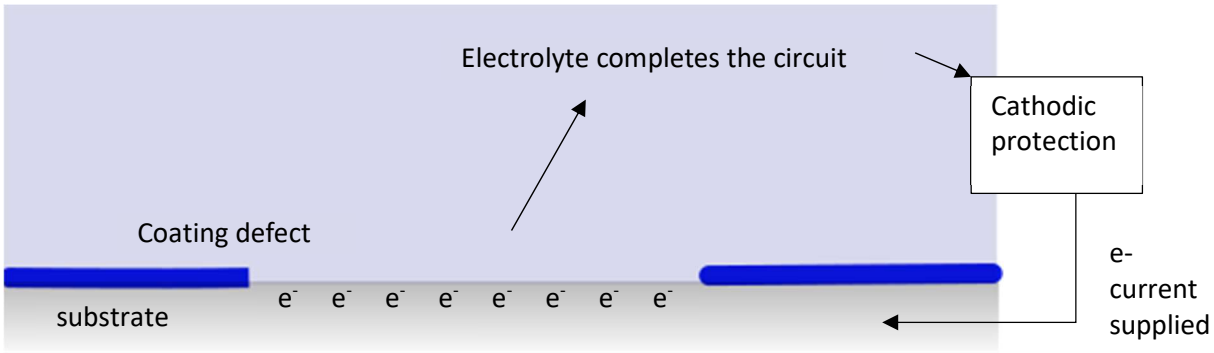

Figure 19: Simple schematic of cathodic protection. The current supplied completes the circuit at the coating defect, causing the exposed metal to become cathodic rather than anodic.

However, cathodic protection can have negative effects as well. Above a certain potential, water is reduced to produce hydrogen (Reaction 7). The high pH caused by the production of hydroxyl ions can also damage some coatings. Additionally, the production of hydrogen can cause a physical lifting effect [114]. Where the coating is lifted due to a cathodic reaction, it is termed cathodic disbondment or cathodic delamination.

Reaction 7: Reduction of water to produce hydrogen [115]

$$2H_2O_{(l)} + 2e^- \rightarrow H_{2\,(g)} + 2OH^-_{(aq)}$$

In test conditions where the electrolyte is saturated with nitrogen so a rust product cannot form, the metal may still be solubilised; though the disbondment only occurred during the cathodic reaction [93].

2.5.6.4 *Non-cathodic loss of adhesion*

Many factors can contribute to the loss of adhesion of a coating. Excluding surface contamination and cathodic disbondment, which is discussed separately in Section 2.5.6.3, the mechanisms of adhesion loss include degradation of the substrate or the coating at the interface, as well as displacement of the bonds by water or hydroxide [93][116].

2.5.7 Service Life

2.5.7.1 *Monitoring and detectability of failures*

Since it is not possible to continuously monitor every part of the asset for corrosion, the operators must use all available data to assess the risk of corrosion. Most assets are large and encompass several different environmental conditions and may be susceptible to different types of corrosion. The operators must consider the severity of the consequence of failure together with the ease of detection (Figure 20). The best case is that the risk of consequences is low and that corrosion is

easy to detect. However, in some cases, the risk of consequences might be catastrophic (major spills, explosions, etc) and the corrosion difficult to detect due to accessibility, types of corrosion, etc. Operators will need to consider these risks when establishing a maintenance plan.

Despite all the known failure modes, and remediation steps taken, coating failure still occurs in unpredictable and seemingly defect-free locations [94]. This work aims to consider inherent, currently undetectable defects in the coating resin to help predict where corrosion will begin.

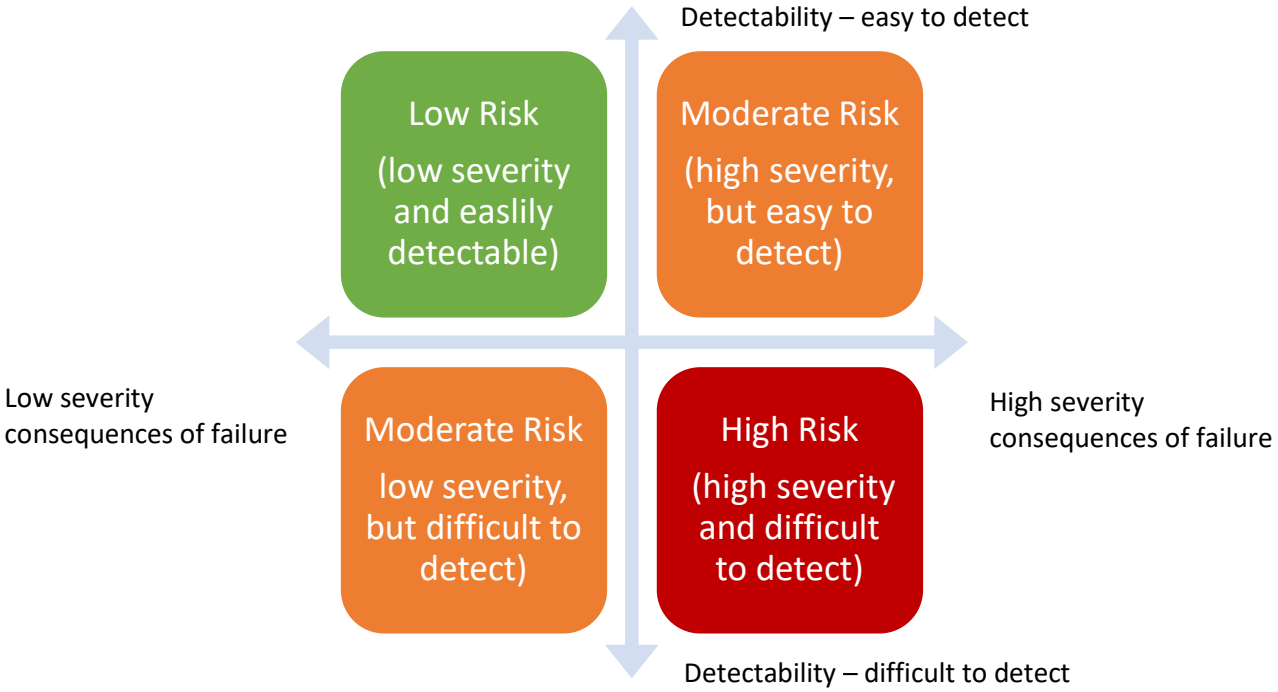

Figure 20: Risk matrix of severity and detectability. Potential coating failures with severe consequences must be allocated more testing resources.

2.6 Academic Application and Testing of Protective Coatings

2.6.1 Surface preparation

Most surface preparation techniques that can be achieved in the field can also be achieved in a laboratory setting. However, in some cases, it can be difficult to replicate the result. For example, abrasive blast cleaning of small samples can deform the samples to an unacceptable degree.

In addition to the surface preparation techniques available to duplicate industrial techniques, a range of techniques suitable for small samples is also available. Surface grinding and polishing is often used to create a flat, uniform surface for academic study. This would be impossible to achieve in the field (and undesirable due to the lack of a surface profile – see Section 2.5.3.2). For

industrial applications, higher surface profile (around 50µm) is desirable because the increased surface area and mechanical interlocking can greatly improve adhesion.

2.6.2 Application

Similarly, to surface preparation, most of the same techniques are available to apply the coating, plus a few more specialised techniques. For example, spin coating is often used in a laboratory setting to achieve a flat, uniform, coating of low thickness.

2.6.3 Testing

2.6.3.1 *Micro defects*

One of the main objectives of a corrosion resistant coating is to provide a barrier, thus blocking the path of ions between localised anodes and cathodes [80]. Unfortunately, all polymer coatings also have some degree of permeability to oxygen and moisture that changes over the life of the coating. The permeability of the polymer generally depends on a number of factors, including the hydrophobicity of the polymer, the density of the crosslinking, and the completeness (degree) of curing. High-performance anti-corrosion coatings often use plate shaped talc or glass to improve the resistance to moisture permeation. Even in these highly loaded coatings, the polymer matrix is a vital part of the protection and any improvement of the polymer would be likely to improve the system overall. As the diffusion rates for moisture and oxygen through most organic corrosion protection coatings far exceeds that which is required for the corrosion reaction to proceed (Table 4 p32), it is important to note that ion solubility within the coatings is typically very small [80].

2.6.3.2 *Chemical inhomogeneity*

As mentioned in Section 2.1.1, commercial unsaturated polyesters are irregular molecules of around 3000 g mol^{-1}. Commercially, these are blended with styrene. Even if the application of the liquid is homogeneous, the components within it may not be arranged homogeneously. This leads to an inhomogeneous structure on the micro- or nanoscale. The dual phase nature of unsaturated polyester polymer in styrene lends itself to preferential association of the styrene phase to the surface and/or substrate interface. Coatings may have regions of crystalline structure, variations in crosslink density and differences in molecular structure. It has been hypothesised that extremely localised inhomogeneities in the crosslinking and structure of the polymer coating may contribute to the onset of corrosion. As mentioned earlier, considerable work has been done to characterise the structure of cured unsaturated polyester coatings. It has been shown that polyester microgels form first, then a styrene network forms around the

microgels [19]. By forming separate areas of polyester and styrene, the cured polymer shows structural differences. It is hypothesised here that differences in the electrical properties, and therefore the corrosion resistance will also be shown in later stages of this work.

In addition to inhomogeneity in the polymer itself, pores and voids exist within the cured polymer. It has been reported that the free volume hole size of an unsaturated polyester in styrene measured by Positron Annihilation Spectroscopy (PAS) is approximately 0.069 nm^3, which makes up approximately 2.25% of the cured volume [117]. Given the volume of the pores, assuming a spherical pore, the diameter of a pore should be on the order of 0.5 nm.

2.7 Summary

Corrosion of metals in atmospheric conditions has been thoroughly examined from both an academic and industrial context and is generally well understood. Through industrial case studies and macro techniques, it has been clearly proven that organic coatings do inhibit corrosion. However, the way in which organic coatings can prevent corrosion is somewhat less clear. The specific criteria and mechanisms for an academic perspective are not fully understood.

Unsaturated polyester coatings have been similarly researched from both industrial and academic perspectives. The properties of the cured polymer are of great interest to the industrial community and has therefore been exhaustively measured in many configurations. The curing and its effect on the polymer properties have also been thoroughly examined. As analytical techniques have improved, some academic investigation of the fundamental polymer has been done. However, as techniques have further improved in the last 20-30 years, academic focus has shifted away from the fundamentals of older technologies such as unsaturated polyester coatings.

There is significant industrial value and unexplored academic potential in the investigation of the corrosion prevention mechanisms of unsaturated polyesters using relatively new analytical techniques. It has previously been reported that reduced electrical resistance of an organic coating correlates with increased susceptibility of the substrate to corrosion [14]. Additionally, capacitance and dielectric constant should correlate with corrosion potential [16].

Using currently available detection methods, polymer structure and morphology will be probed to identify those responsible for the majority of electrical activity. The identification of electrical activity within a coating has previously been limited to a bulk sample. CSAFM allows high-resolution mapping of these electrical features that was previously unachievable (refer to Section

3.2.3.5). By mapping the electrical resistance and correlating it to chemical structures within the polymer, it will be possible to relate the chemical structure and morphology to the electrical properties (and infer the onset of corrosion). Highly specific data relating the structural, morphological and phase features to the electrical activity will help explain performance differences and elucidate the mechanism of corrosion protection by organic coatings that is not currently fully understood (Section 2.4). This new information source will allow resin manufacturers to pinpoint the weakest link in their corrosion protection resins. Using this information, they will be able to optimise the polymer for corrosion projects – giving a significant commercial advantage.

3 INSTRUMENTATION

3.1 ALICONA INFINITEFOCUS 3D OPTICAL MICROSCOPE

The Alicona InfiniteFocus 3D Optical Microscope works as a regular optical microscope with the ability to easily capture images. It has the added feature of capturing images from a range of depths and angles to reproduce a topographical map of the surface. There are some limitations to the topographical mapping though. Light travels in straight lines and cannot divert around particularly rough or jagged surfaces to map crags or valleys. Figure 21 shows a schematic demonstrating how a rough surface can block some features from view.

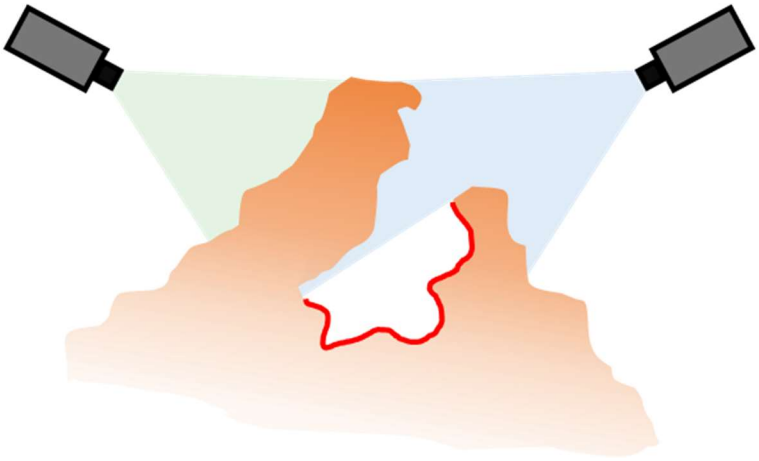

Figure 21: Schematic of problematic crag in a sample for 3D microscopy. In this case, the cameras (in black) cannot "see" the surface highlighted in red as it is blocked from view by the nearby peaks.

Additionally, optical microscopy is not suitable for the extremely small measurements required to determine the sub-micron structure. It has limitations that stem directly from the use of visible light. The resolution is limited by the wavelength of the light. Reductions in wavelength to near-ultraviolet, as well as techniques using electron beams can cause degradation of organic samples during examination.

3.2 ATOMIC FORCE MICROSCOPY (AFM)

3.2.1 History and Invention

Scanning Tunnelling Microscopy (STM) was invented in the late 1970s by Binnig and Rohrer at IBM Zurich [118], for which they were subsequently awarded the 1986 Nobel Prize in physics. This precursor to the Atomic Force Microscope (AFM) moved away from using light and optics and instead made use of the vacuum tunnelling effect, also known as quantum tunnelling. If a bias

voltage is applied to a conductive sample and conductive tip very close together, the tunnelling of electrons in the vacuum were measured. Later STM are able to measure in air or liquid. STM measurements are particularly dependant on the distance from the STM to the cantilever and use the forces exerted on the probe by the sample surface, the system was highly susceptible to noise from surrounding vibration. Unfortunately, the STM required precise control of the tip/sample distance, was limited to conductive samples, and was more suitable for a vacuum environment. Fortunately, these limitations were soon overcome by the AFM [119].

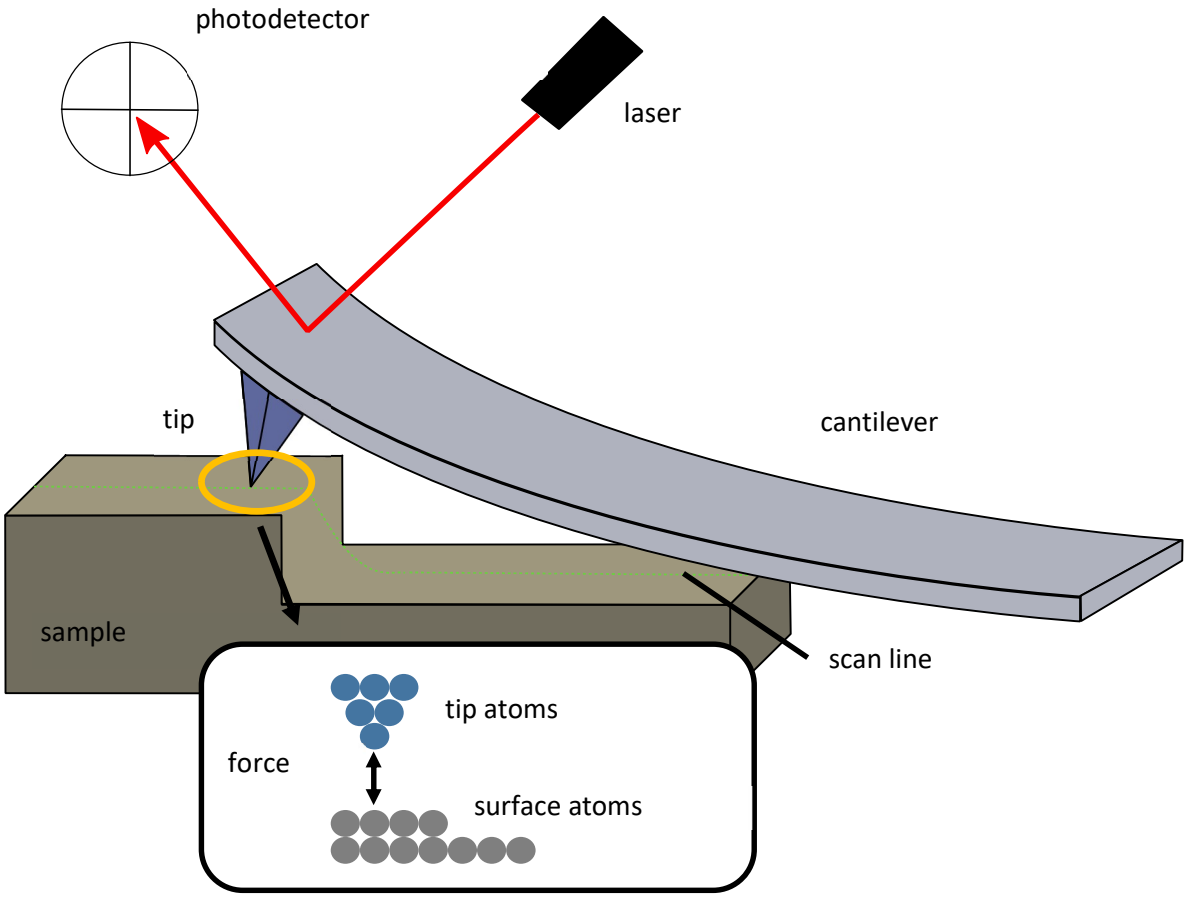

Figure 22: Schematic of Atomic force microscope (AFM). (Modified from Agilent AFM 5500 user's guide [120])

3.2.2 Principles of Atomic force microscopy (AFM)

AFM does not use light and is therefore free from the resolution limitations of optical microscopy. Instead of relying on the tunnelling of electrons, the AFM measures the very small forces between the tip and the sample; initially the tip and sample were in contact. Later versions of AFM used a laser to measure the deflection of the cantilever and therefore, the force exerted by the sample [121]. This improvement allowed non-contact and 'tapping' modes. AFM is a powerful and adaptable tool for the investigation of surfaces including polymers. Since its introduction, several advances have resulted in additional modes, expanding the range of surfaces that can be imaged

and information that can be obtained. The strength of the AFM lies in its ability to measure forces on the pico-newton (pN) scale with high spatial resolution [122].

Figure 22 shows a schematic of a standard AFM [120]. A micro-fabricated tapered tip is mounted on the end of a flexible cantilever with a low spring stiffness/modulus. The tip is brought into contact with the sample and scanned across the sample surface. As the tip interacts with the surface, the laser light is reflected onto a photodetector. Very small forces at the tip deflect the cantilever and the resulting movement in the reflected laser light is recorded and interpreted.

Cantilever deflection is used to measure the forces caused by tip-surface interactions; Figure 23 shows how the cantilever is expected to deflect through the approach and retraction. At relatively long distances (>10 µm), there is no interaction between the tip and the sample surface, therefore the cantilever remains in its natural state. However, once the tip is brought within range of the electrostatic forces (few microns) [123], the tip is attracted forwards the surface, causing the cantilever to deflect. This deflection is interpreted by the AFM as a force. At some distance, the forces will cause the tip to "snap" into contact with the surface. If the tip is moved closer still to the surface, the outer orbitals of the tip and surface atoms will interact and the cantilever will deflect in the opposite direction, measuring a repulsive force. As the cantilever is moved away from the surface, an adhesive force is measured by the deflection of the cantilever towards the surface.

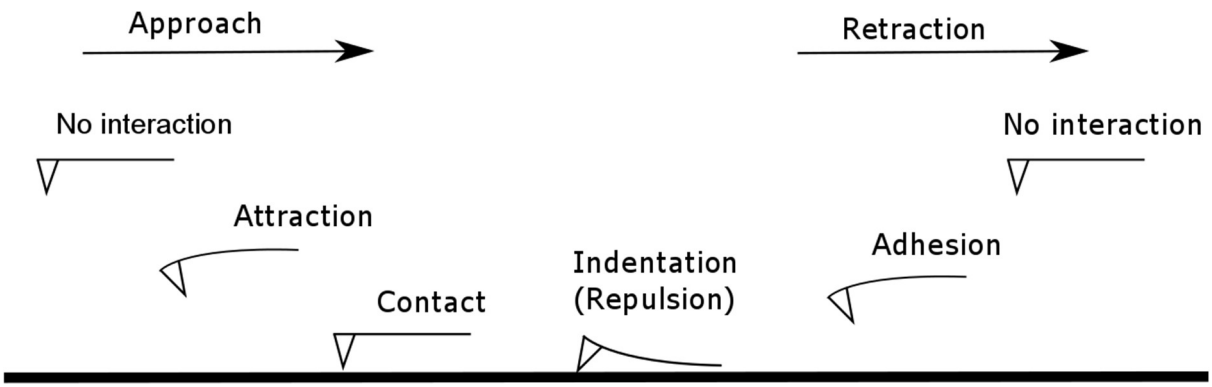

Figure 23: AFM Cantilever deflection during approach and retraction.

A force-distance curve is commonly used to show forces measured by AFM. Figure 24 shows a generalised force-distance curve for illustrative purposes. As the probe tip approaches the sample surface (shown by the red line) it begins at zero force (point A). Eventually, it reaches a point in which force interactions are measurable (point B) and the AFM measures attractive forces and "snaps" to the surface. Moving past this point, the forces quickly become repulsive as the

atomic orbitals overlap and indentation may occur (point C). As the probe retracts from the surface, it follows the slope of the approach data, but then shows a greater attractive force through a longer distance (point D) – this is reported as adhesion.

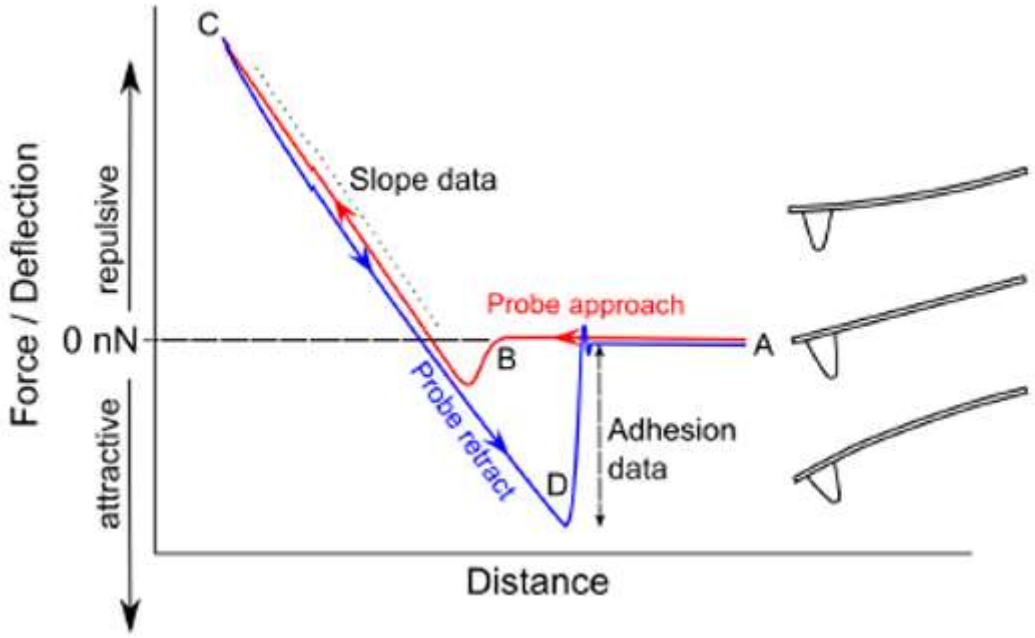

Figure 24: Illustrative force distance curve [124].

Depending on the distance between the tip and sample, different forces dominate the tip-sample interactions. Table 6 shows some of the main forces.

Table 6: Main forces measured by AFM [122], [125]–[127]

Type of force	**Typical distance**
Electrostatic	100 nm
Van der Waals	10 nm
Capillary	2-50 nm
Hydrogen bonding	0.2 nm
Contact (elasticity and viscosity)	0.1 nm
Born repulsion (overlap of orbitals)	0

The low spring stiffness/modulus of the cantilever ensures that small forces can be measured. Indeed, as the cantilever and tip approach the surface, long-range forces such as electrostatic forces will deflect the cantilever. Cantilevers may be around 125 µm in length, though they may be shorter than 10 µm or longer than 500 µm for specialist applications [128]. AFM are usually set up to measure multiple properties at the same time.

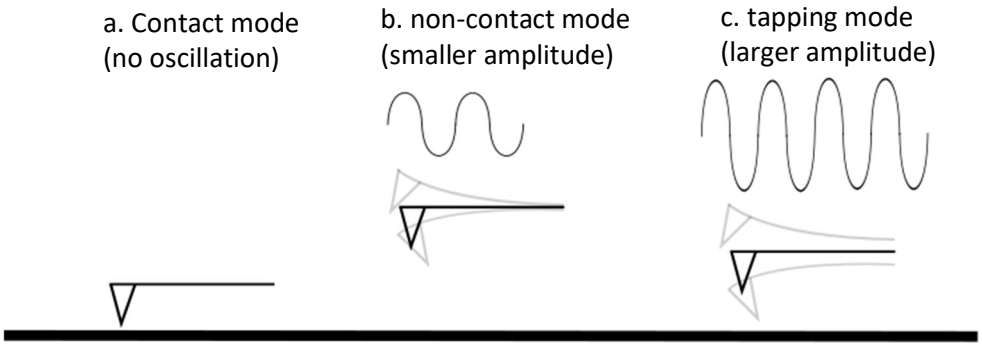

Figure 25: Comparison of tip locations and oscillation amplitude of AFM modes.

3.2.3 AFM Modes

AFM can be operated in several different modes. Each has advantages and disadvantages and gives different types of information. The relevant modes are summarised here.

3.2.3.1 *Contact Mode*

AFM was introduced in contact mode in 1986 as an extension of Scanning Tunnelling Microscopy (STM) [119]. The tip is moved into contact with the sample surface and then moved along the surface while maintaining a constant force [125] (Figure 25 a) without oscillation [129]. This mode allows reconstruction of a topographical image, as well as gathering friction data [120]. However, because the tip is in contact with the surface of the sample, it can introduce contamination and both the tip and sample may be damaged [126].

3.2.3.2 *Non-contact mode*

Non-contact mode AFM was introduced in 1987 [130]. In non-contact mode the tip does not touch the sample surface (Figure 25 b). Instead, the cantilever with the tip at the end is vibrated at its resonant frequency with a tip-sample distance of 30-150 Å. This method does not give the friction information available with contact mode but is not damaging to the sample surface. This can be used for topography of very delicate samples – such as biological cells [131]. However, the topography is less reliable and can have reduced resolution. As the tip does not touch the sample, contamination of dirt or liquid condensation can be more difficult to distinguish from the true sample. Additionally, the lateral resolution is reduced compared with contact mode due to the longer tip-sample distance [126].

3.2.3.3 *Tapping mode*

Tapping mode sought to combine the advantages of contact and non-contact modes. As in non-contact mode, the cantilever is vibrated at near its resonant frequency. However, in tapping mode, the amplitude is much larger (Figure 25 c). The distance is such that at the lowest point in

the oscillation, the tip briefly comes in contact with the sample surface. Because the probe is only in contact with the surface for a fraction of a second, the dragging action is minimised – along with damage to the sample, making this mode particularly beneficial for use with soft samples [122][123]. The tip-surface forces recorded during the oscillation cause alteration of the amplitude, phase and the frequency of the oscillation. In this way, topography, phase and amplitude data are simultaneously collected and mapped [120]. Friction data is not available in this mode.

3.2.3.4 *Kelvin Probe Force Microscopy (KPFM)*

Following on from using the Atomic Force Microscope in tapping mode, it became possible to measure charges on the surface [134], [135], Kelvin probe force microscopy was introduced in 1991 [89]. This allowed high resolution mapping of contact potential differences. Kelvin Probe Force Microscopy is a variation of AFM that uses amplitude modulation to detect the surface potential [136]. In this method, the cantilever is vibrated at a known frequency. As electrostatic forces interact with the tip, the change in amplitude is measured and converted into an image of surface potential. The vibrating tip oscillates through a range of tip-sample distances. At the peak, the tip-sample distance is largest, and surface-tip interaction at its lowest. At an oscillation minimum, the tip-sample distance is at its minimum value, while sample-tip interaction is at a maximum. Unfortunately, if tips with comparatively large mass are used, the effects of the oscillation can overwhelm the signal used to determine surface potential [136]. Additionally, at large tip-sample distances, the side interactions are not negligible. However, at small tip-sample distances (less than 10 nm), the electric field strongly concentrates at the tip apex [137] making the forces at the side of the tip less relevant. In order to maximise this effect, the tip and cantilever should be carefully chosen. It has been reported that a long, slender, slightly blunt tip attached to a cantilever of minimal width and surface area [138].

Due to the way KPFM (or sometimes called KFM) measures surface potential, there are two modes, KFM – AM and KFM – FM [139].

> *"For the detection of the electrostatic force, an a.c.-voltage with a frequency ω is applied between tip and sample. Two different methods can be employed for the measurement: the frequency modulation (FM) mode or amplitude modulation (AM) mode detection. In FM-mode the oscillation of the frequency shift at ω is measured, which is proportional to the gradient of the electrostatic force. In AM-mode the amplitude of the cantilever oscillation at ω is measured which is proportional to the electrostatic force itself."* [140]

Although AM appears to be the more direct measurement, the FM measurements are more suitable for extremely flat samples as the tip must be kept much closer to the surface (<30 nm) [139]. Although AM mode can tolerate the tip farther from the surface, increasing the tip-sample distance for both methods increases the error. And, with AM-KFM, the measured surface potential is always smaller than the actual value due to errors in the measurement and the effect of averaging over a larger area [139][140]. The KPFM mode used in this work is AM-KFM due to the topographical differences in the exposed samples.

Using KPFM, a variety of information can be mapped simultaneously. Precise mapping of the surface potential differences can be achieved together with the topography [79][127]. In some configurations other electrical properties can also be measured, including capacitance (CSAFM, Section 3.2.3.5) [120][125][131][132]. It is particularly important to map the electrical properties of the coatings because current understanding links the electrical resistance to the corrosion performance [13][72][77][133]. However, KPFM is a surface method and cannot measure the electrical current (and therefore resistance) through a sample like current sensing AFM (CSAFM).

3.2.3.5 *Current Sensing Atomic Force Microscopy (CSAFM)*

Current Sensing AFM is a contact mode with the ability to investigate the resistance between the tip and a plane electrode (usually the substrate) [144]. In CSAFM a conductive tip (usually Pt coated) and a conductive substrate [145]. The tip is in contact with the sample and the circuit is completed by a connection to the substrate. A constant voltage (called bias voltage) is applied to the sample and the tip is kept at a virtual ground to measure the current as well as topography and friction [120]. This difference between the charge produced at the tip and the ground at the substrate is the bias, which can be positive or negative. The resolution for electrical features is a few nanometres [144].

It is hypothesised that heterogeneity of the electrical resistance of a coating will relate to the microstructure within the coating and the corrosion performance. The resistance in air is less than the resistance of a polymer, so areas of lower density would be expected to have lower resistance than areas with more densely packed polymers. However, the microstructure of the polymer is also expected to play a part. As discussed in Section 5.3, p82, the formation of polyester microgels during curing may encapsulate more hydrophilic chain ends and therefore concentrate the ions that are expected to increase conductivity through the polymer. These structures are key areas of interest in this work. However, challenges exist in preparing samples such that enough current passes through the sample to be detected.

3.2.4 Mapping types

3.2.4.1 *Topography*

A topographical map is produced by the vertical movement of the scanner in either contact or tapping mode [129]. From this data, surface roughness can be calculated.

3.2.4.2 *Phase*

The phase image is constructed by comparing the recorded oscillation of the cantilever with the expected oscillation (Figure 26) [146].

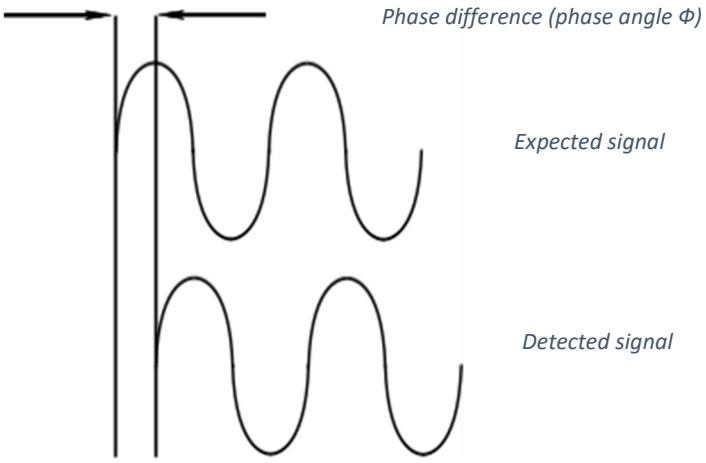

Figure 26: Simple illustration of phase shift in atomic force microscopy

If the surface is highly uniform, the phase difference will also be uniform, and the resulting image will not show features. Therefore, phase imaging relies on changes in the phase difference in different locations rather than purely the difference from the expected signal. Phase imaging aims to map the differences in friction, adhesion and viscoelasticity [129]. However, topographical variations can also cause artefacts in the phase image. For example, a valley may show increased adhesion due to increased contact area without the chemical and mechanical differences phase is designed to detect [129]. It has been reported that the phase shift is caused by multiple forces combining to cause energy dissipation [146].

3.2.4.3 *Friction*

Friction is measured using the lateral forces detected by the AFM. Variations in frictions will cause a twisting motion on the tip and cantilever [120]. This twisting motion is reported in volts. Topography will also influence the reported friction data.

Although basic contact modes are not commonly used. Friction data can be mapped from CSAFM. Additionally, friction data from AFM or Scanning Force Microscopy (SFM) can be useful in tribological studies of materials [147].

3.2.4.4 *CSAFM (Current map)*

The CSAFM image is constructed using the current measured between the sample electrode (usually the substrate) and the AFM tip [120].

3.3 SUMMARY

The Alicona Infinite Focus 3D microscope is a powerful tool for looking at surfaces on the microscale. AFM is a remarkably flexible tool for interrogating sample surfaces (and some internal structures) on nanoscales. Combining the information from these two instruments should give a good picture of the sample surface and structure.

4 EXPERIMENTAL METHODOLOGY

In this section, some of the variations on experimental methodology will be discussed. After refining the methods over several attempts, results from two methods will be presented in this work. Both methods will be presented in this section.

The first set of samples had less surface preparation of the steel, and used a spin coater to apply the resin. This method was generally unable to reduce the thickness beyond approximately 15 µm.
Sample set 1: spin coated, approximately 15 µm thickness

The second set of samples used a more highly polished surface and were cured under a coverglass to reduce the thickness beyond what was achievable by spin-coating.
Sample set 2: cured under coverglass, 5 µm thickness

4.1 THEORY AND MACROSCOPIC PRECEDENT

For details on industrial selection and applications, see Section 2.5.
For details on academic application and testing, see Section 2.6.

4.2 POLYMER SELECTION

Many different coating chemistries are used in industrial, marine and anti-corrosive coatings. It was not initially clear which would enable the clear interrogation of surface and microstructural features. Both epoxy-amine and isophthalic unsaturated polyester-MEKP were considered, however initial testing showed epoxy-amine polymers to be unsuitable due to lack of visible changes in the surface in the time allotted. Isophthalic unsaturated polyester polymers were selected and epoxy-amine coatings will not be discussed further.

4.2.1 Isophthalic unsaturated polyester polymers

As discussed in Section 2.1, unsaturated polyester polymers are a condensation polymer resin in styrene initiated with an organic peroxide. Microstructures do form during the crosslinking process, as reported in literature [18][39][46][56][57] (Section 2.1.4.2). This will be confirmed by the results discussed in Chapter 5.

Several different unsaturated polyester resins were screened for use in this work. All resins and crosslinking agents used are commercially available. Table 1, p15, gives some of the typical

properties of the unsaturated polyester resins used in this work compared with others. The unsaturated polyester resin chosen is commercially available and is marketed as a base resin without the acceleration and thixotropy additives. To preserve commercially sensitive information, specific brands and product names of commercially available materials are not disclosed.

All commercially available unsaturated polyester resins are comprised of unsaturated polyester blended in styrene (or similar reactive diluent). It is not possible to examine the properties of the individual components. Some research groups have removed the styrene by vacuum evaporation, but this would certainly leave traces which may interfere with high-resolution techniques such as AFM. Attempts to synthesise a pure unsaturated polyester polymer similar to the commercially available polyester resin were unsuccessful as the parameters must be tightly controlled to produce the desired molecular weight. This proved not to be feasible within the working day with available equipment.

4.3 Polymer formulation

All components of the formulation are commercially available. The unaccelerated, non-thixotropic isophthalic resin was first accelerated by mixing 800 g of resin with 1.2 g of 10% solution of dimethylanaline (DMA) in styrene and 1.2 g of cobalt (II) 2-ethylhexanoate, 6% Co, in an aromatic solvent mixture. The accelerated resin is stable at room temperatures for at least several months.

4.4 Sample preparation and crosslinking

4.4.1 Sample set 1 – for Tapping mode AFM and KPFM

BS EN 10130 DC01[1] steel plates (see Section 2.2), with dimensions 40 mm × 40 mm of were cut from a 1 mm thick sheet with a guillotine. Each plate was wiped with xylene and a lint-free cloth. After drying, the plates were rinsed in a bath of methanol and dried following the Japanese Industrial Standard (JIS Z 2371). No abrasion was used, so the substrate profile was typical for cold-rolled steel according to BS EN 10130 DC01. Alicona measurements indicate a profile of less than one micrometer (see Figure 32 and Figure 33, p65) Abrasive blast cleaning was attempted, but the treatment caused the panels to deform. To produce the thinnest coating possible, a custom spin-coater was used.

[1] Not generally alloy quality steel: max C 0.12%, max P, S 0.45%, and max Mn 0.6%

These samples were spin coated, but coating thickness varied too much to reliably determine the resistivity. As soon as the activator is added to the resin, the viscosity begins to increase. As multiple samples were coated from the same sample, the resulting thickness of the coating increased. Samples from early in the coating run were used to keep the thickness and variation to a minimum. Typical thicknesses were around 15 µm, but could vary by several micrometres.

4.4.2 Sample set 2 – for CSAFM

Electrical resistance is directly related to the thickness of a polymeric coating. After several attempts with a combination of spin coaters and surface tension reducing additives, it was not possible to make the coating surface completely flat. Nor is it possible to map the coating thickness. Therefore, it was decided that the best solution would be to control the flatness of the surface at the interface and map the topography - which would relate to the coating thickness. For the CSAFM samples, the metal surface (BS EN 10130 DC01 steel, in 20 mm squares) was polished with decreasing sized grit, finishing with 1 µm. This gave the surface a mirror-like appearance. This surface was rinsed with acetone to remove dust and allowed to evaporate prior to coating.

To achieve tightly controlled 5 µm thickness, precision milled stainless steel shims were placed on the polished surface (Figure 27), the initiated resin was dropped onto the surface and then a clean microscope coverglass was placed on top. In order to counter the tendency of the resin to gather and push up the coverglass, a nut of 10.3g was placed on top (Figure 28). However, it is unclear how the tendency of the resin to shrink (around 2%) during cure would affect the final thickness. Glass was an ideal surface for the top of the sample as the cured polymer is well known to have low adhesion to glass and could generally be removed intact with little force. Obviously damaged samples were discarded. A finished sample is shown in Figure 29.

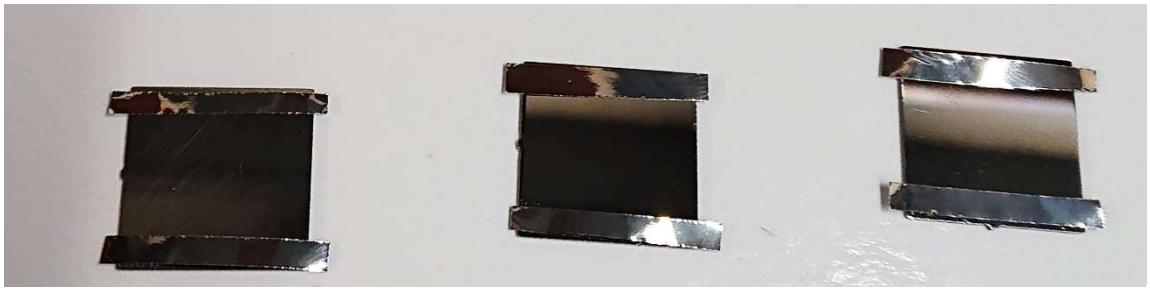

Figure 27: polished samples with 5 µm spacer shim

Figure 28: polished samples with stainless steel spacer shims, coating, coverglass and 10.3g weight (nut)

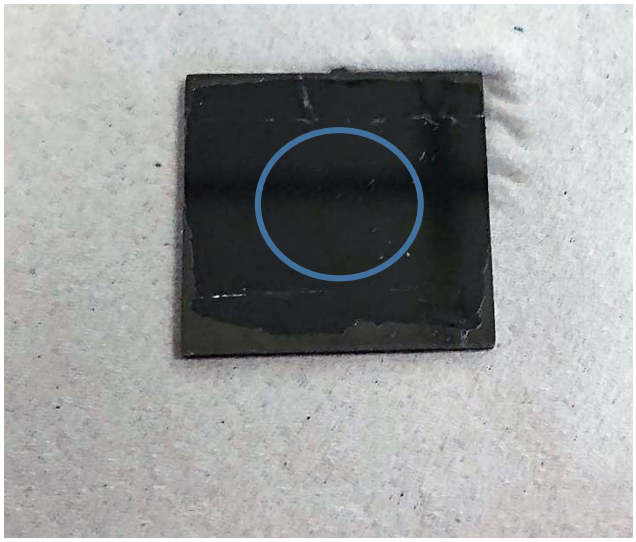

Figure 29: coated sample after the coverglass is removed, target CSAFM test area is circled in blue

4.4.3 Curing

To initiate the crosslinking reaction, 2% (by weight) of MEKP was mixed with the resin sample immediately before coating. Polyester samples were cured at ambient conditions. As these types of coatings are commonly used in a variety of field applications at a wide range of temperatures, this is not expected to cause any issues or performance differences. Samples (except for 5 µm thickness) were prepared in uncontrolled ambient lab conditions. During the sample preparation, the ambient temperature in the lab varied considerably, from 21°C to 28°C. This caused some variation in pot life. This was noted as approximately 10 samples were coated with each mixture using the spin coater. They tended to increase in thickness, presumably due to increasing viscosity during crosslinking. To minimise this issue, the samples selected were from the start of each coating run.

For the 5 µm thickness samples, the ambient temperature was more tightly controlled around 23°C.

4.5 Coating Thickness

Initially, the samples were measured for coating thickness using Elcometer 456 (see Aside 2 [148]). The samples were then weighed to determine thickness more accurately. Each metal sample was weighed

Figure 30: Elcometer 456 Coating thickness Gauges (see Aside 2) [148]

to four decimal places using an analytical balance (Ohaus Adventurer AR2140). The metal was then coated and the polymer cured. The final piece was weighed again. The area of each sample was measured using a metal ruler. The cured density of the resin was measured using water displacement method in a graduated cylinder. Using this data, the film thickness was calculated. However, this is an average thickness and does not map the thickness.

> *Aside 2: **Electromagnetic Induction Coating Thickness Gauges***
>
> *"Electronic coating thickness gauges for measuring on magnetic substrate materials use the electromagnetic induction principle. A three-coil probe system is used where the central coil is powered by the instrument and the other two coils, either side of the central coil, detect the resulting magnetic field. The signal generated by the instrument is sinusoidal and therefore an alternating magnetic field is established round the central coil."*
>
> *"When there is no magnetic materials [SIC] influencing the probe then the magnetic field cuts through the other two coils equally. As the probe is brought closer to the uncoated substrate the field becomes unbalanced with more field cutting the nearest coil and less cutting the furthest coil. This produces a net voltage between the two coils which is a measure of the distance to the substrate (the coating thickness)."*

4.6 Salt Fog Exposure

An Ascott cc450ip (Figure 31), commercially available salt fog chamber, was running ASTM B117[2] neutral salt fog. In order to minimise edge effects on small pieces caused by accumulation of condensed salt solution on the holder, each piece was connected to a larger plate by a small magnet. The plates were then arranged at the appropriate angle in the salt fog chamber holders. The samples were exposed to salt fog for a specified amount of time (15 mins to 4 h). After exposure, they were rinsed in deionised water and dried to remove salt and discontinue any corrosion reaction. For operational reasons, samples were examined by Alicona and AFM two to three days after the initial salt fog exposure. It was not possible to examine the same location on

[2] 35°C, 5% sodium chloride solution, 1-2 mm h^{-1} fallout, pH 6.5-7.2

samples before and after exposure, so unexposed samples were examined alongside those exposed to salt fog.

Figure 31: Ascott cc450ip salt fog chamber.

4.7 Atomic Force Microscopy

An Agilent AFM 5500 was used in AC mode. As a starting point, tapping mode was chosen to examine topography and phase of the samples. The cantilever frequency was auto-tuned to 300 kHz. As a major aim of this work was to determine suitable methodology, scan sizes from 1 µm to 50 µm were explored. The speed was generally 1.9 lines per second, but lower speeds were also used.

Pointprobe® – silicon SPM-sensor NCHR[3] AFM probes produced by Nano World were purchased from Windsor Scientific. The Agilent AFM 5500 was also used in KPFM modes (see Section 3.2.3.4). KFM FM mode did not give clear images and will not be presented. KFM AM was more suitable for polymer imaging and initial images are presented in Section 5.2.2. The changes in topography of the unsaturated polyester coating samples after exposure to salt fog may be the reason that results were difficult to obtain with KPFM-FM, as mentioned in Section 3.2.3.4, this method requires the tip to be kept very close to the surface – which is difficult for samples that are not extremely flat.

[3] Typical technical data: Thickness 4 µm, length 125 µm, width 30 µm, resonance frequency 320 kHz, force constant 42 N m^{-1}, detector side is Al coated

For CSAFM, a platinum coated conductive tip was used (Bruker OSCM-PT-R3). The nose cone had a preamp sensitivity of 0.1 nA V^{-1}. A suitable set point was determined from a force-distance curve at each scan location. A variety of sample bias voltages and tip bias voltages were explored, and the most successful results will be presented in Chapter 6.

4.8 Alicona InfiniteFocus 3D optical microscope

To supplement the information gained by the AFM, an Alicona InfiniteFocus 3D optical microscope was used. This allowed the visualisation of larger sections of the sample- up to 6mm across.

4.9 Supplemental Images

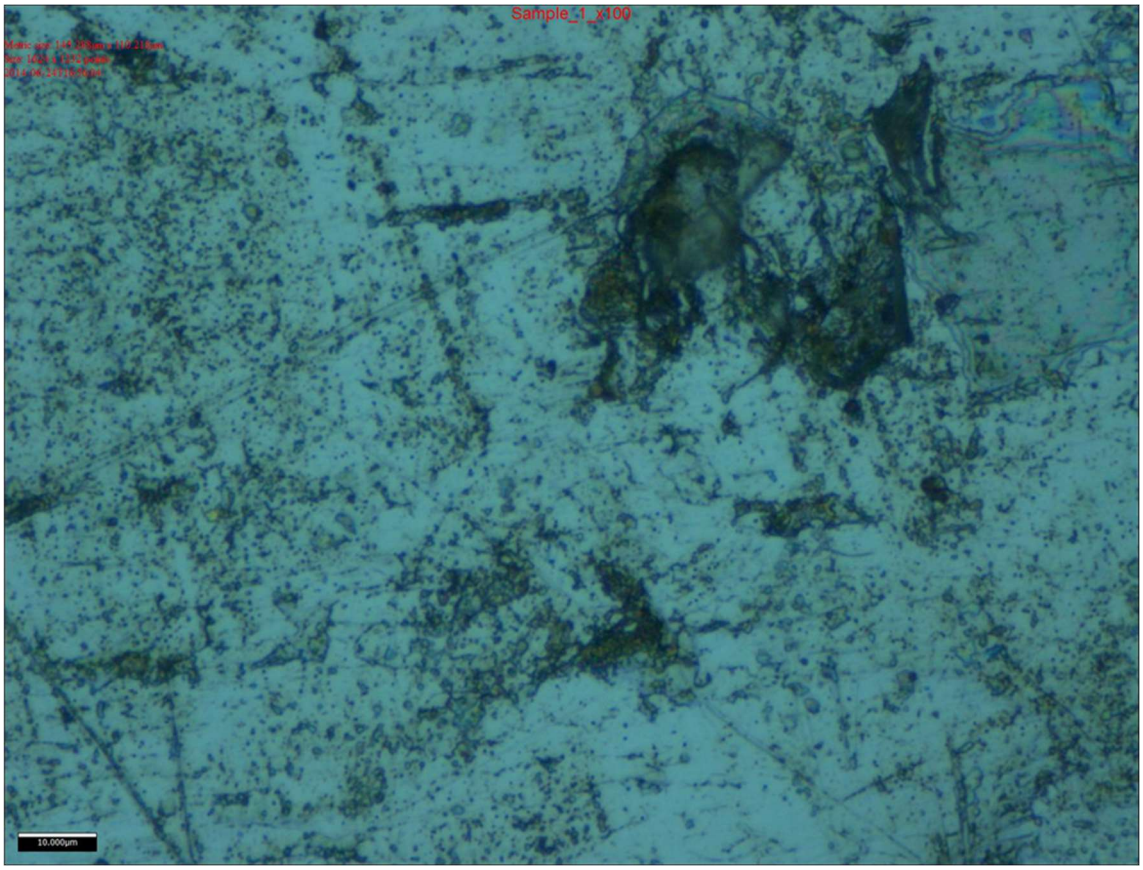

Figure 32: BS EN 10130 DC01 steel surface – optical image from Alicona Infinite Focus at 100× magnification.

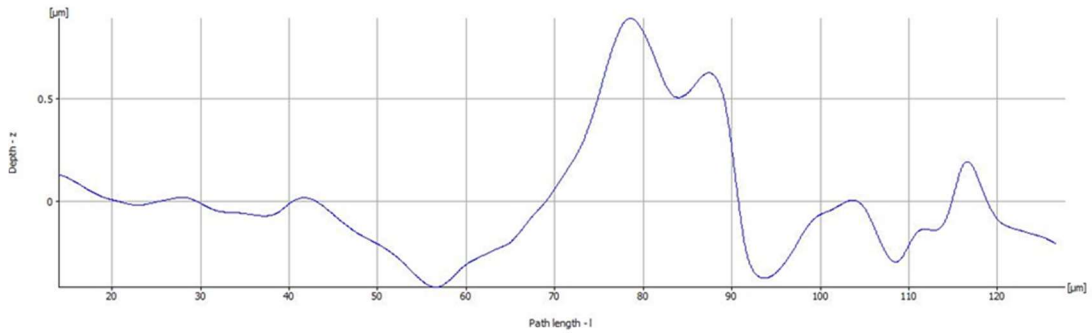

Figure 33: BS EN 10130 DC01 steel surface profile - Alicona Infinite Focus (100×).

5 RESULTS AND DISCUSSION – VERIFICATION OF MICROSTRUCTURE

Samples of commercially available unsaturated polyester resin were spin coated and cured on mild steel plates wiped with solvent (see experimental method for sample set 1 in Chapter 4 for details). The coated samples naturally reached a lower thickness limit of around 10-15 µm. Due to viscosity and wetting properties of the resin, it was not possible to reduce the thickness further by this application method without materially altering the properties of the resin. This limitation is not an issue for surface measurements, but the high resistance of the polymer means that the breakdown voltage may be beyond the capability of the instrumentation.

This chapter details the results indicating that microstructures were detectable optically and with the atomic force microscope (AFM) using minimal exposure to salt fog (ASTM B117: 5 wt.% NaCl, 100% relative humidity and 35°C) and without the solvent washes and cracking required in other studies. This has the advantage of preserving the polymer morphology being investigated, but has less direct investigation of the structures in the bulk of the polymer. This is not ideal, but the electrical properties will be investigated through the polymers in Chapter 6.

5.1 ALICONA OPTICAL MICROSCOPY

Unexposed samples are entirely clear, and the underlying substrate is clearly visible through the coating, but no coating features are visible (Figure 52, p85). A comparison of uncoated and coated steel is shown in Figure 34. After a salt fog exposure of only 15 minutes (Figure 53, p86), structures in the cured film are clearly visible via optical microscopy. Since only a short exposure time leads to marked changes in surface texture, it is hypothesised that these begin immediately on exposure, but the rate of change has not been investigated in this work as it is only used to reveal structures. Artificial ageing generally and ASTM B117 particularly are commonly used methods of evaluating coating performance. However, it is well understood that these methods do not always give results that can be related to real-world performance. In this case, the salt fog is used to reveal features rather than to relate to expected performance over a specified time period.

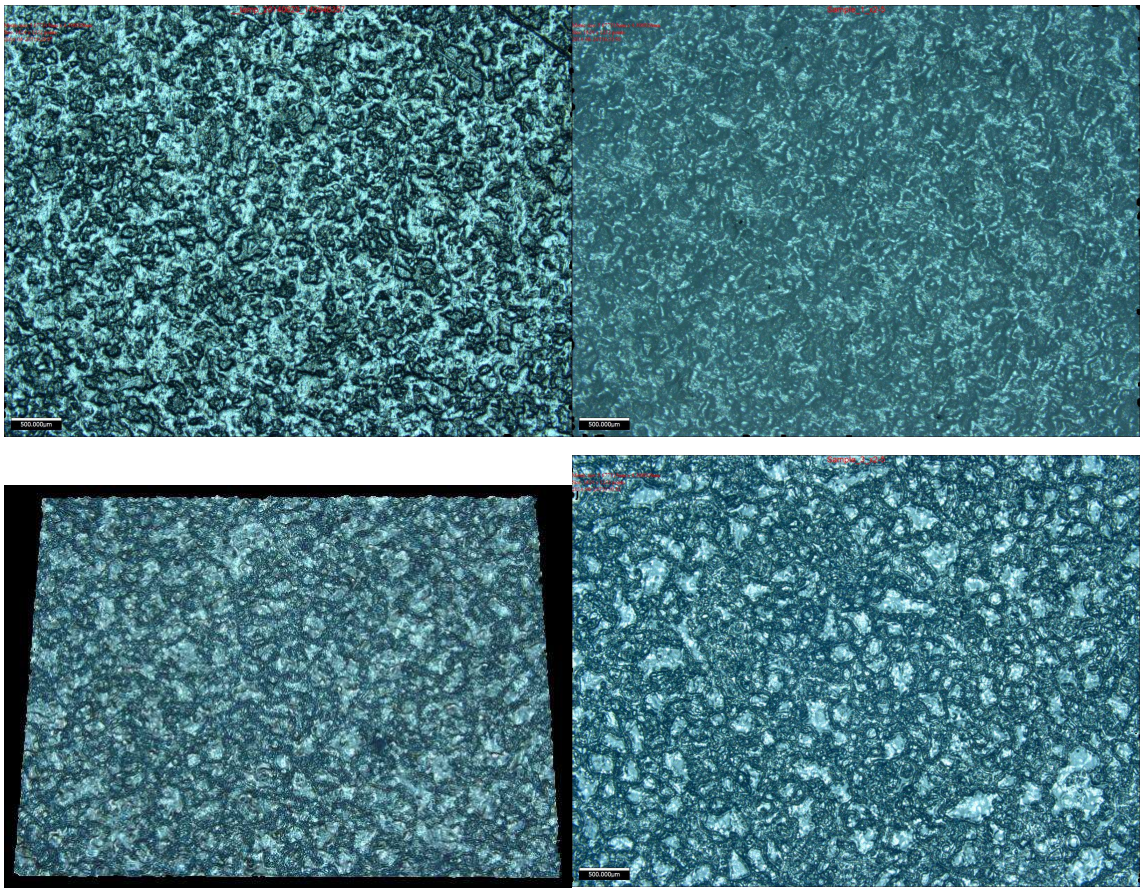

Figure 34: Alicona optical images - 2.5x magnification, top row: uncoated steel surface (left) and coated surface (right), Second row: exposed to salt fog: 15 min (left) and 30 min (right)

After 30 minutes of ASTM B117 salt fog exposure, the polymer samples still remain relatively transparent, and care must be taken to focus the Alicona on the polymer sample surface rather than the steel substrate/polymer interface (both are shown in Figure 35). Although it may seem obvious which is the polymer depth and which is the substrate, it was compared with an image of uncoated steel (Figure 34 and Figure 51). Once the Alicona is focused on the polymer, a two-phase structure is clearly visible.

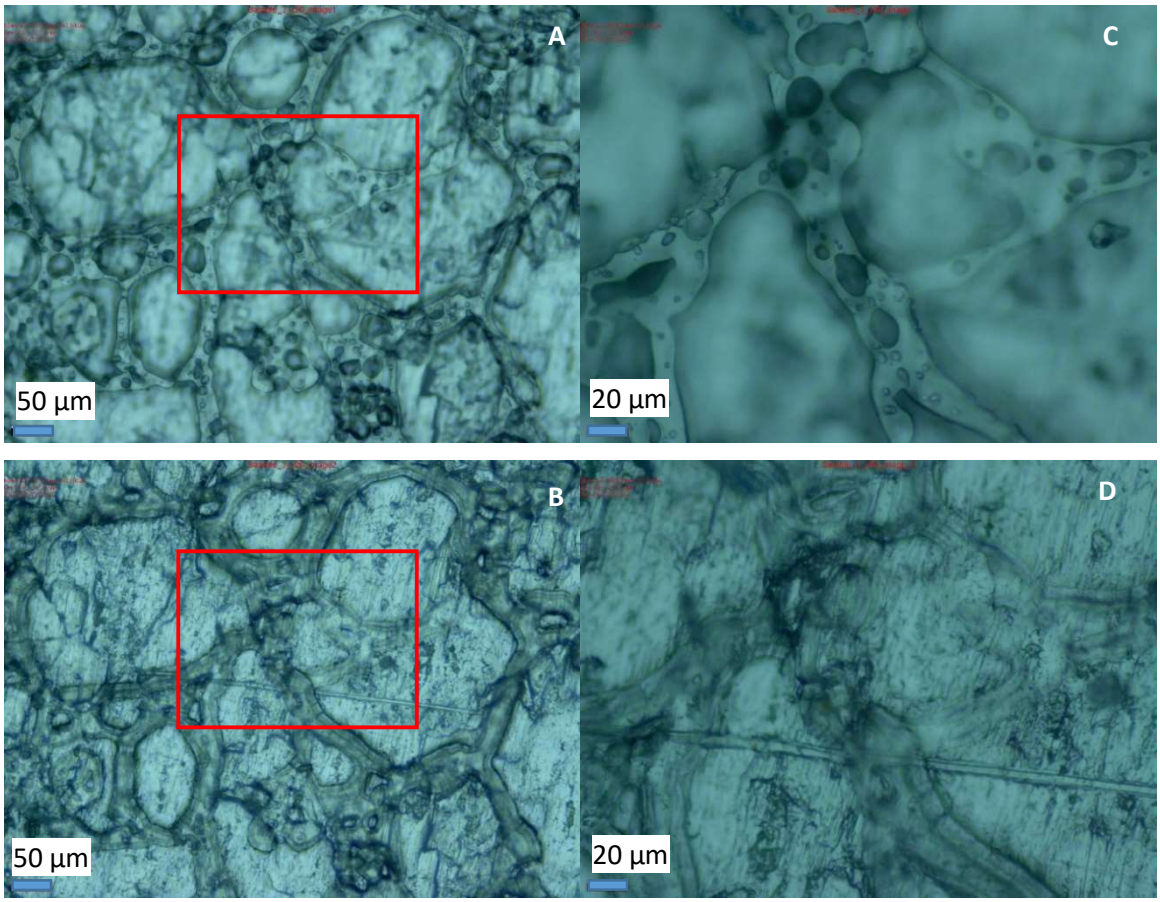

*Figure 35: Non-thixotropic isophthalic unsaturated polyester cured with 2% MEKP, 30 minute salt fog exposure - Alicona Infinite Focus: **A** –focus depth: polymer; **B** –focus depth: substrate; **C** –focus depth: polymer; **D** –focus depth: substrate. Box shown in red in A and B indicates the area of the detail shown in C and D. Image C shows the predicted microgels and branched structure.*

As discussed previously (Section 2.1.4.2) the published literature indicates an expected polymer structure of microgels of unsaturated polyester surrounded by a network of polymerised styrene [19].

Figure 36 (p70, taken from [19]) is an SEM image of a coral-like structure of cured polyester. The structure was found to vary with the degree of unsaturation and styrene content. The degree of unsaturation of this commercial resin is unknown; the styrene content is 45%, but the molar ratio cannot be calculated without the molecular weight of the commercial polymer, which is unavailable. As the structure does not correspond with the flake-like structure found by Yang and Lee [19], it is unlikely that this resin has the low-styrene molar ratio associated with that morphology. Figure 35(C) shows small globules in a branched network. The globules in this image are on the order of 1-20 µm in diameter. These are surrounded by a matrix that appears to branch to other groups of microgels.

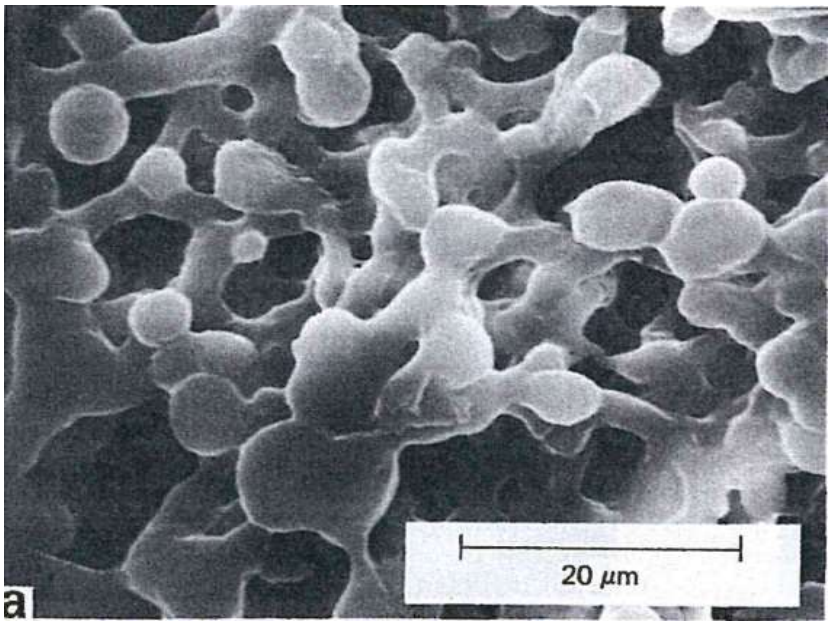

Figure 36: SEM micrographs of ST/S-8 samples with MR=6.67/1 (taken from [19](figure 7))

Although the structure of microgels and polystyrene network have been hypothesised and reported elsewhere, they have not been reported via optical microscopy. Optical methods are large-scale compared to other methods used in this work and by other research groups. Alicona images generally encompass an area of hundreds or thousands of µm square, with a maximum resolution of around 1 µm. Scanning electron microscopy (SEM) bypasses the resolution limitations of optical microscopy by using electrons rather than light to produce the image. While this improves the maximum resolution, it does introduce other limitations. Some samples may be damaged by the beam of electrons itself as it heats the sample. These are generally biological samples, but may also be some polymer samples [149]. SEM requires conductive samples. Non-conductive samples are generally coated with gold or other metals to make an SEM image possible. In some cases, this process can obscure delicate features. The process of depositing the metal can damage the sample itself, or obscure fine detail. Typical coating thicknesses are on the order of 10 nm, so features smaller than that may be obscured. Additionally, SEM is performed in a high vacuum. Again, biological samples risk damage, but polymer samples may also be changed if unreacted monomers with low boiling points (such as styrene) may be removed from the sample unintentionally. Although SEM is a powerful imaging technique, these limitations suggest that polymer microstructures should be confirmed with other techniques.

Yang and Lee attributed the large pores in
Figure 36 (ST/S-8 MR = 6.67 samples) to the unreacted monomers washed away by dichloromethane treatment prior to SEM [19]. They noted that the application of a post-cure

increased the styrene conversion and filled some of the pores observed (Figure 37), unfortunately pore size for either cure schedule was not specifically reported. The samples in this work did not undergo a specific post-cure as this is generally impractical in the field of pipeline coatings. However, the temperature during cure was not controlled and the maximum exotherm is determined by sample geometry (as thin samples will cool faster than samples cast for volume). The degree of cure was not measured, but as these are commercial resins under industrial usage conditions, it is unlikely that severe under-curing would occur.

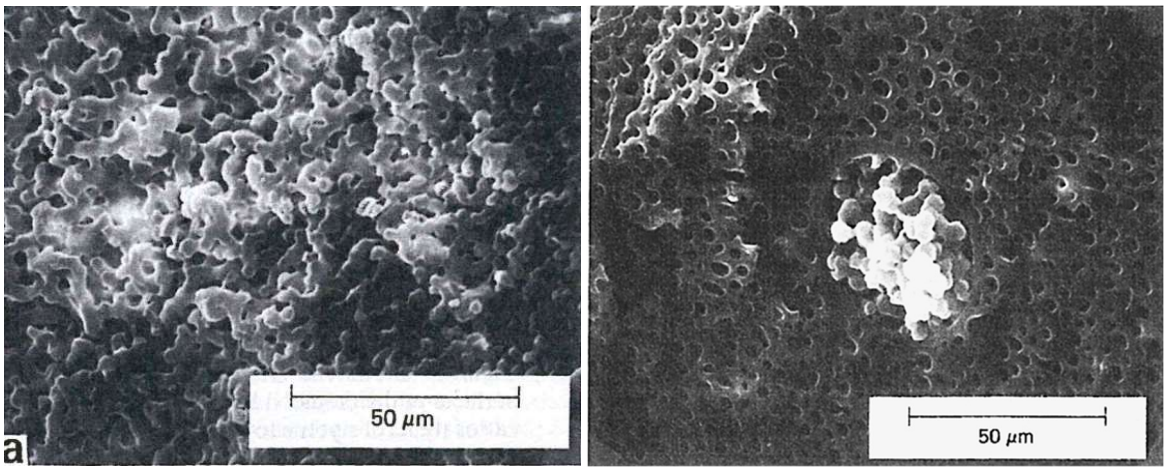

Figure 37: SEM micrographs of ST/S-10 samples with MR = 4/1 before (left) and after (right) post cure of 1 h at 200°C, from [19] (figures 4a and 10),

Even in the post-cured sample, the SEM shows holes in the polymer structure that are up to 5 µm in diameter. These would not be visible without magnification, but would allow water, oxygen, and ions to flow freely through the "protective" coating. In practice, these voids cannot be present in the finished protective coating. Yang, et al attributed these to unreacted monomers, and free chains removed by the dichloromethane treatment [19].

Another group who used a laser to ablate the surface rather than solvent to wash away monomers obtained SEM images suggesting a closely packed morphology of nodules without obvious pores (Figure 38) [26]. At 25 mJ cm^{-2} the styrene polymer is removed, and the polyester remains. This implies that a large portion of the surface polymer is expected to be polystyrene rather than polyester. A closely packed structure indicates that the unreacted monomers and untangled polymers presumed washed out by Yang, et al., may encompass a significant portion of the protective coating. These may represent a weak point in the coating. None of these techniques has the resolution required to see the expected pores of 0.5 nm diameter reported [117]. Alternatively, the apparent microstructure visible in Figure 38 may be due to a surface energy minimisation effect from the laser treatment. Laser ablation has been found to affect the

morphology of polymers [150]. The surface presented may be evidence of damage. This work aims to avoid the damage of surfaces and morphology caused by these treatment methods.

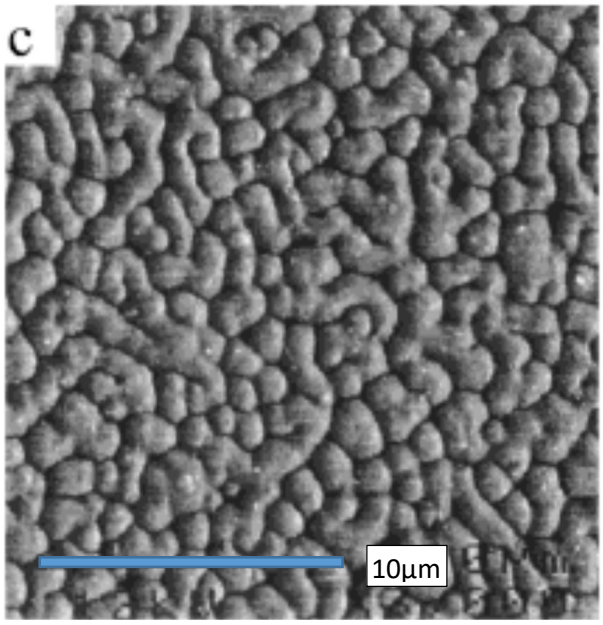

Figure 38: SEM observation of unsaturated polyester G703 material with 45 wt.% styrene (A45 sample) after ArF laser excimer treatment (193 nm radiation) with (c) 25 mJ cm^{-2} (taken *from* [26])*– the closely packed structure shown here indicates that the unreacted monomers and untangled polymers presumed washed out by Yang, et al, in*

Figure 36 may encompass a significant portion of the protective coating.

The 3D rendering images by Alicona InfiniteFocus (Figure 39 and Figure 40) also show changes in the topography of the samples after salt fog exposure following the branched network visible in Figure 35. In Figure 40, the difference between the peaks and valleys is approximately between 30 µm and 40 µm, however, the original total film thickness was measured at only 10 µm. This suggests the explanation is not erosion or pitting of the surface. Much of the polymer surface and branching between nodules is expected to be polystyrene, and that polystyrene is reasonably permeable to water [151], this may be evidence of a swelling phenomenon rather than pitting. Polymers generally are known to swell during water absorption, but they are also susceptible to washing out of monomers or smaller molecules. Though both are possible, on such short timescales water absorption is the more likely phenomenon here.

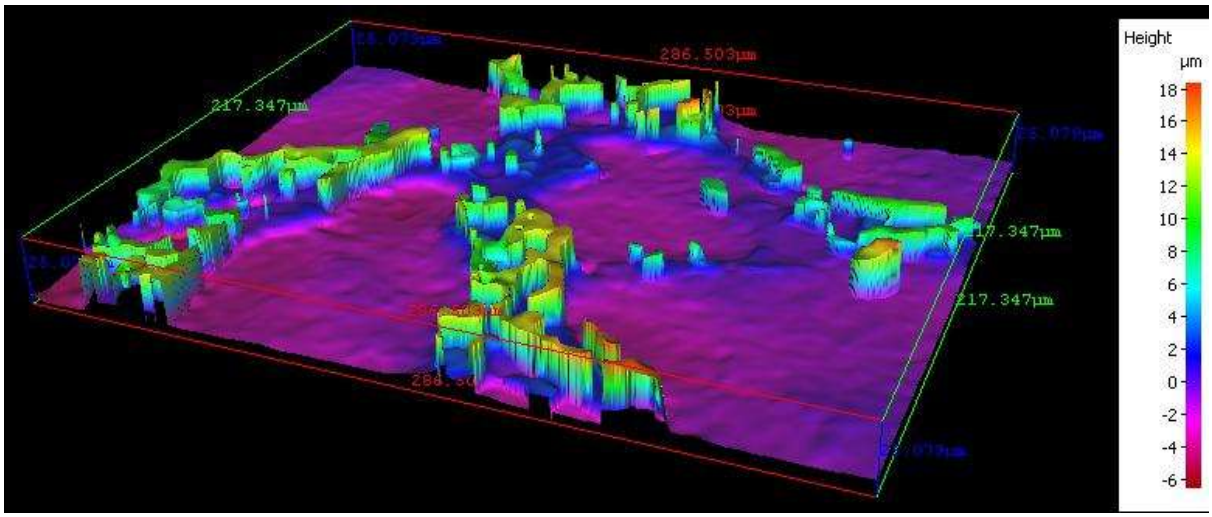

Figure 39: Alicona InfiniteFocus 3D microscope image of the area shown in Figure 35 C, D. The areas expected to be polystyrene branches show raised topography compared to the rest of the polymer after 15 minutes of salt fog exposure. Imaged area is 287 µm by 217 µm.

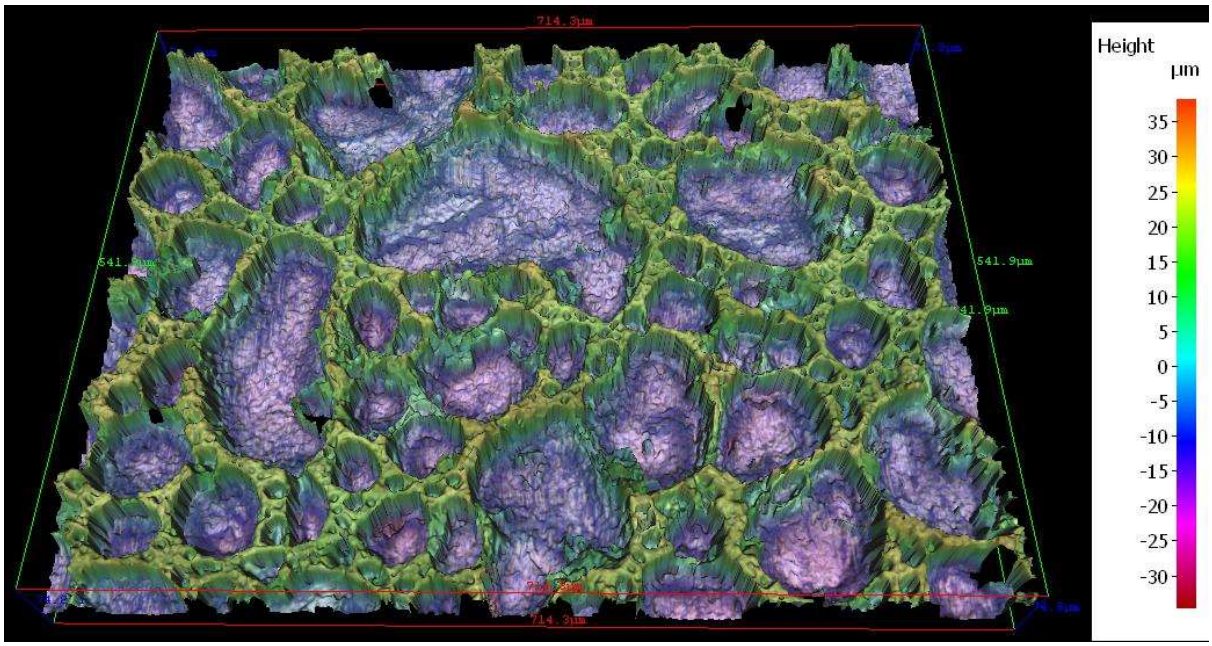

Figure 40: Alicona InfiniteFocus 3D microscope image of unsaturated polyester after 1 h of salt fog exposure. Imaged area is 714 µm wide by 542 µm.

While it seems clear that the topographical changes are caused by a swelling effect rather than an erosion effect, it is unclear how fast these changes progress. A series of images are shown in Figure 41, Figure 42, and Figure 43. It seems the topographical changes do increase with time, though not linearly. There are no reported data for the swelling of unsaturated polyesters in salt fog or water vapour. However, it has been reported that hydrogels of sodium poly(acrylic acid) in a polymer matrix rely on swelling to bridge the distances between microgels and facilitate water transport [152]. Similarly poly(3,4-ethylene dioxythiophene polystyrene sulfonate (PEDOT:PSS)

thin films swell when exposed to water vapour, though in this case the surrounding polystyrene sulfonate shell that swells rather than the PEDOT cores [153].

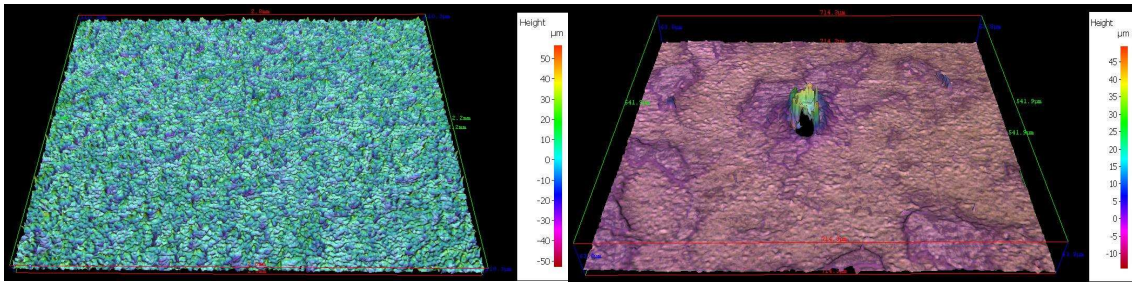

Figure 41: Alicona InfiniteFocus 3D microscope image of unsaturated polyester unexposed to salt fog. Left: 5x magnification, right 20x magnification. Aside from occasional features shown (right) the surface is relatively flat.

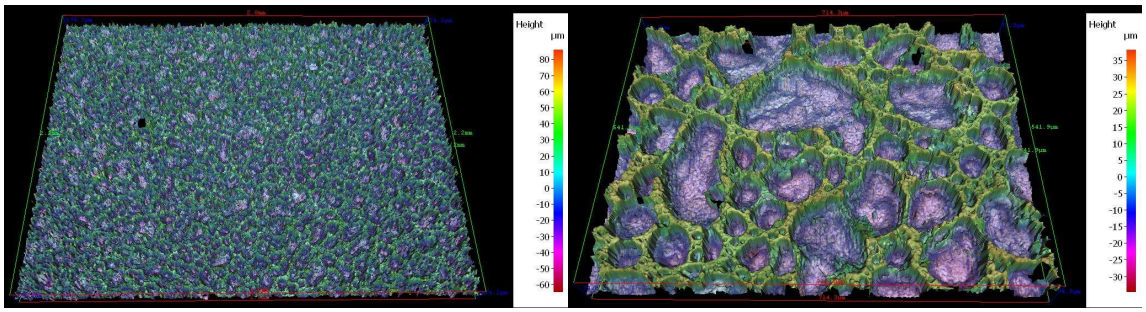

Figure 42: Alicona InfiniteFocus 3D microscope image of unsaturated polyester after 1h of salt fog exposure. Left: 5x magnification, right 20x magnification. The branched structure is clearly showing, though this is expected to be swelling rather than erosion as the difference between peaks and valleys is around 20-30 µm and the original thickness is around 10 µm.

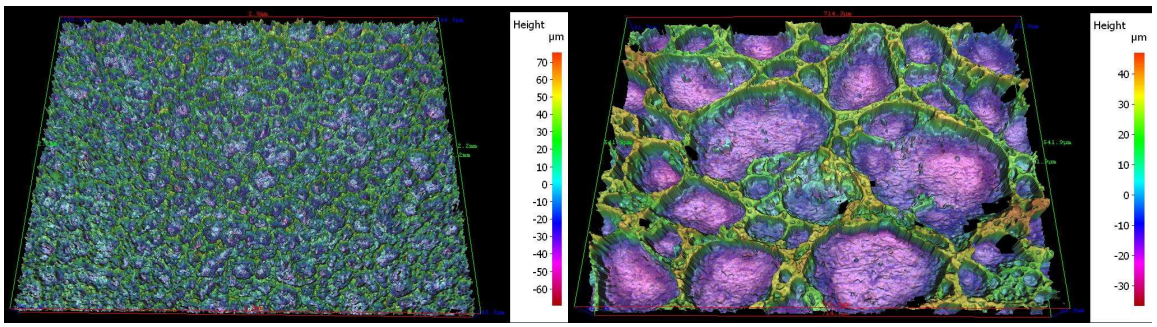

Figure 43: Alicona InfiniteFocus 3D microscope image of unsaturated polyester after 4h of salt fog exposure. Left: 5x magnification, right 20x magnification. The branched structure is clearly showing, though this is expected to be swelling rather than erosion as the difference between peaks and valleys is around 50-60 µm and the original thickness is around 10 µm.

The expected microstructure of unsaturated polyester coatings has been confirmed by optical microscopy with reference to published SEM. In order to consider the effects on a smaller scale, the microstructure was investigated by AFM as well.

5.2 Atomic Force Microscopy (AFM)

Due to the limitations of the vertical movement of the cantilever, AFM scans perform better on small areas without large peaks or valleys. Although exposure to salt fog is purposely used to reveal topographical features in the samples, shorter exposure times reduce these maxima and minima slightly. This improves the ease of scanning by AFM, but may not reveal as many surface structures as longer exposure. However, keeping a short exposure time is justified as features revealed by longer exposures are still undetectable if the topography exceeds the vertical limits of the instrument. The AFM scans of the non-thixotropic isophthalic unsaturated polyester exposed to 15 minutes of salt fog (Figure 44 and Figure 45) show a similar structure to the optical images with sphere-like microgels, or globules and faint 2D rings in the relatively flat amorphous phase.

5.2.1 Tapping mode

AFM images are on a decidedly smaller scale than either the optical microscopy or the SEM images. This presents the opportunity to see features that would not have been visible in the other techniques. Globular structures are clearly visible in both topographical and phase images. These are of a similar shape, but smaller size than those seen by other imaging techniques. This may be due to a wide range of structure sizes present. Faint rings are visible in the phase images, primarily at very small scale and typically 750 nm in diameter (Figure 45, right). These are far too large to be aromatic rings in the polyester's chemical structure (sub-nanometre- roughly 300 picometres), but could be evidence of the expected network of polyester globules connected by styrene bridges previously reported [18][54][56]. It is unlikely that the visible features formed following the structure of the steel below, but a 5 µm tapping mode AFM image of the uncoated steel substrate is provided for comparison in the supplemental images section at the end of this chapter (Figure 55, p87).

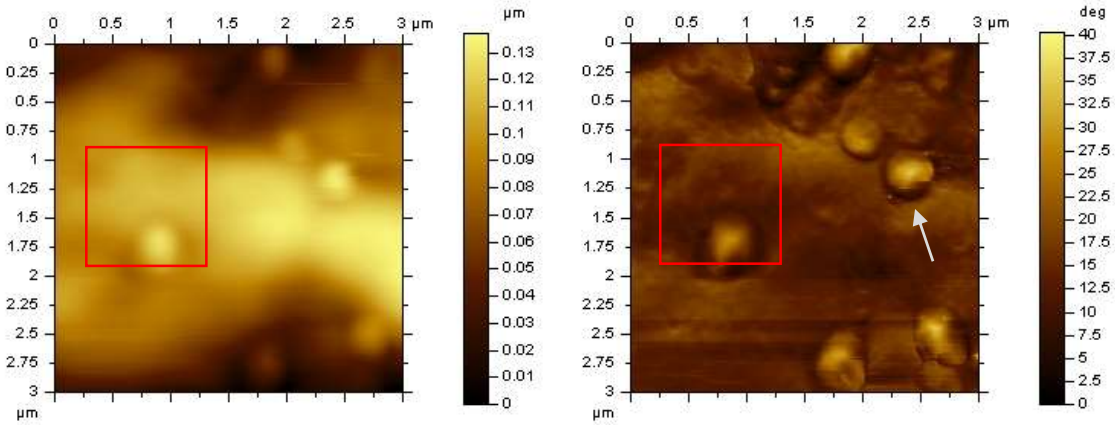

Figure 44: Non-thixotropic isophthalic unsaturated polyester cured with 1% MEKP, 15 minute salt fog exposure - AFM topography (left) and phase (right). Spherical globules with a diameter of around 0.5-1.5 µm are more clearly visible in the phase diagram. One of these globules, which is expected to be polyester, is indicated by the arrow and is visible on a relatively featureless background. Detail contained in the red box shown in Figure 45.

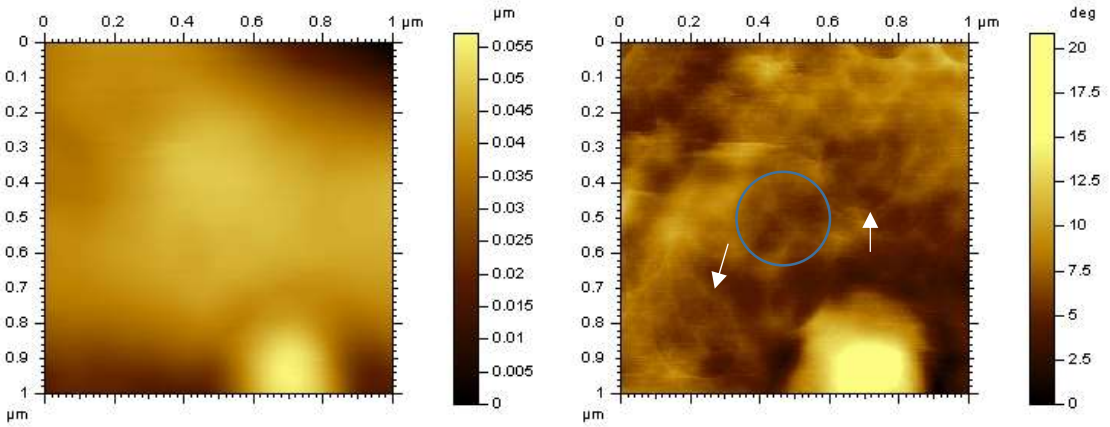

Figure 45: (Detail of Figure 44) Non-thixotropic isophthalic unsaturated polyester cured with 1% MEKP, 15 minute salt fog exposure - AFM topography (left) and phase (right) In this detail image part of a single spherical globule is visible at the bottom of the image in bright yellow. This is expected to be polyester. Rings of approximately 200 nm in diameter are visible in this image. While they are too large to be aromatic rings in the polystyrene, they may be evidence of similarly sized globules in the bulk of the polymer. A single ring is indicated in blue, with two others indicated by arrows.

Overall, the AFM scans show globules surrounded by a less structured background. While the topography is generally flat, there are some overlapping rings of around 200 nm in the phase scan (Figure 45, right). The globule appears to have an approximate diameter of 100-200 nm, which is much smaller than those seen in the SEM or Alicona images above or SEM after ArF laser excimer treatment [26]. However, it is much closer to the value of 30 nm reported by Gu, et al, after the degradation of the film using 3 M NaOH solution for varying intervals up to 50 days [133]. These rings are too large to be aromatic rings in the styrene molecule (which would be around 0.3 nm). They are also too large to be a single coil of unsaturated polyester microgel which is reported to be less than 100 Å (10 nm) [19]. Predicted pores of 0.5 nm diameter [117] are not visible.

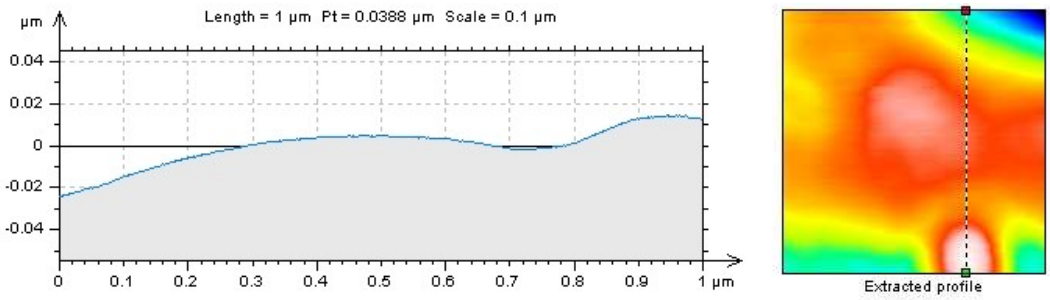

Figure 46: Non-thixotropic isophthalic unsaturated polyester cured with 1% MEKP, 15 minute salt fog exposure - AFM profile of view shown in Figure 45.

The AFM profile (Figure 46) indicates the globules are on the order of 10 nm in height from the surrounding area, however the diameter is larger and it is likely that only part of the globule protrudes from the surrounding resin. This is similar to the average diameter of 30 nm reported

by Gu, et al. in 2001 [133]. Looking at Figure 44 however, the average diameter looks more like 50-100 nm.

5.2.2 Kelvin Probe Force Microscopy (KPFM)

There are theories that once application defects are disregarded, coating inhomogeneity is due primarily to differences in bonding within the polymer film [12]. Unfortunately, this heterogeneity cannot be seen using visual methods. However, the two polymers and even the monomers within the polyester have variations in polarity that may influence the electrical characteristics of the sample. The electrical properties are of utmost interest due to their contribution to their ability to resist or allow the passage of ions and electrical current to complete the corrosion cell. A few test measurements were made to verify the potential of further investigation. All of the images in this section were made using KFM-AM. KFM-AM is more suited to samples with topographical features, but does tend to under-report the surface potential values (see Section 3.2.3.4).

Using KPFM, the surface potential of a coating may be mapped with high spatial resolution. The surface potential gives an indication of the electrical activity at the surface, but does not necessarily give information on the electrical insulation properties of the coating. As one of the main functions of the coating is to provide a barrier to ions, it is important to determine the resistance to current passing through the coating. This will be discussed in Chapter 6.

One of the benefits of AFM, is that multiple properties can be mapped concurrently. Figure 47 shows topography, phase, amplitude, kelvin phase, surface potential, and x-component. This is particularly useful as it has proven essentially impossible with current equipment to pinpoint particular locations or features for further investigation once the sample has been moved out of the imaging area. While the Agilent AFM5500 does have an optical microscope to assist in choosing an area to image, using it to find features on the nanoscale for AFM imaging has proved impossible. Newer AFMs are starting to feature a high-resolution optical scan over a large area to find features in the sample.

Figure 47 shows how multiple layers of information can be simultaneously mapped via KFM with complementary results. The topography scan (top left) shows a gently sloping valley with the hint of some spherical features and a single large globule of around 50nm in height and 125 nm in diameter. The phase image (top right) resolves the large feature into a combination of high and low phase information. The topography is not visible, but the amorphous background is scattered with small areas of higher phase. These may be areas of softer resin as softer resin can cause a

small dissipation of energy if the interaction with the cantilever is not completely elastic. The polyester portion of the cured polymer is expected to be much softer, with a lower T_g than the surrounding polystyrene.

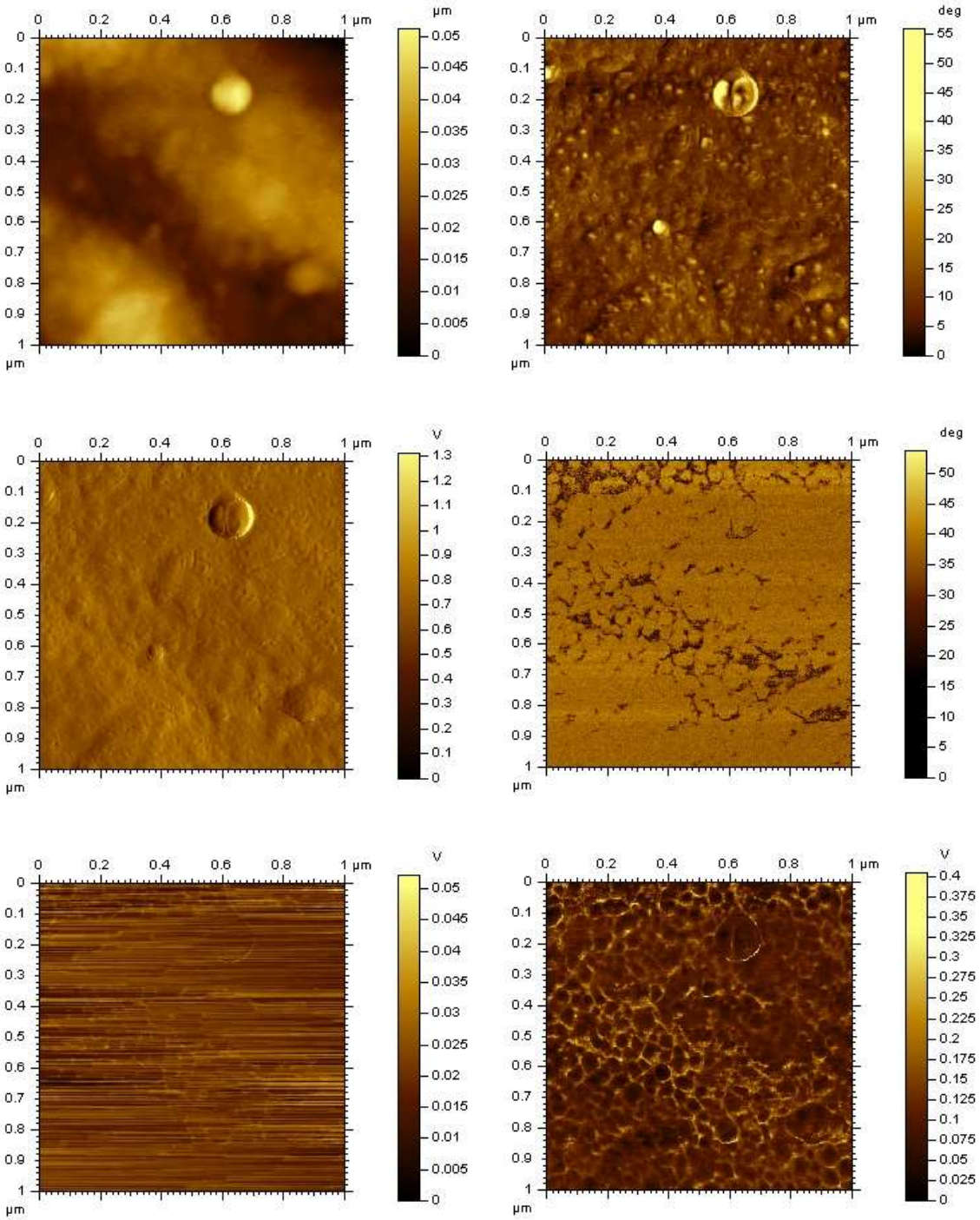

Figure 47: Unaccelerated, non-thixotropic isophthalic unsaturated polyester (15 minute salt fog exposure) imaged in a valley- AFM properties concurrently scanned: Topography (top left), phase (top right), amplitude (middle left), kelvin phase (middle right), surface potential (bottom left), x-component (bottom right)

Amplitude (middle left) shows very little differences across the sample. In KFM-AM mode the error is minimised by keeping the tip a constant distance from the sample and this may restrict the amplitude response [139]. The Kelvin phase (middle right) is recorded from amount the alternating current (AC) signal is out of expected phase. It isn't clear what physical property these data might be related to, possibly a tendency toward ground or a slight electrical dissipation like the regular phase image.

The surface potential image (bottom left of Figure 47) is unfortunately not as clear as desired. However, higher surface potential is visible following the branches of a network. This same network is seen more clearly in the x-component image (bottom right). The x-component is a measure of the forces on the tip in the same direction as the scan movement. Between these two images it seems the surface potential may drag slightly as the tip moves across the surface. The polymer coating is expected to be generally non-conductive, but charges on the surface of the sample might be affected by the tip and voltage as it moves across the surface. If the surface charges produce a drag effect on the tip, that drag would be recorded in the x-component image, which clearly shows more activity in the same branched network as the surface potential image.

The features in Figure 47 appear to support the reported structure of unsaturated polyester microgels (seen in the phase image, top right) surrounded by a network of higher surface potential polystyrene. The polystyrene is expected to have a higher electron density across the polymer due to the aromatic nature of the ring (see Figure 9, p21). As discussed above, all of the features seen here are too small to be single molecules of polyester (~10 nm) or of a benzene ring in the polymer (~0.3 nm).

Interestingly, the x-component image of Figure 47 (bottom right) is very similar to the published image shown in Figure 38, p72. These KFM images add to the weight of evidence confirming the expected structure. This work advances the evidence by providing samples that are not solvent washed, fractured, nor laser ablated. Direct AFM detection of the microstructure of a sample of commercially available, unsaturated polyester coating treated only with a standard accelerated ageing test method has not been reported elsewhere.

It is encouraging to find that electrical differences in the polymer sample can be detected by the AFM. While surface electrical properties may be of interest for determining where water might penetrate first, ultimately the electrical conductivity through the polymer will give the greatest insight into the way electrons move through the coating to complete the corrosion cell.

5.2.2.1 *Additional resin*

In addition to the commercially available, unaccelerated, non-thixotropic, isophthalic unsaturated polyester resin used elsewhere in this work, a similar resin from another manufacturer was prepared in the same way and imaged. This resin was not chosen for further work for several reasons. It remained soft and sticky when cured which was impractical for general use and changes in the curing formulation would be required- thus introducing questions on the comparability of the two resins. The cured polymer remained completely clear after salt fog exposure and no Alicona images of the polymer could be obtained. However, the samples remained relatively flat and a large scan was obtainable (see Figure 48). Obviously, the disadvantage of the large scan is that small features are not visible. However, it is interesting to see how the surface potential is concentrated across a broad swathe of this resin, rather than evenly spaced in a small network. The principles of surface potential are discussed in Section 3.2.3.4. It is unclear what would cause this concentration, though each commercial resin is likely to have slightly different phase separation as well as other properties.

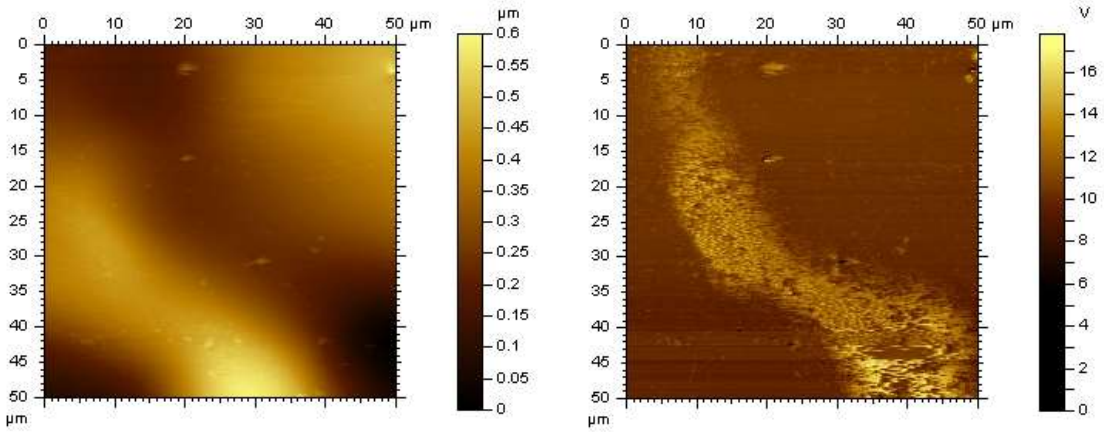

Figure 48: Alternative commercially-available, unaccelerated, non-thixotropic isophthalic unsaturated polyester – topography (left) and KFM AM surface potential (right) exposed to 30 minutes ASTM B117 salt fog

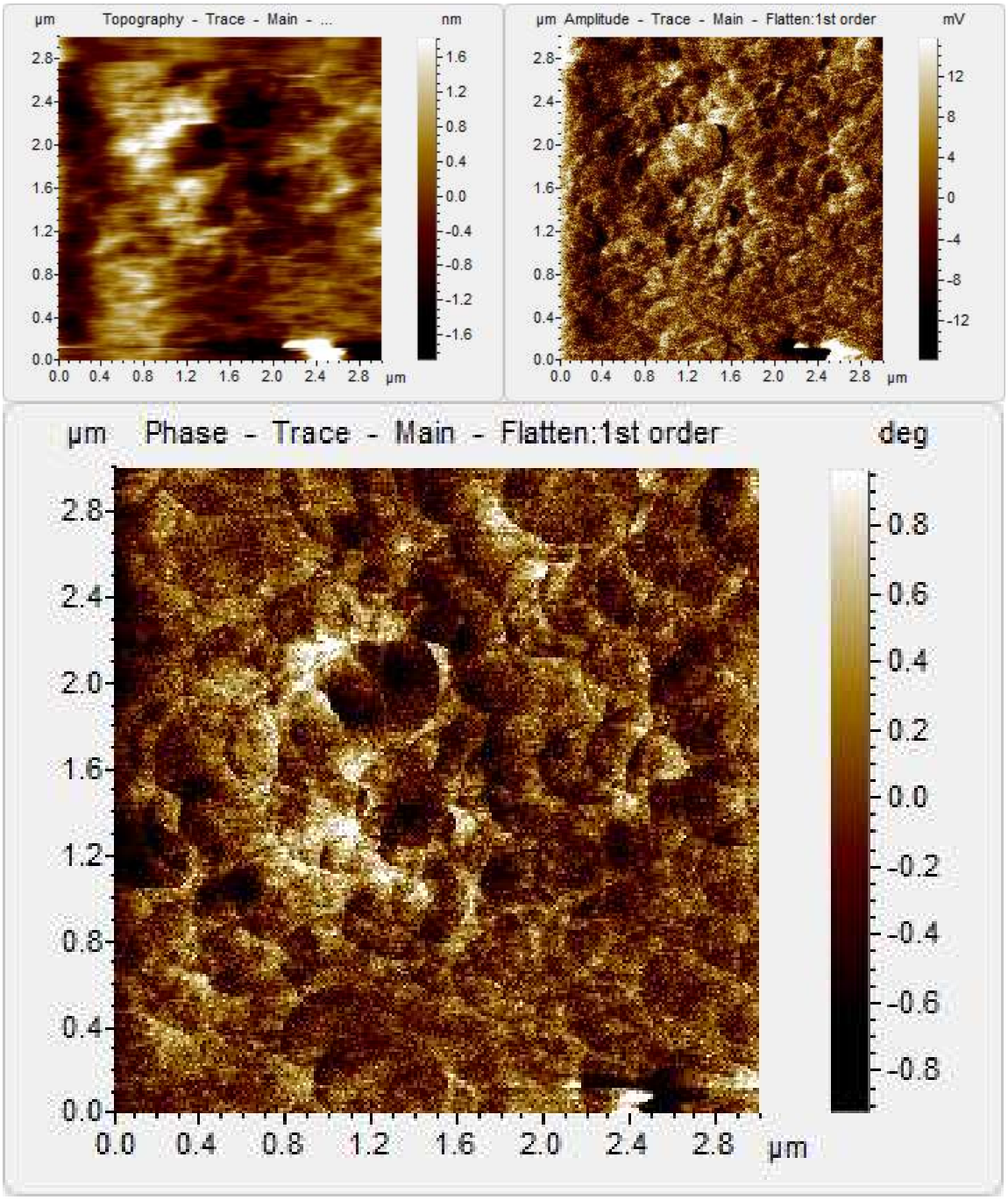

Figure 49: Alternative commercially-available, unaccelerated, non-thixotropic isophthalic unsaturated polyester – topography (top left), Amplitude (top right), and Phase (bottom) exposed to 15 minute ASTM B117 salt fog

As shown in Figure 49, the alternative resin also shows a series of overlapping spheres that strongly resembles Figure 45, p76. There is also some similarity to the closely packed structure seen in Figure 38, p72. Although this resin was not used throughout this work, there is some evidence of a closely packed microgel structure in two different commercially available unsaturated polyester resins without the destructive sample preparation methods used in other studies. The first order flatten function is a linear subtraction method used to level the sample and reveal features that might otherwise be obscured by a tilt of the surface.

5.3 DISCUSSION OF PHYSICAL CHANGES

During the curing of unsaturated polyester resins, phase separation is observed between the styrene and the polyester fractions [43]. In this case, phase separation refers to the way a uniform liquid blend of polyester and styrene monomer do not remain uniformly distributed in the cured polymer. Instead, the polyester forms microgels and the styrene forms bridges as well as covering the surface [43]. The extent of the phase separation depends on several factors including the molecular weight of the unsaturated polyester polymer and the cure temperature [154]. The phase separation in reactive systems may be induced by the resin composition during curing [61]. However, styrene is relatively non-polar in both its monomeric and polymeric forms. Crosslinking of the polar chain ends of the unsaturated polyester should decrease the degree of polarity, not increase it – causing phase separation. Increased molecular weight reduces the proportion of hydrophilic chain ends in the mixture [154]. In contrast, the styrene is hydrophobic in nature [154]. In general, increasing the molecular weight of the unsaturated polyester polymer increases the solubility in styrene and decreases the water absorption of the cured coating [154].It may be possible that the exothermic nature of the curing reaction leads to a temperature increase that facilitates the phase separation. Indeed, it has been reported that phase separation is dependent on the temperature during curing [62]. The nature and extent of the phase separation is key to the formation of the microstructure and therefore understanding the phase separation is essential for understanding polymer performance.

As previously discussed (Sections 2.1.2 and 2.1.4.1), unsaturated polyester resins are a blend of an unsaturated polyester (in this case polymerised from isophthalic acid, maleic anhydride and propylene glycol) in styrene monomer. As the cure progresses, the unsaturated polyester forms microgels, surrounding the more polar chain ends. The non-polar styrene monomer crosslinks with the polyester and also into polystyrene bridges and possibly at the surface (see Figure 38, p72). Polystyrene is more hydrophobic than unsaturated polyester due it its non-polar nature, and styrene is known to increase the hydrophobicity of the final resin once blended. However, it is not currently possible to correlate the unsaturated polyester hydrophobicity with the performance of the final coating due to the effect of curing with styrene. It is thought that the glassy nature of polystyrene together with the hindrance of the ester groups when cured in polystyrene reduce the hydrophilicity [155]. Indeed, the phase separation and microstructure see in the cured unsaturated polyester resin cannot occur in the unsaturated polyester alone. Thus, the microgel structure that folds the more hydrophilic chain ends towards the centre would not occur. These differences may account for the blended resin being far less hydrophilic than the cured unsaturated polyester polymer.

Even through pure polystyrene is relatively hydrophobic, water is still absorbed. Water absorption is related to the size, location, and availability of "holes" in the polymer [156]. These are not holes in the macroscopic sense, but only of a size to accommodate one or a few water molecules. The rate of water transport is governed by the affinity of the polymer to water at that site. When the water molecules permeate the coating, they fill the free volume and cause a plasticisation effect [157]. This plasticisation reduces the T_g in a similar way to annealing by allowing the polymer chains to rearrange. Water ingress to a commercial isophthalic, propylene glycol unsaturated polyester cured with MEKP is expected to be around 1%, resulting in a drop in the T_g of about 8K due to plasticisation [155].

After moving through the surface layer, the water is expected to migrate preferentially to the unsaturated polyester microgels where the unreacted chain ends and ester linkages are more hydrophilic (Figure 50). Water can cause a scission of the ester linkage [155], which in turn leads to additional chain ends and additional hydrophilicity. While there is evidence that some monomers and unreacted molecules may be washed away [158], the dominant effect of salt fog seen in this work is to swell the clusters of polyester nodules. This might explain the wide variety of size ranges visible as the permeation progresses and how these appear to increase over time.

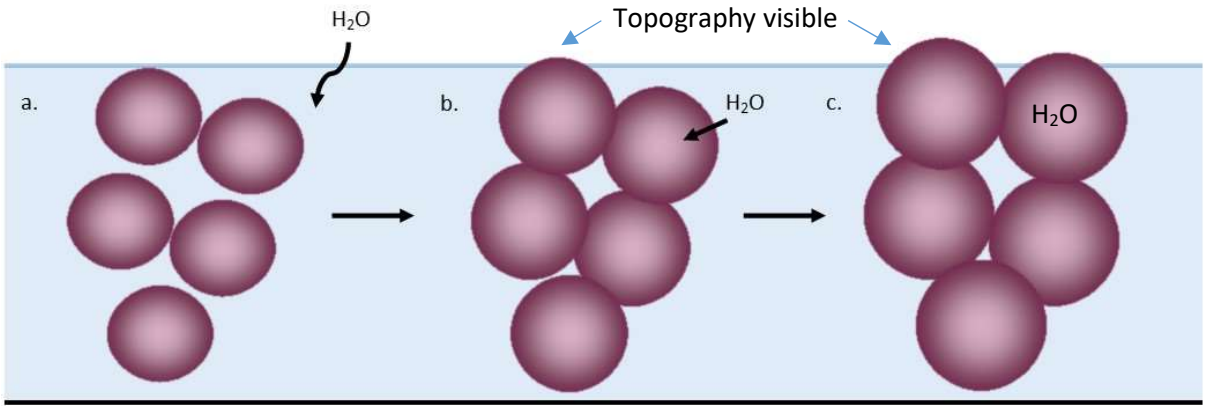

Figure 50: schematic of water absorption and subsequent swelling of the unsaturated polyester coating. ***(a)*** *the water penetrates the styrene surface and migrates towards the unsaturated polyester microgels,* ***(b)*** *attracted by the hydrophilic chain ends, the water is absorbed by the polyester microgels. Once inside, the water starts to swell the microgels,* ***(c)*** *hydrolysis of the ester bond increases the hydrophilicity of the polymer microgels. Additional water causes swelling that protrudes above the surface – rendering them visible to optical and AFM instrumentation.*

The salt fog (as with real-world exposure scenarios) are not solely water. ASTM B117 is a mixture of water and ions. Sodium chloride is purposely added to the water, but there may also be some ions present from the water source. De-ionised water is specified, and any residual ions are generally considered negligible to the artificial acceleration of the corrosion reaction. It is well established that certain ions such as Cl^- accelerate corrosion more than other ions [159].

Ions and water appear to mutually influence the way in which both move through the polymer coating. Ions cannot move without the presence of water, but their presence also seems to facilitate the passage of water through the coating by introducing polar character to a relatively non-polar polymer [160]. There is some discussion regarding the creation or pores or transport channels where water permeates more easily. Previous studies have found that localised water uptake creates permeant changes in the morphological structure, causing previously soaked samples to absorb more water when exposed to a humid environment or soaked again [161]. The hypothesised pores are on a scale too small to be seen directly by the techniques in this work. However, some of the theories are also discussed later with relation to thin films (Section 6.2.2).

There is some debate regarding the difference in permeability to liquid water or humidity [151] which may suggest that coatings are more permeable to water vapour due to the higher velocity of water vapour molecules or to the way the water molecules cluster in vapour form [162][163][164]. It is reported that liquid water and water vapor do no act the same way after absorption into the polymer film and at the interface. Differences in molecular placement and groupings can still be detected after absorption. Unfortunately, it remains unclear how these two forms differ in their effect on polymer degradation in the bulk or in the corrosion reaction at the interface. In practice, a salt fog (and real-world exposure) is a mixture of both liquid water and water vapour. Clarifying the differences between water vapour and liquid water is beyond the scope of this work, and as a clear understanding has eluded researchers thus far it may be a Herculean task to reach a clear understanding at this time.

5.4 Summary

Short term exposure to salt-fog has induced changes in the surface that are visible optically and detectable with the AFM. These features conform to the structures expected in an unsaturated polyester coating. The physical changes seen optically and by AFM methods were discussed.

Electrical properties at the surface of the sample were examined by Kelvin Probe AFM. The presence of surface potential features independent of the topographical features suggests differences in electrical properties may continue though the bulk of the polymer film. For the corrosion reaction to proceed, an electrolyte must reach the metal-coating interface. This transport mechanism is governed by electrical properties within the coating. In the next chapter electrical properties through the coating will be examined by CSAFM. Quantitative measurements will be attempted.

5.5 Supplemental Images

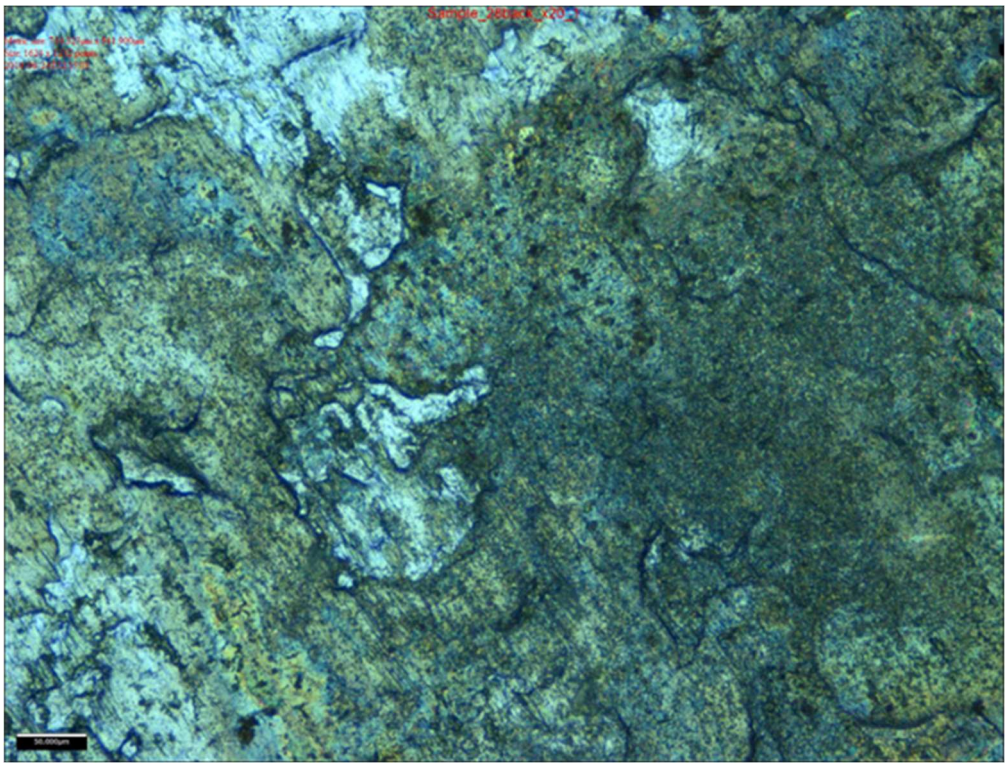

Figure 51: Uncoated steel, this sample has some surface rust and pitting, but the general grain and structure can be seen. A similar grain and structure can be seen below the polymer in Figure 35, D.

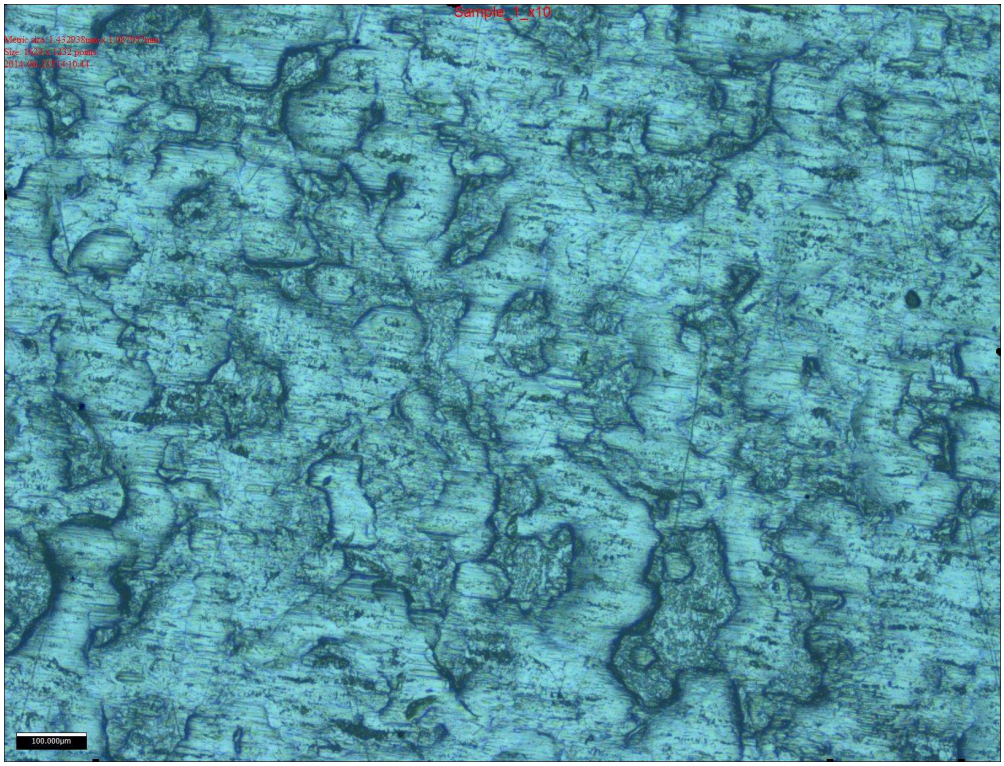

Figure 52: Alicona image of cured unexposed unsaturated polyester. The polymer is entirely transparent, and all features are of the steel substrate below. Uncoated steel can be seen in Figure 51, p85.

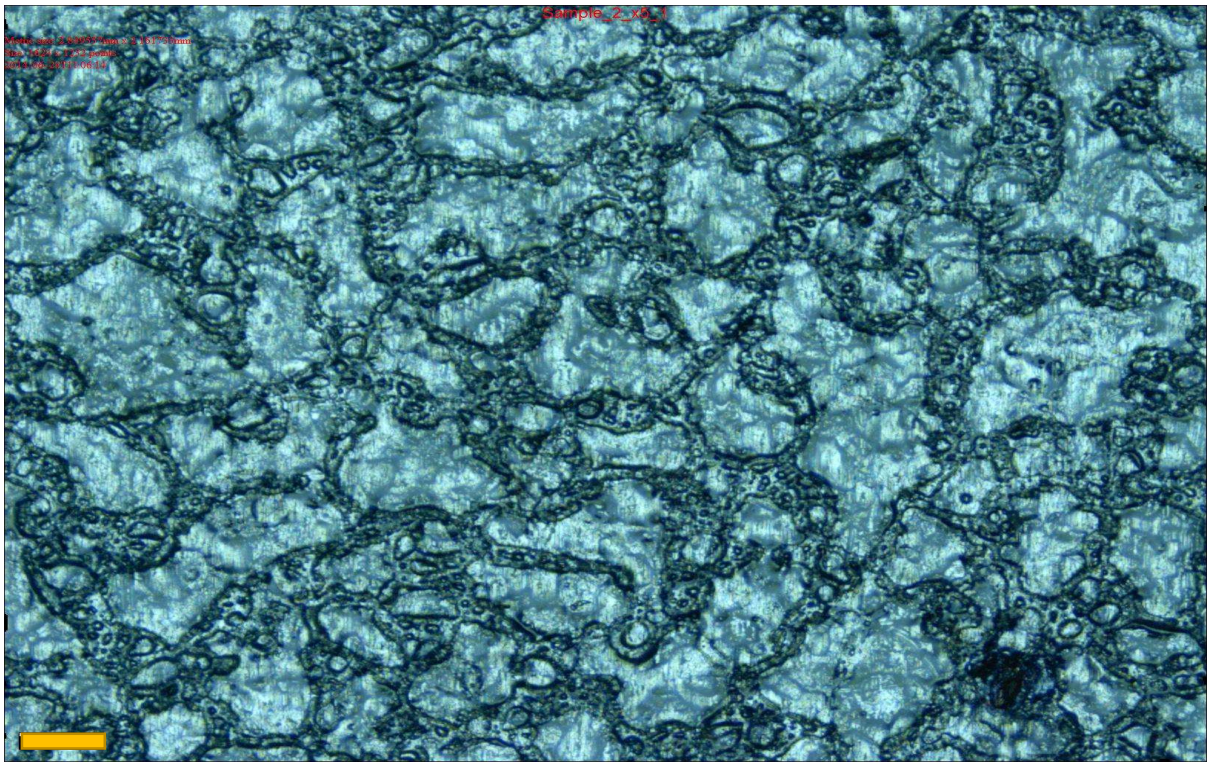

Figure 53: Alicona image of cured unsaturated polyester after 15 minutes of ASTM B117.

200 µm

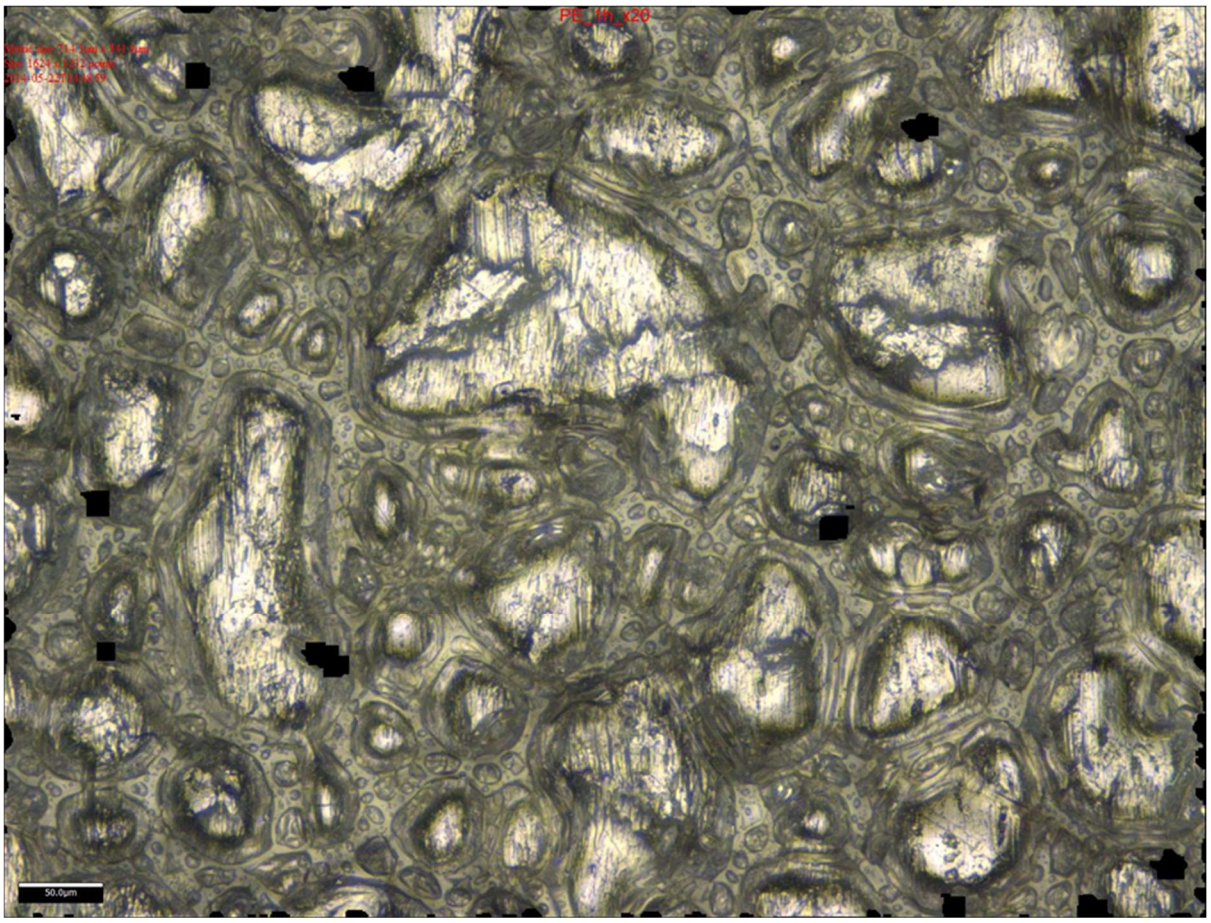

Figure 54: 2D Image of Figure 40

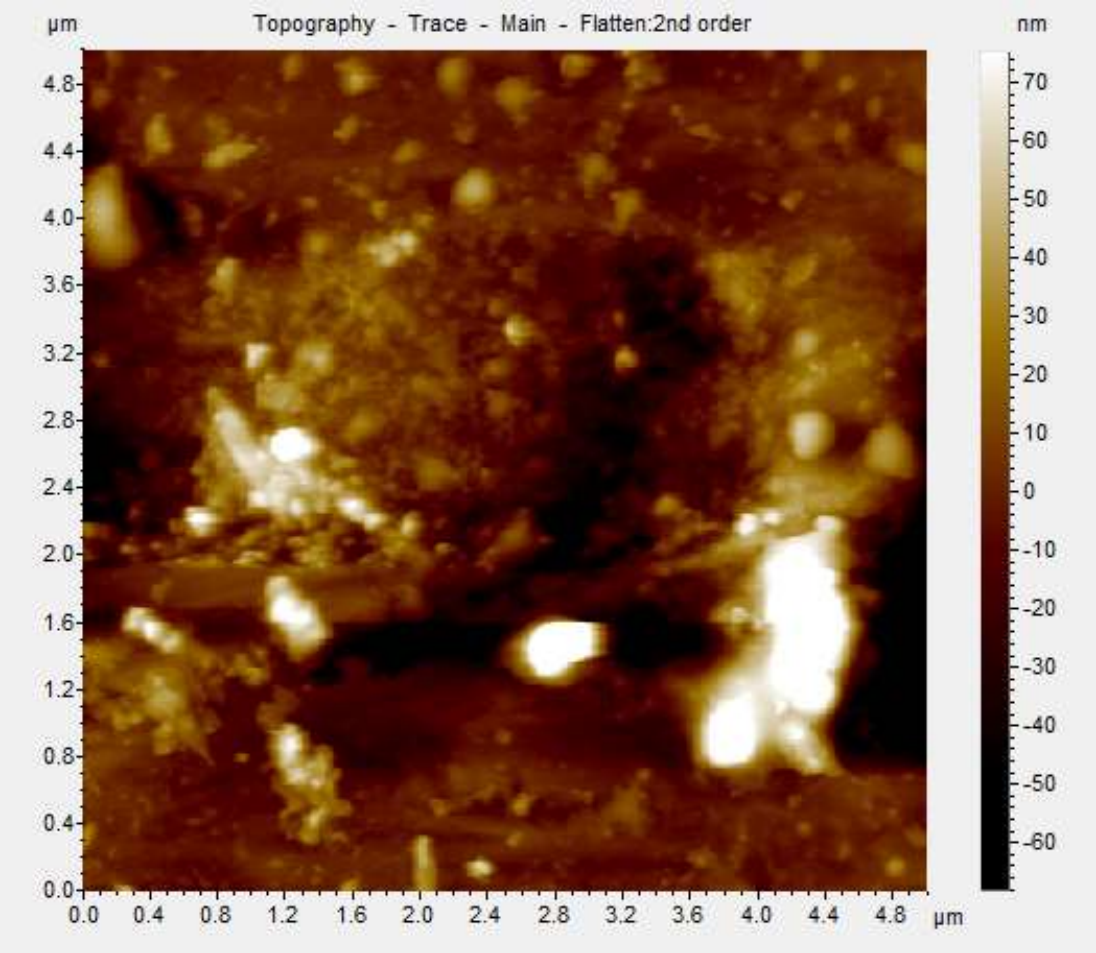

Figure 55: uncoated steel samples by tapping mode AFM. Topography indicates a profile under 100 nm.

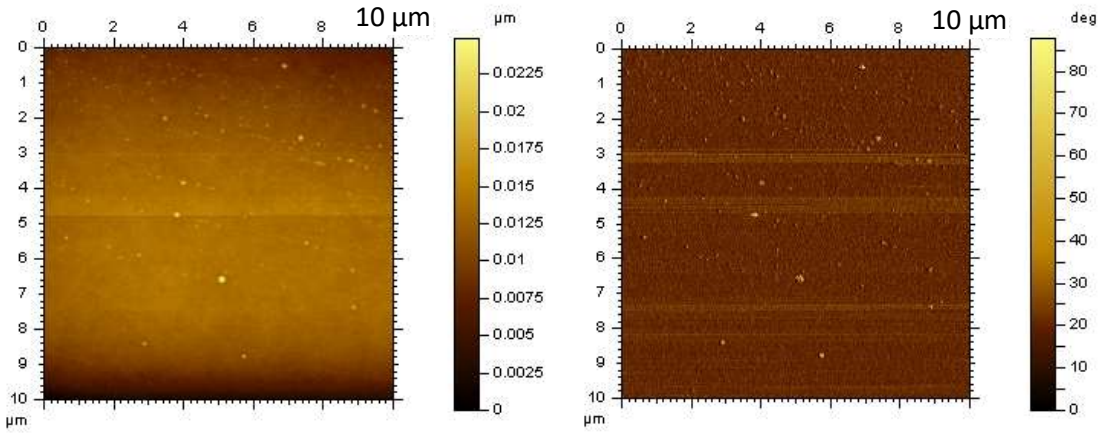

Figure 56: Non-thixotropic isophthalic unsaturated polyester cured with 1% MEKP, unexposed – tapping mode AFM topography (left) and phase (right) the non-thixotropic isophthalic unsaturated polyester show a generally smooth and uniform surface. In contrast to the optical image, the steel substrate is not visible in the AFM scans.

6 Further Results and Discussion – Electrical properties by Current Sensing Atomic Force Microscopy

The previous chapter confirmed the presence of microstructures in the 15µm thick samples of cured unsaturated polyester coating. These microstructures conform to the expected arrangement in published literature of spherical globules of unsaturated polyester polymer connected by branches of polystyrene. KPFM was able to differentiate the surface potentials of these structures (Section 5.2.2).

While the confirmation of microstructures without fracturing and dissolving part of the sample is an improvement over previous methods, this work aims to relate the electrical properties to these microstructures to facilitate further work in anticipating the onset of localised corrosion. The electrochemical nature of the corrosion reaction means that the ability for current to flow through the coating is of great interest. Using the AFM tip and the steel substrate as electrodes, the current through a sample may be precisely mapped by Current Sensing Atomic Force Microscopy (CSAFM).

6.1 15 µM thickness, 15 minutes of DI water immersion

Resistance is dependent on the path length, in this case through the coating. Therefore, it is essential to minimise the variation in thickness. In Chapter 5, salt fog was used to reveal the microstructures, but it also caused topographical changes as the water was absorbed. A 15 µm thick, unexposed sample of cured unsaturated polyester resin was scanned, without notable features. A typical scan has been added to the appendix of this section (Figure 79, p112).

6.1.1 CSAFM

In an attempt to expose a feature without causing significant topographical changes shown after exposure to ASTM B117 salt fog, a large drop of deionised water was applied to the surface of the 15 µm thick sample for 15 minutes at room temperature. After this treatment, water was absorbed from the surface using paper towel and CSAFM was performed. The differences in topographical changes between a mixture of liquid water, ions, and water vapour in a salt fog and exposure to liquid deionised water alone might be of interest to future researchers in the context of the effects of humidity vs liquid water discussed in Section 5.3, but will not be discussed further here.

Using a sample bias voltage of 0V, a baseline image was scanned. Based on Ohm's law, this should not produce any current and the response may be attributed to topographical and frictional information being picked up across multiple channels. The maximum current found was 2 pA, at location A (Figure 57). Despite the image scale only reaching 4 nm, the AFM measured topographical value of -44 nm at this location. This should be considered a minimum value as deep craters with a narrow opening can cause an error due to the inability of the probe to scan accurately down the sides of the crater to measure the true depth or due to the maximum movement of the probe on the z-axis. A long, sharp probe tip can reduce this error to some extent, but physical limitations will always exist. Wide, sloping features are less prone to this error. A different location in the bulk (B) with a topographical value of 0.1 nm had a current of 0.1 pA (Figure 57, also Figure 81, p113). This scan was also performed at two positive sample bias voltages and summarised in Table 7.

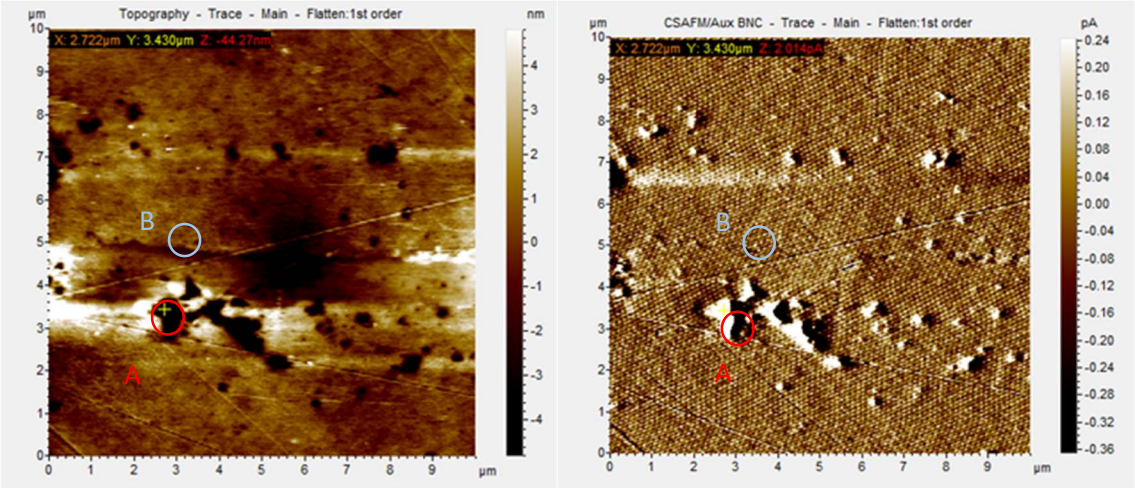

Figure 57: AFM images of cured unsaturated polyester resin exposed to 15 minutes of deionised water immersion. 0V sample bias. At the point indicated, -44nm and 2 pA, as measured by the AFM. (Scan with measurement at point B indicated in Figure 81, p113)

Table 7: Summary of current response obtained at two estimated film thicknesses and three sample biases

Figures	Sample bias voltage	Current	Measured Topography
Figure 57, A	0 V	2 pA	-44 nm
Figure 57, B (also Figure 81, p113)	0 V	0.1 pA	0.1 nm
Figure 58, A	0.2 V	2 pA	-26 nm
Figure 58, B (also Figure 82p114)	0.2 V	0.03 pA	0.20 nm
Figure 59, A	3 V	2 pA	-40 nm
Figure 59, B (also Figure 83, p115)	3 V	0.03 pA	0.2 nm

At first glance the data in Table 7 are not encouraging. The current was found to be 2 pA at point A with a sample bias voltage of 0 V as well as 0.2 V and 3 V. The measurements at increased voltage do not show current in excess of the baseline measurement of 2 pA. However, the measurements may still be interesting.

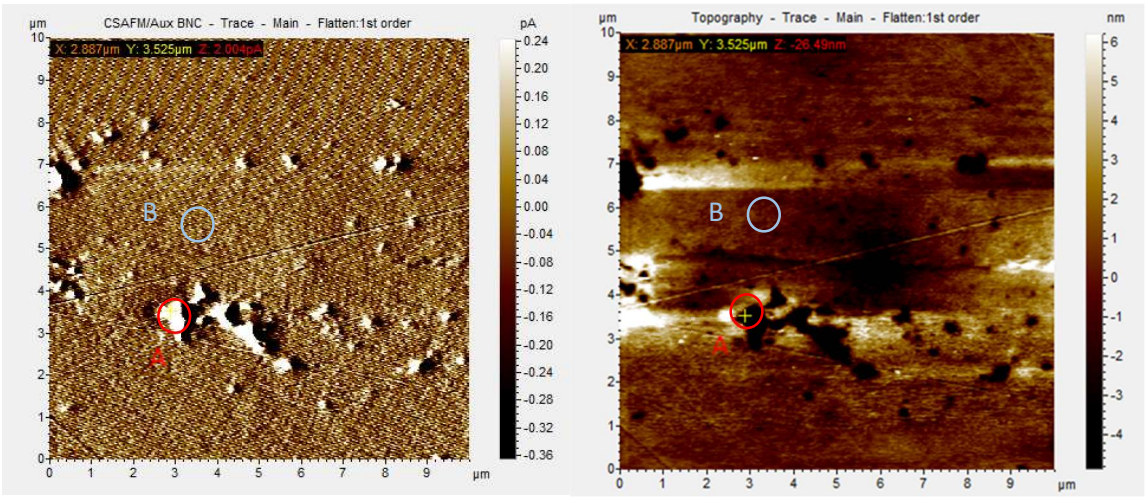

Figure 58: 0.2V sample bias voltage

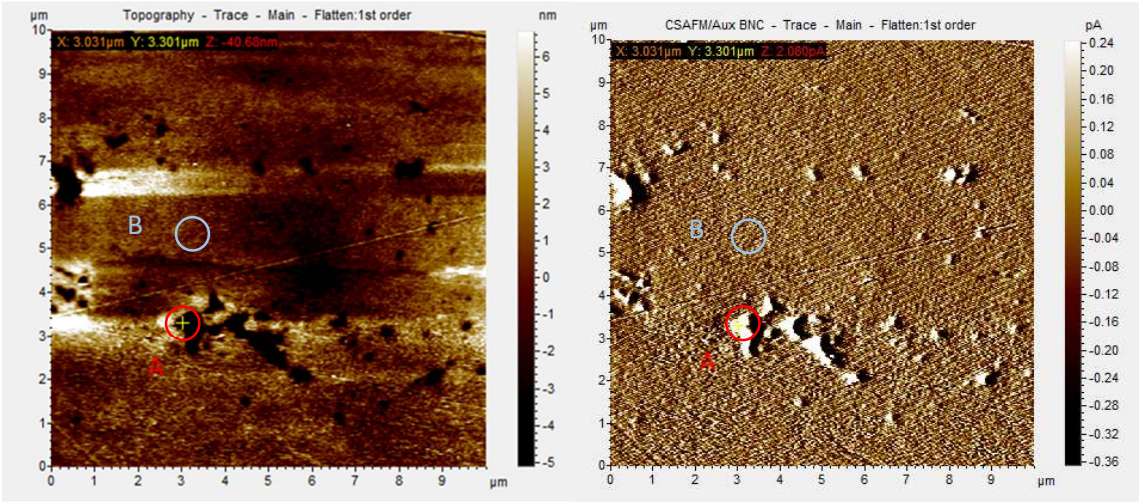

Figure 59: 3V sample bias voltage

Looking at location A vs location B on this sample, the sample is at least 26 to 44 nm thinner at location A is than location B – around 0.3% of the total thickness. It is no surprise that the thinner coating allows more current to pass through. However, the difference in resistance can be shown to be far greater than would be expected from reduced thickness alone. Other factors will also come into play, including the increase in contact area due to topographical valleys in the surface.

Voltage (*V*), resistance (*R*), and current (*I*) are related by Ohm's law (Eqn. 4). In CSAFM mode the Voltage (sample bias voltage) is set and the current is measured. The resistance can be calculated

from the other two parameters. However, the resistance is dependent on the sample geometry. To compare materials using different geometries, resistivity (ρ) is used; the relationship between resistance and resistivity is given in Eqn. 5. In order to calculate resistivity from resistance, we will need to know the length and the area of the sample. In this case the path length for electrical resistance is the thickness of the sample – either 5 µm (location B) or the reduced thickness (location A).

Determining the area (A, Eqn. 5) is somewhat more complicated as it requires estimating the area in which the AFM tip in contact with the sample. Although several methods can be used, all are estimates and have strengths and weaknesses. In this work, a relatively simple estimation is used which assumes a purely elastic contact [165]. Polymers are by nature relatively elastic and AFM uses small forces and short times which suggest an elastic contact is a reasonable assumption. The method of calculating the area of contact is described below.

The radius of the contact zone of AFM probe in contact with surface (α) [165] can be expressed using Hertzian contact mechanics (assuming a purely elastic contact):

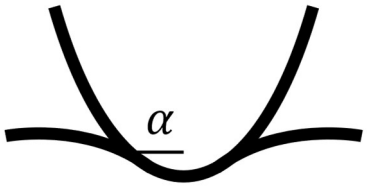

Figure 60: Schematic of the contact area () from Eqn 1. In this model, depth is taken into account using Young's modulus and force and the radius is used to calculate the area using $\pi\alpha^2$.

$$\alpha = \left(\frac{3\,FR_t}{4\,E}\right)^{1/3} \quad \ldots\ldots(1)$$

Where, loading, in this case imaging force, F, in [nN] can be determined using

$$F = k * DS * f \quad \ldots\ldots(2)$$

We can also replace the Young's modulus (E) of each contacting body (metal AFM tip and polymer sample) by the 'reduced' value

$$\frac{1}{E^*} = \frac{1-v_1^2}{E_1} + \frac{1-v_2^2}{E_2} \quad \ldots\ldots(3)$$

And

k = lever spring constant (typical 0.3 N m^{-1} as given by AFM probe specification);

DS = Deflection sensitivity determined from FD curves (see Figure 80, Annex, p112); 148.4 nm V^{-1}

f = set point or the force in V used to image surfaces 0.119 V;

R_t = tip radius (AFM probe) (<30 nm, >>8 nm – taken to be around 20 nm);

E^* = the reduced modulus of tip and substrate (E_1: Pt = 163 GPa [166], E_2: polymer 3.6 GPa[4]);

v = Poisson's ratio of tip and sample (v_1: Pt = 0.39 [166], v_2: polymer 0.4 typical [167]).

*When all terms are put into Eqn. 1, the radius of the tip contact area (α, Eqn. 1) is 2.6 nm and the area of contact between the AFM probe and the polymer surface is **21 nm²**.*

Then, using the definition of resistance:

$$R = \frac{V}{I} \qquad \ldots\ldots (4)$$

as well as the equation for volume resistivity (ρ) [168].

The expression for volume resistivity is:

$$\rho = R\frac{A}{l} \qquad \ldots\ldots (5)$$

where,

ρ = resistivity;

R = resistance;

A = area;

l = path length (in this case, the coating thickness).

The area is assumed to be constant, though in practice it cannot be due to the way slight topographical valleys can increase the contact area between the probe and the surface. The actual difference is expected to be fractions of a nanometer and the effect on the resistance value would therefore be much less than the measured difference. The path length is also not constant across the surface. To compensate for this, two points (single path lengths) were chosen to compare. The resistivity is independent of thickness and thus should be a property of the material (polymer sample). The precise thickness of the coating at this location is not known and therefore an approximate value of 10 µm is used. Table 8 and Table 9 show that the resistivity is significantly lower at location A than location B. There may be some slight variation in the area of contact between the tip and the sample that cannot be accounted for. However, the reduction in path length (sample thickness) is taken into account during the calculation and therefore the

[4] From supplier TDS

resistivities should be similar, unless there are significant differences in the sample material at that point. It is hypothesised that the differences could be evidence of polymer microstructures. However, resistivity could also be affected by moisture present in the sample, ions, or impurities unrelated to the microstructure.

Table 8: Calculated resistance values at point B (bulk) and A (feature). Voltage 3 V, current 0.03 pA and 2 pA (Table 7), area 21 nm^2 (calculated above), length as indicated in the table for an approximate value of 10 µm for B and 42 nm less at point A.

3 V	**Point B (bulk)**	**Point A (feature)**
Thickness	10 µm	9.96 µm
Resistivity (Ω m)	210 Ω m	3.1 Ω m

Table 9: Calculated resistance values at point B (bulk) and A (feature). Voltage 0.2 V, current 0.03 pA, and 2 pA (Table 7), area 21 nm2 (calculated above), length as indicated in the table for an approximate value of 10 µm for B and 26 nm less at point A.

0.2 V	**Point B (bulk)**	**Point A (feature)**
Thickness	10 µm	9.97 µm
Resistivity (Ω m)	14 Ω m	0.2 Ω m

Unfortunately, as these values are not significantly different from the baseline, firm conclusions cannot be drawn. However, it is interesting that the resistivity at the two locations varies by a factor of 100 over repeated measurements and multiple voltages. Despite being referred to as a "law" many materials do not obey Ohm's Law [169]. Current does not always increase linearly with applied voltage, and some materials will only obey Ohm's Law over a certain voltage range. From a molecular perspective, application of a voltage causes electrons to move (on average, after collisions) in a particular direction [169]. Metals and other conductors are expected to have a relatively uniform resistance throughout the structure. Semi-conductors, like polymers, have a more complicated structure that means electrons will encounter areas of higher and lower resistance as they travel through the sample. The aromatic nature of polystyrene compared with the primarily aliphatic unsaturated polyester, contrasted with residual free-radicals, unreacted monomers, and absorbed water and ions makes this a far more complex system for conductivity and resistance. Even if samples do not follow Ohm's Law, the electrical properties may still be of interest for the corrosion reaction. Breakdown voltage is discussed in more detail further in Section 6.4.2.

Despite a longstanding rule of thumb that increased electrical resistance improves corrosion performance, there is no understanding or agreement as to how much resistance is desirable or required. Indeed, the rule of thumb on the importance of electrical resistance has been challenged in the USA by Polyguard, after a number of significant failures due to electrical

shielding of a disbonded coating opened an opportunity for a different commercial approach. Similar failures were not prevalent in the EU due less common use of affected materials. Measurements of the bulk polymer with an ohmmeter (Amprobe 30XR-A) gives a resistivity of around 40 Ωm. This is in line with AFM measurements at 3 V. It's unclear what voltage is used by the ohmmeter, and the resistance (and therefore resistivity) of unsaturated polyester has been shown to vary with voltage nonlinearly.

6.1.2 Summary

CSAFM has detected a feature with electrical resistivity properties that may be different from the bulk polymer. This type of inhomogeneity is likely the result of bonding within the polymer coating. Uniform thickness is essential for calculating the resistivity. Ideally, the resistance through the coating could be mapped, and the structures identified simultaneously. Polymers are known to have high electrical resistance and seem to exceed the limits of the AFM at this thickness. It is thought that thinner coatings will bring the current into a range for better detection. Samples with reduced thickness will be examined in the next section, 6.2.

6.2 Thin Films (5 µm)

6.2.1 CSAFM

Following the somewhat successful detection of electrical features of a cured unsaturated polyester coating by CSAFM, it was reasoned that thinner samples would increase the current through the coating – bringing it into a more easily detectable range. Thus, samples were prepared by applying coating onto highly polished steel and manually reducing the thickness by way of a 5 µm spacing shim and a microscope coverglass (see Section 4.4.2). Once the samples were cured, the coverglass was removed and the samples analysed by CSAFM.

In the previous section, resistivity of the polymer was calculated to be around 0.2-14 Ωm at low voltage and 3-210 Ωm at 3V. If the thickness of the new samples is 5 µm, and a similar voltage is used, the current should be between 0.06 and 4 pA. The AFM nose sensitivity is 0.1 nA V^{-1}, so unfortunately this would not fit well with the expected detectability, though slightly higher than the previous section.

In the same way as described in section 6.1, a baseline was measured at 0 V (and therefore 0 current). Additional current measured after applying a voltage to the sample would enable the resistance to be mapped. The differences seen in the map could correlate to microstructures in

the bulk of the sample, and theoretically could be evidence of areas more susceptible to allowing the passage of reactants (water, oxygen, and ions) and ultimately the corrosion reaction.

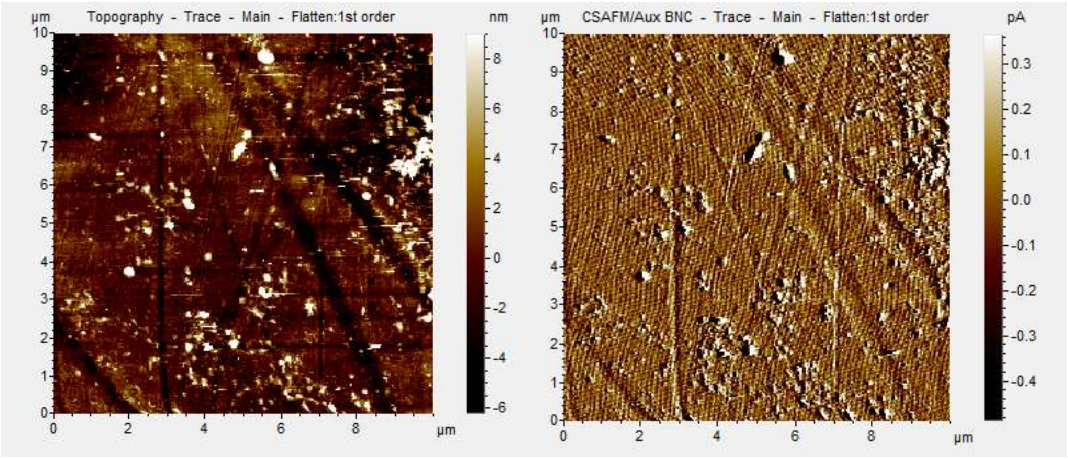

Figure 61: Baseline scan of 5 µm thick samples of cured unsaturated polyester coating on polished steel surface, sample bias voltage of 0 V , Topography (left) and CSAFM current (right)

To confirm the baseline response, a 10 µm area was scanned with a sample bias voltage set at 0 V (Figure 61). Based on the definition of resistance, this should not produce any current and the response can be attributed to topographical information being picked up across multiple channels. Baseline current measurement is taken to be - 0.4 to 0.3 pA.

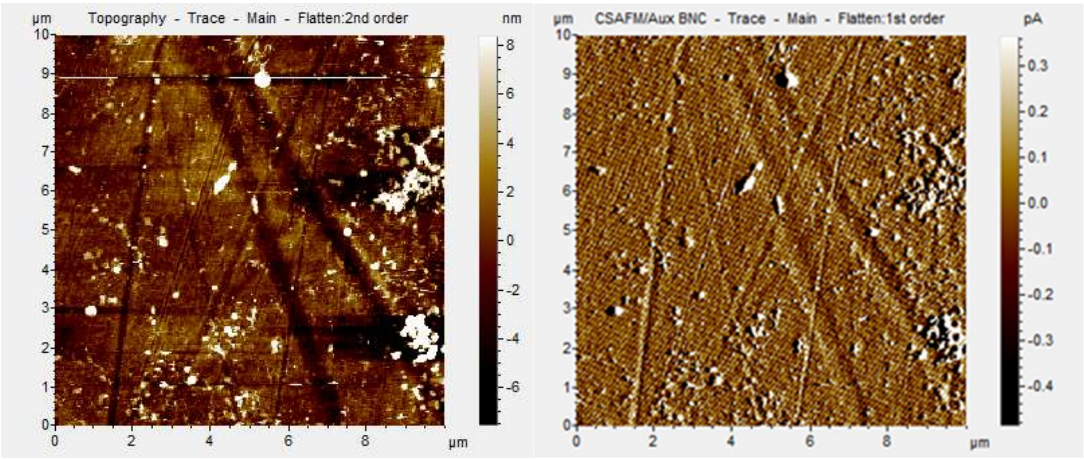

Figure 62: Scan of 5 µm thick samples of cured unsaturated polyester coating on polished steel surface, sample bias voltage of -5 V – same area as Figure 61 but with higher sample bias voltage, no visible change in current response, Topography (left) and CSAFM current (right)

The same area as Figure 61 was imaged with a sample bias voltage of -5 V (Figure 62). If, as expected, the current was flowing through the sample we would expect a current greater than the baseline. The image is almost exactly the same, with a current range of -0.4 to 0.3 pA. As this

was also shown in the baseline scan, it can be inferred that no additional current was produced by the sample bias voltage.

The same area as Figure 61 and Figure 62 was imaged with a sample bias voltage of -7.5 V (Figure 63). Unfortunately, again the measurement does not detect any current in excess of the baseline from Figure 61.

Finally, the same area was imaged with a sample bias voltage of -10 V (Figure 64). This is the maximum voltage achievable by the instrument. However, as seen in the previous images, the current does not vary from the baseline current visible in Figure 61. Thus, 10 V did not produce an additional current response in these 5 µm samples.

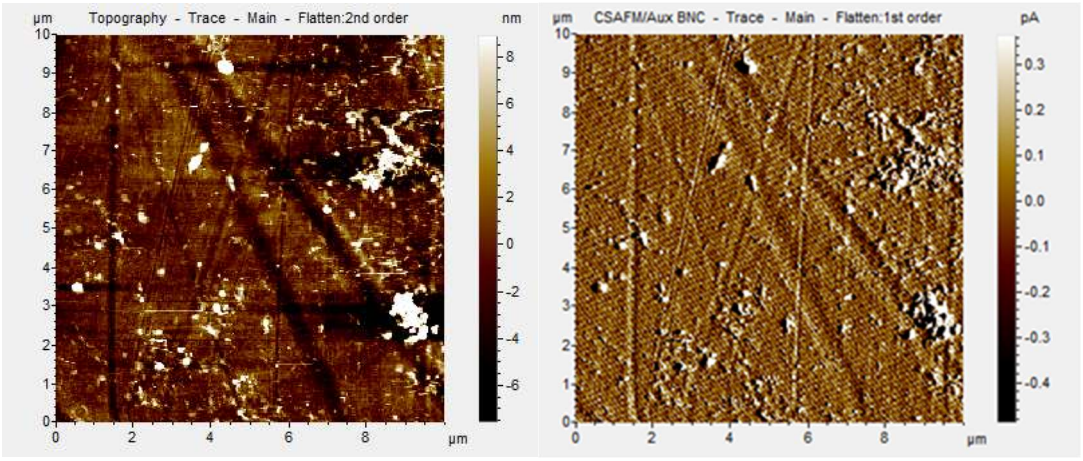

Figure 63: Scan of 5 µm thick samples of cured unsaturated polyester coating on polished steel surface, sample bias -7.5 V – same area as Figure 61 but with higher sample bias voltage, no visible change in current response, Topography (left) and CSAFM current (right)

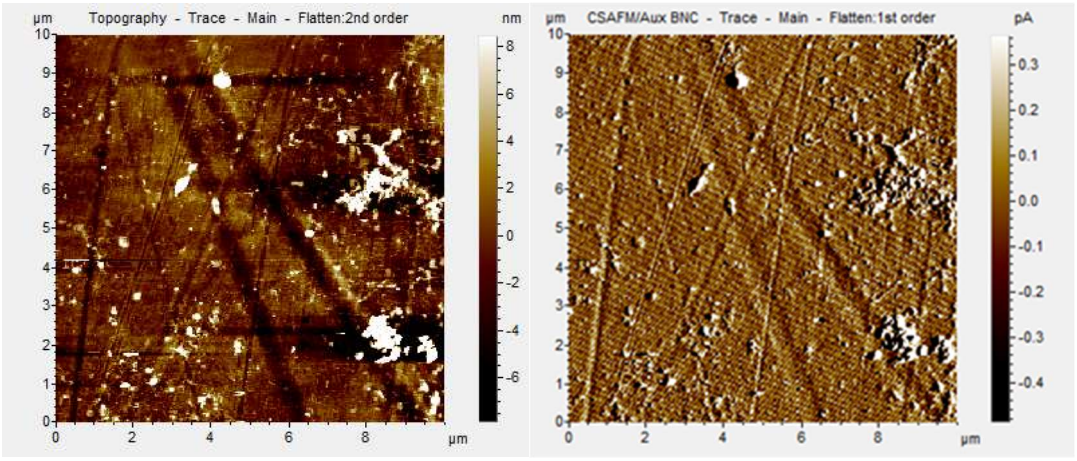

Figure 64: Scan of 5 µm thick samples of cured unsaturated polyester coating on polished steel surface, sample bias -10 V – same area as Figure 61 but with higher sample bias voltage, no visible change in current response at maximum voltage capable by Agilent AFM 5500, Topography (left) and CSAFM current (right)

6.2.1.1 *Summary*

Unexposed 5 µm thick samples of unsaturated polyester coating do not show a CSAFM response beyond the baseline as the bias voltage is increased. The results indicate that this unsaturated polyester resin does not follow Ohm's law within the voltage range achievable with current instrumentation and sample geometry. It is unclear if alternative test criteria would significantly change the result. A discussion of some theories of ion migration and conductivity in polymers follows.

6.2.2 Mechanisms of ion migration

As mentioned previously in Sections 2.4.1 and 5.3, one theory of the breakdown of corrosion prevention by organic coatings postulates that the exposure to water forms pores in the coating. These pores then remain after drying and allow for water and ions to penetrate more easily after repeated wet/dry cycles. An alternate theory suggests that the ions move through the bulk of the coating facilitated by areas of localised ionic character.

Both the Alicona and AFM (Chapter 5) do show irreversible changes to the topography of the samples when exposed to a salt fog. However, the expected size of pore-like structures is not clear from literature. However, pores just large enough to accommodate a few water molecules and ions would be significantly less than 1 nm in diameter and may not be obvious at the surface. Figure 65 shows a small scan of unsaturated polyester coating sample after exposure to 30 minutes of ASTM B117 salt fog. Small features are visible in the scan, but it is unclear if these are evidence of pores, or simply clusters of polyester microgels. Strong difference in the phase scan suggest these are more likely to be microgels.

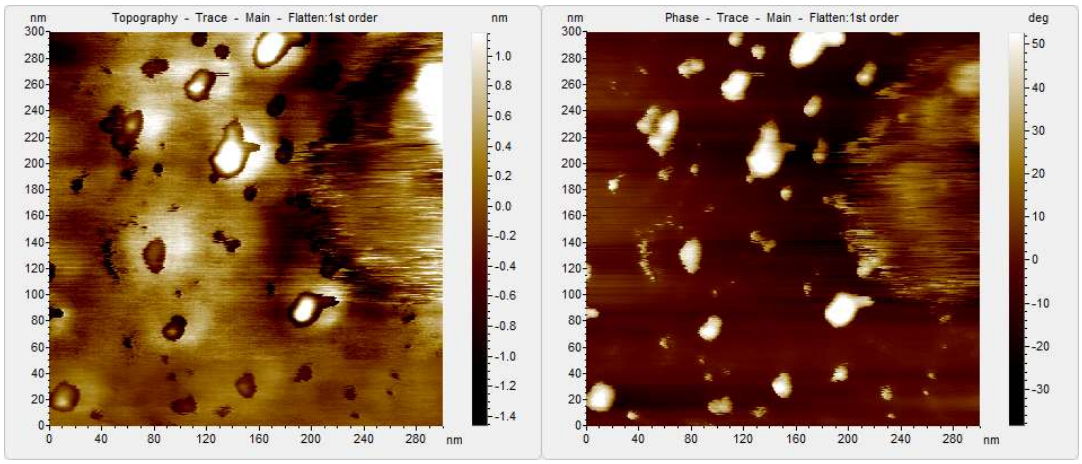

Figure 65: Tapping mode AFM scan of ~15 µm thick cured unsaturated polyester coating after 30 minutes salt fog exposure. Small dips in the surface of the coating might be evidence of pores formed, but also could be attributed to polyester microgel. Agilent AFM 5500 AC tapping mode.

Figure 66 shows a CSAFM scan on a similar scale to Figure 65. While the tapping mode AFM scan shows some features revealed by the exposure to salt fog, the CSAFM does not show any features at all. Unfortunately, attempts to link the features (whether pores or microgels) were unsuccessful.

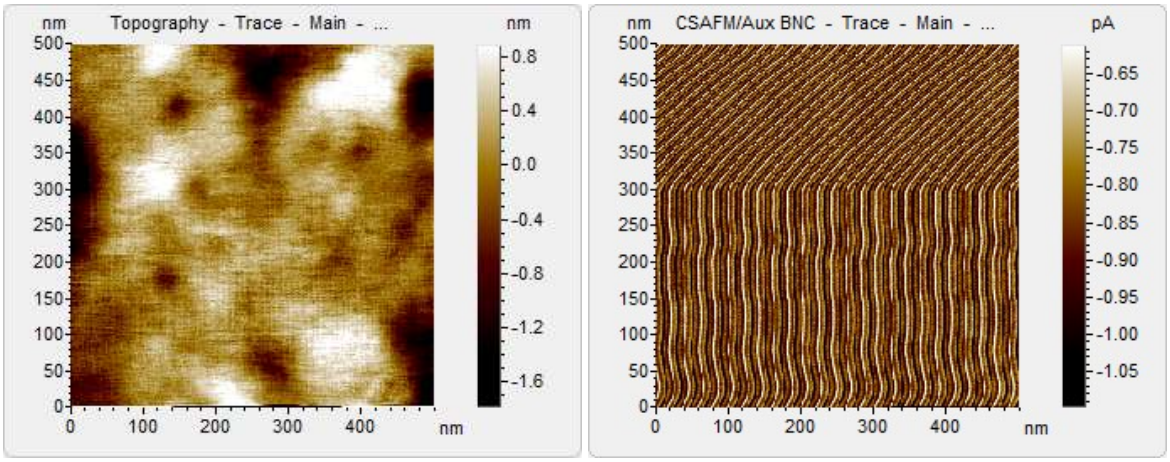

Figure 66: CSAFM scan of ~5 µm thick sample of cured unsaturated polyester coating after 15 minutes of ASTM B117 salt fog exposure, Agilent AFM 5500, tip bias voltage of 5V. No features can be attributed to pores or polyester microgels.

6.3 Validation using VHS tape

Given the lack of expected response, the equipment manufacturer was contacted for advice on validating the machine and procedure (now Keysight Technologies for the Agilent AFM5500). It was recommended to use standard VHS tape (Figure 67) to validate as the conductive particles encapsulated in the tape should be discernibly different from the polymer film substrate.

Figure 67: typical VHS tape cartridge

VHS tape is constructed in three layers [170]. The substrate is a polyester film backing for stability. The top layer is a made of tiny particles of metal oxide (iron oxides or chrome dioxide) which magnetise to record the information. These two layers are joined by a layer of adhesive. During a CSAFM scan, more current passes through the conductive metal than the surrounding binder and substrate, so the particles can be detected.

A small portion of VHS tape was mounted to a steel panel using conductive glue to ensure electrical contact with the substrate electrode.

6.3.1 CSAFM

An area of the VHS tape was imaged with and sample bias voltage of 0 V, to establish the baseline (Figure 68, top – left and right). The CSAFM scan does pick up some current independently of the topography, this is considered the baseline value. The same area was then scanned with a sample bias of 1 V (Figure 68, bottom – left and right). With a sample bias voltage of 1 V, the current increases to around 20 pA. This is a difference of around 18 pA. Although it was not clear what magnitude would be expected, Keysight Technologies indicated that particles should be clearly discernible.

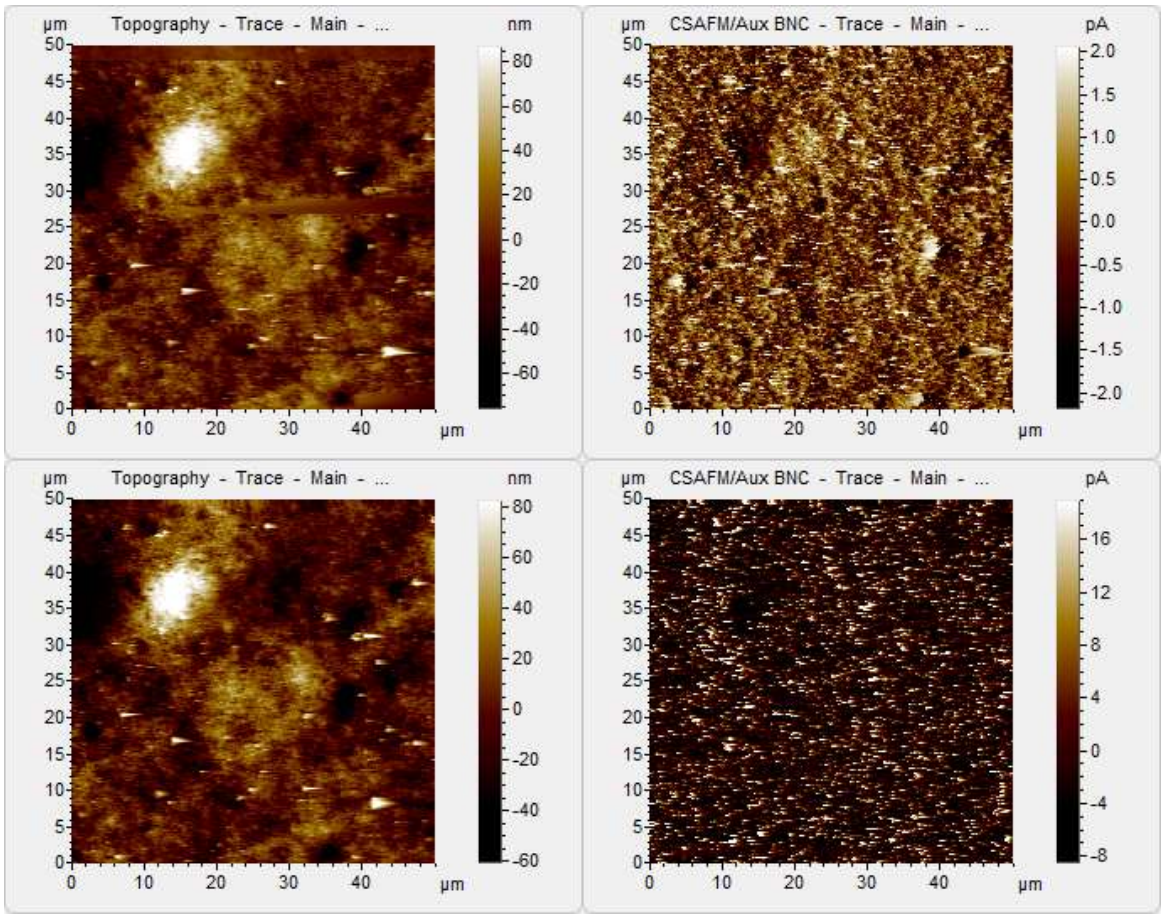

Figure 68: CSAFM scans of VHS tape. Topography (Left, top and bottom), CSAFM (Right, top and bottom), sample bias 0 V (top, left and right); sample bias voltage of 1 V, (bottom, left and right). Increasing the sample bias voltage from 0 V to 1 V, the peak current increases from around 2 pA to around 20 pA.

In a smaller scale image of the VHS tape, Figure 69 shows that a sample bias voltage of only 0.4V produces a current of 2.8 pA, independent of any topographical features. In these scans, maximum current is expected to correspond to locations of metal oxides in the VHS tape.

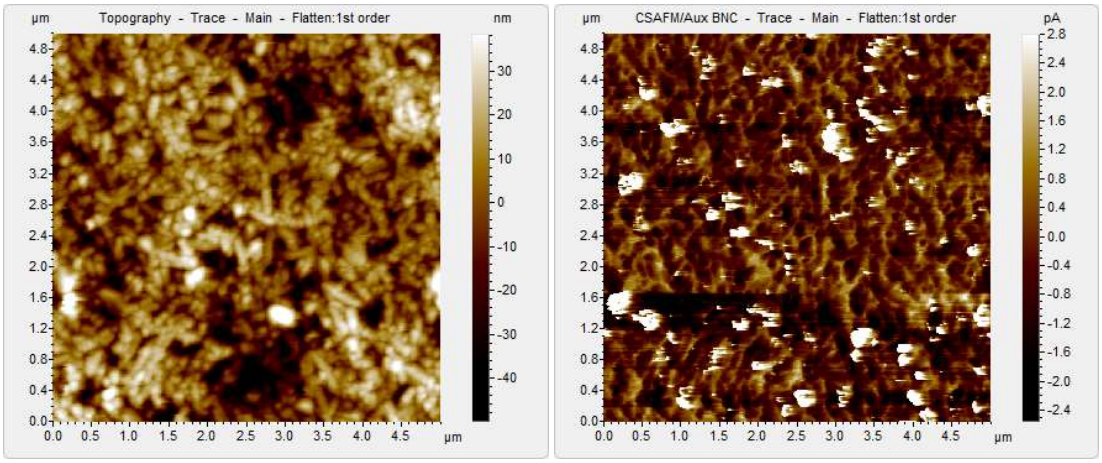

Figure 69: CSAFM scans of VHS tape. Topography (Left), CSAFM (Right), sample bias voltage of 0.4 V. Areas of higher conductivity are white in the CSAFM scan, and do not correspond with any topographical features in the topography scan.

There is significant variation among maximum current of VHS samples at the same voltage. It is clear that at lower sample bias voltage the current results are lower and appear to be more reproducible (Figure 70). The images of VHS samples were easier to obtain at low sample bias voltage. In general, large scan sizes tended to have larger maximum current. This may be due to the increased probability of a high current location in a larger scan. Although, all of the conductive areas appear as bright spots near the maximum in all images – the conductive features do not appear to have varying resistances within the detectable range. The VHS sample appears to obey Ohm's Law at low voltages, but more data points would be required to make a clearer determination on the actual relationship. Microscopically, the conductive particles fabricated into VHS tape seem to make a consistent path through the sample. Regions of higher and lower conductivity are expected due to the nature of the VHS tape (conductive particles in a less conductive polymer matrix).

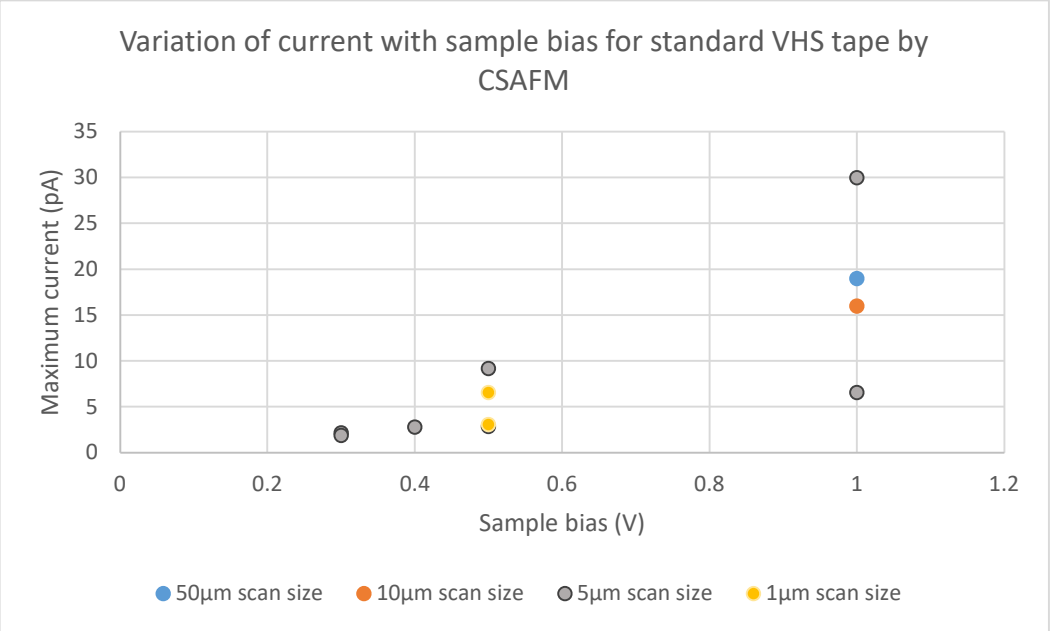

Figure 70: variation of current with sample bias voltage for standard VHS tape by CSAFM. For validation purposes, maximum current is measured at a feature, where the conductive path is strongest.

6.3.2 Summary

The CSAFM setup and method was experimentally validated with VHS tape, as recommended by Keysight technologies. The lack of CSAFM response in unsaturated polyester samples is not due to equipment or method.

6.4 Barriers to Conductivity

It is clear that samples of VHS tape do produce a CSAFM response, as expected, and that the samples of unsaturated polyester resin do not. However, it is not clear why. Some theories of conductivities in polymers are discussed.

6.4.1 Tunnelling distances and Activation Energy

Recent work on quantum tunnelling suggests that electrons could tunnel approximately 1-10 nm to reach a suitably conductive location [171]. Unsaturated polyester coatings and their microstructures of interest will always be too thick for the electron to tunnel directly through them. However, a concentration of water and ions is always present, and tends to increase with aging. It is postulated here that there is a critical point at which there are sufficient ions to complete a conductive path through the coating. Prior to this point, the volume between electrically active sites is too far for the electrons to jump and no conductivity is detectable.

Warfield and Petree noted in 1961 that physical processes are governed by the same concepts as chemical kinetic processes, and applied this to electrical conductivity of polymers [172]. They postulated that the electrical resistivity dependence on temperature is governed by the chemical kinetics of ion generation with a minimum activation energy and three ion sources. The majority of ions are residual monomers and other unreacted impurities that can easily move within the polymer network when an electrical potential is applied. Additional ions are formed by thermal dissociation and background radiation. In general, highly crosslinked polymers (like polyester and, to a lesser extent, polystyrene) had relatively high E_e 46 Kcal mol^{-1} (polyester, and 30 Kcal mol^{-1} for styrene). It is not surprising that densely crosslinked polymers would require additional energy to create mobile ions.

All of these AFM measurements were performed at ambient temperature. Elevated temperatures are known to accelerate ageing and degradation – possibly in part due to the generation of ions within the polymer. Although further work could be done at elevated temperatures, this would be outside the scope of this work as it aims to determine contributory factors and predict corrosion location prior to defects and degradation.

6.4.2 Capacitance

The setup for CSAFM may be compared to a capacitor – two electrodes separated by an insulator or weakly conducting substance [169] (Figure 71). The insulator prevents the current from flowing from one electrode to another, however the application of a voltage creates a potential across the two electrodes. In the AFM, either the tip or the sample is set to a bias voltage, setting up a potential between the tip and the substrate with the polymer sample filling the entire gap. In the case of the AFM, the voltages are relatively small (0 V to 10 V). In theory, the bias voltage can be charged at the start of the scan. It is unclear if a quick scan speed affects the bias voltage applied if some current moves though the sample.

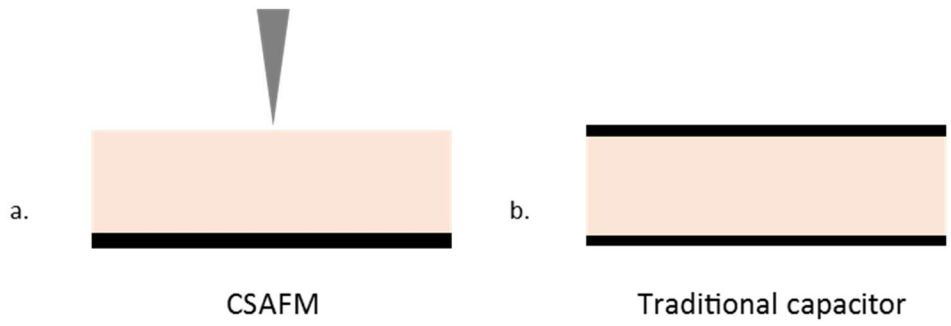

Figure 71: Schematic comparison of CSAFM and traditional capacitor

In a capacitor filled with a dielectric, no current will pass through the dielectric until the breakdown potential is exceeded. Polystyrene has a published dielectric strength of 24 kV mm^{-1} [169]. For samples of polystyrene of 5 µm thickness, the AFM would not be expected to detect current through the sample because the 10 V equipment maximum would not exceed the breakdown potential (120 V μm^{-1}). However, a commercially available unsaturated polyester was reported to have a breakdown potential of 8 kV mm^{-1} (40 V μm^{-1}) [173]. These are macroscopic values. If the polystyrene is 24 kV mm^{-1} and the average is 8 kV mm^{-1}, the value of the unsaturated polyester alone, would be expected to be somewhat lower. For the dielectric breakdown of to be exceeded, it would need to be within 10 V per 5 µm, or 2 V μm^{-1}. It is unclear if the unsaturated polyester alone would be that low, or if any area through the entire thickness of the sample would be low enough to overcome the dielectric breakdown. However, exceeding the breakdown potential would create ions and therefore increase the conductivity by damaging the sample.

A wide difference between the dielectric strength of the polyester and the polystyrene would be ideal for the detection on a nanometre scale, if the lateral resolution were sufficient to distinguish between the areas rich in each of the two types of polymer without damaging the sample.

6.4.3 Differences in microstructure between 15 µm and 5 µm

When Reiter and Naptolitano discussed the effect of thickness on the properties of glassy polymer films [174] they concluded that preparation methods are key to understanding the differences in the resulting properties due to the way polymers modify their conformation when cured in confinement. In industrial situations unsaturated polyester coatings are normally spray applied or sometimes by brush, lay-up, or roller. Each of these are expected to give slight differences, though they are not expected to be perceptible in practice. Spray application is likely to be the most irreproducible due to many competing factors, such as air pressure, tip size, temperature, rheology, etc. There is more styrene lost during spray application than other methods, and this is known to affect the microstructure of the cured coating (Sections 2.1 and 5.1). Spray applied samples can also be more unpredictably porous if the surface tension of the liquid resin does not allow both the full wetting of the surface and for the landed droplets to coalesce to a continuous film. Differences might be detectable in academic studies, but these application methods are generally impractical for the small-scale samples required.

Most academic work is done on solvent-reduced, spin-coated films of tens of nanometre thickness, though these are rarely crosslinked polymers. These may be useful to consider foundational principles, these polymers are very far removed from commercial coatings. The idea

that thinner films have weaker entanglements may still apply. Fewer molecules will be in the bulk of the sample – though it is unclear how much this would affect polyester coils expected to be less than 100 Å (10 nm) [19]. The scale effect of reducing polymer thicknesses to the range of nanometres is extensively studied and in the process of being understood. However, these effects are not reported for samples in the 5 to 15 µm range.

In addition to weaker entanglements [174], thin films have been found to have lower T_g due to the reduced free volume for thermal expansion [157]. Considerable work has been done on the way T_g is affected by film thickness and various annealing schemes [175]. Annealing below the T_g was found to increase the surface diffusion and create unusual ageing phenomena [174]. It is unclear how this may relate to performance in accelerated ageing tests which often use temperature to accelerate the results.

Curing the sample under a coverglass may have effects beyond that of constraining the microstructure via entanglements. A resin/glass interface is materially different than a resin/air interface in several ways. The solid glass provides more of a physical constraint than air, but it is unclear how this physical restraint affects the surface and the microstructures within. Generally, it might be expected to constrain the microstructures from forming in three dimensions. Conversely, resins tend to shrink during cure and the capillary forces from the liquid surface could induce the resin to fill the entire volume rather than shrinking back as would normally occur in air. It is unclear which of these opposing forces would dominate and if the constrained coating will be denser due to physical limitations or less dense due to filling the space that would otherwise be shrinkage.

In addition to the physical constraint of a resin/glass interface, the reduction in air at the surface, particularly oxygen could be relevant. Unsaturated polyester coatings are known to have issues with oxygen inhibition during curing. Oxygen at the surface during cure may retard the reaction such that the coating remains soft, sticky, and not fully cured. Commercial coating formulations often contain a wax that helps to keep oxygen from the surface and also claims to supress styrene evaporation. While this resin has not shown any signs of oxygen inhibition in these samples, nonetheless there may be invisible effects to the reduction of oxygen at the surface – such as a fuller cure.

6.4.3.1 *Contact angle measurements*

The hydrophobic or hydrophilic nature of a sample surface can be measured by the contact angle of distilled water on a surface. Figure 72 shows the idealised drop on a uniform, smooth, impermeable surface. Young's equation relates the contact angle on an ideal surface to the surface energy (equation 6) [176].

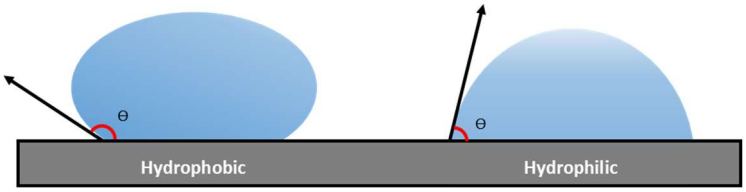

Figure 72: Schematic of contact angles of a water drop on idealised surfaces.

$$\gamma_{sl} + \gamma cos\theta = \gamma_{so} \quad \ldots\ldots (6)$$

Where:

γ_{sl} *is solid/liquid interfacial energy*

γ *is liquid/gas surface tension*

γ_{so} *is solid/gas surface energy*

However, in practice, surfaces are not ideal. Although attempts were made to keep the samples smooth for the purposes of AFM, they are not ideally smooth, and the topography changed during exposure to salt fog. There are two possible models for the effect of a rough surface on contact angle. The Wenzel model assumes the whole surface is wetted under the drop as in Figure 74, whereas the Cassie-Baxter model aims to take into account air entrapped under the water drop (Figure 73)[177][178].

$$\cos\theta_c = f_1 \cos\theta_1 - f_2 \quad \ldots\ldots (7)$$

Where the predicted or corrected contact angle is $\cos\theta_c$,

f_1 is the total area of solid under the drop,

$\cos\theta_1$ is the contact angle for a smooth sample

f_2 is the area under air.

Nb: the contact angle of air/water is assumed to be 180°, which reduces $\cos\theta_2$ to 1.

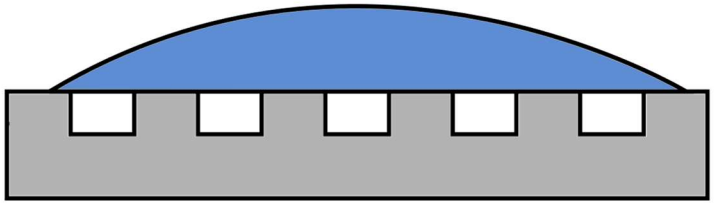

Figure 73: Depiction of the Cassie-Baxter model of contact angle on a surface with topographical features filled with air

Wenzel equation:

$$\cos\theta_w = r\cos\theta_1$$

Where the Wenzel contact angle (θ_w) is obtained by a using a roughness factor (*r*) rather than a projected area.

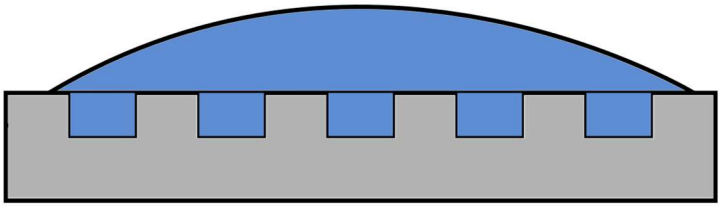

Figure 74: Depiction of the Wenzel model of surface wetting, which assumes a rough surface with the water droplet filling the topography of the surface

Unfortunately, samples in the real world are even more complex than these models. The degree to which air might be entrapped in the topography of the sample is difficult to estimate. The samples do not have uniform peaks and valleys as depicted in Figure 74 (see Section 6.6, p112). Additionally, the solid sample is not homogeneous and is comprised of both polystyrene and polyester molecules. This could be modelled with the full Cassie equation summing the proportions of each surface (including air, if entrapped). However, this modelling is beyond the scope of this thesis. In addition to challenges due to heterogeneity of the surface, the samples exposed to salt fog are likely to have sodium chloride surface contamination. These ions could introduce error by tending to decrease the contact angle by an unknown amount. Despite the likely error in the absolute contact angle measurements, the samples were measured to consider possible trends.

After the AFM measurements, the contact angle was measured on a variety of samples. Figure 75 shows the contact angle of samples after treatment with salt fog. The contact angle decreases significantly with salt fog exposure, indicating reduced hydrophobicity at the surface. Increased duration of salt fog exposure appears to reduce the contact angle in a relatively linear manner,

though additional data points would be beneficial. (Samples were made for the AFM and longer exposure times were not available at the time of test.)

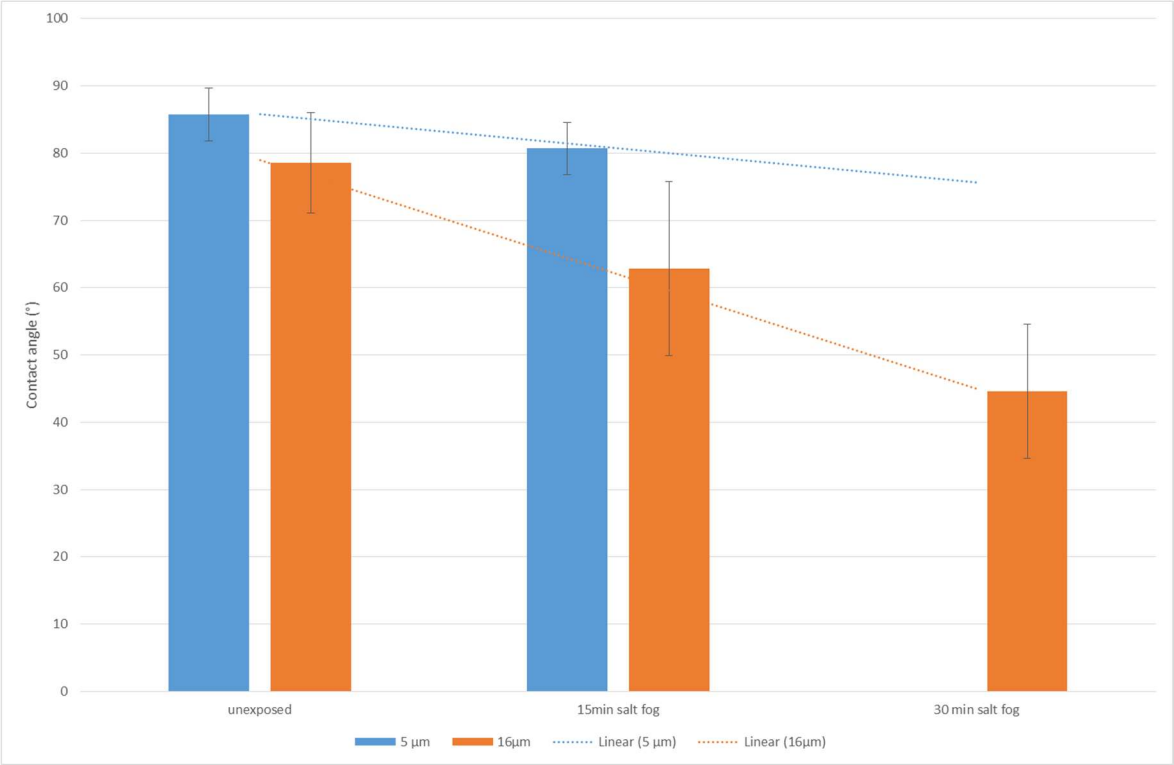

Figure 75: Contact angle of distilled water on unsaturated polyester resin of two thicknesses exposed to salt fog with error bars of one standard deviation. Hydrophobicity clearly decreases with increased exposure to salt fog. This effect is reduced for the thinner sample.

As discussed above, it is understood that the increased topographical changes (though small) affect the contact angle and therefore measured surface energy of the samples. Table 10 show the uncorrected contact angle values together with topography measurements by Alicona and AFM. These two measurements result in significantly different values due to the sample area used. Indeed, even the trends are different. The roughness of the unexposed 15 µm thick sample is larger than the exposed values by Alicona, but smaller by AFM. At 2.5x magnification, the Alicona images an area of approximately 5.6 x 4.3 mm, whereas the AFM scans in Table 10 are only 10 µm square. The Alicona method gives a more accurate picture of the roughness encountered by a contact angle water drop due to its larger scale. Additionally, the period of any waviness of the sample may be too large to be detected by the AFM.

Table 10: Uncorrected contact angle of distilled water on sample surfaces of two thicknesses exposed to salt fog, and roughness data by Alicona and AFM.

		Contact angle	R_a by Alicona 2.5x	AFM topography 10µm scan
15 µm	**unexposed**	78.6°	1311 nm	<2 nm, Figure 84, p116
	15 min salt fog	62.8°	927 nm	<80 nm, Figure 85, p117
	30 min salt fog	44.6°	981 nm	<30 nm, Figure 86, p118
5 µm	**unexposed**	85.7°	unavailable	<10nm, Figure 87, p119
	15 min salt fog	80.7°	unavailable	<20 nm, Figure 88, p120

In addition to the reduced change in contact angle with salt fog exposure, thinner samples were more hydrophobic when unexposed (Figure 76). This trend did not remain linear at much higher thicknesses, but did continue. It would be counter-intuitive to think that extremely thick samples would eventually become hydrophilic. Again, additional data points would be beneficial to this discussion. Traditionally, barrier coatings are applied at the maximum thickness without drips or sagging to provide the longest path for water to penetrate to the asset surface. If the hydrophobicity decreases with thickness, this may not be the most performance enhancing strategy – nor the most cost-effective.

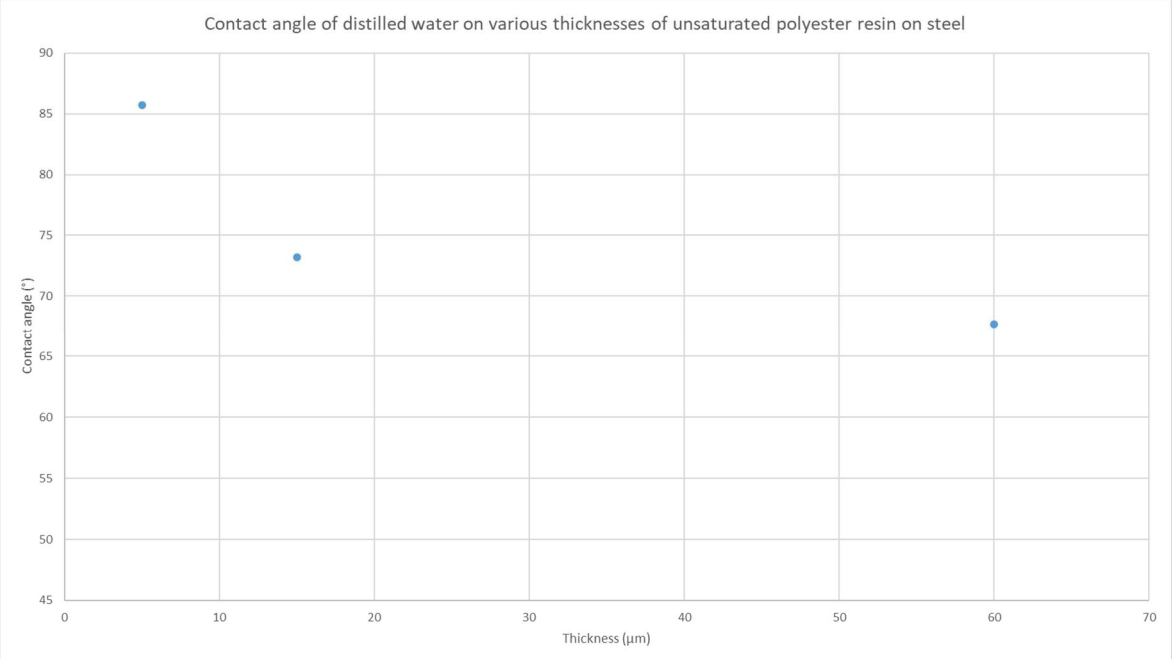

Figure 76: Contact angle on samples of unsaturated polyester coating over a range of thicknesses. The contact angle is reduced at higher thicknesses indicating that thinner films become increasingly more hydrophobic.

As well as considering the effect of salt fog exposure, contact angles of thin (5 µm) samples exposed to other treatments were measured (Figure 77). The salt fog showed the largest decrease in contact angle – corresponding to the largest decrease in hydrophobicity. This is interesting as ASTM B117 is a combination of several of the other treatments. The salt fog encompasses liquid water condensation, water vapour, and a 35°C temperature, as well as ions. Exposure to distilled water in liquid form showed the second-largest reduction in contact angle, suggesting that it is the strongest driver of hydrophobicity reduction in the salt fog – though the effect of ions cannot be judged by these samples. As discussed previously (Section 5.3), annealing below the T_g (like 35°C) causes a drop in the T_g of around 8K. The T_g was not measured, but the contact angle decreased slightly, but within the margin of error. Interestingly, the sample exposed to humidity showed a small increase in hydrophobicity. This is larger than the change due to heat, but may still be within margins of error.

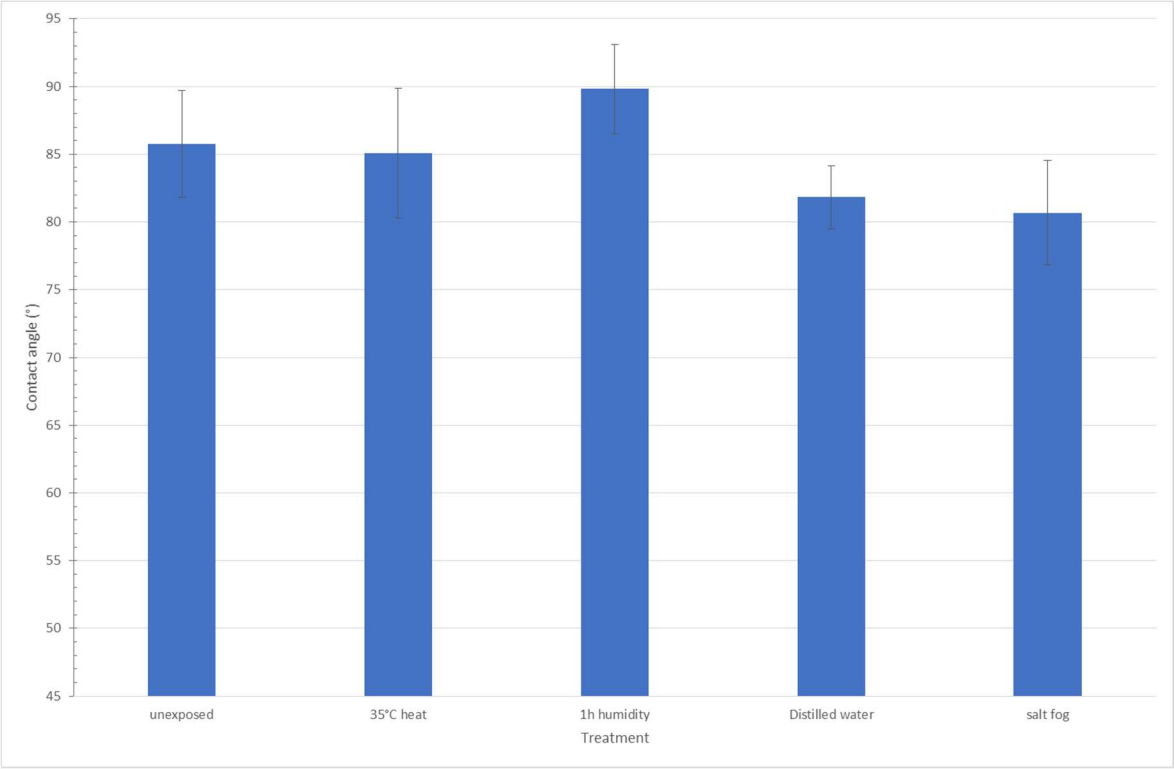

Figure 77: Contact angle of distilled water on 5 µm thick unsaturated polyester resin exposed to various treatments with error bars of one standard deviation

By looking at two different scales in chapter 5, features were found that were tens of microns as well as hundreds of nanometres. By reducing the film thickness and curing under a coverglass, the volume available for these structures is reduced and the surface interface has changed. There may no longer be enough material available to form the microgel structure seen in previous chapter, and thus the salt fog exposure would no longer produce the same raised structure

(Figure 78). Without microgels, the areas of concentrated hydrophilic nature are greatly reduced, and the changes are reduced from 3-dimensional to 2-dimensions. This may reduce the water absorption generally, and would reduce the swelling caused by the concentration of water absorption in hydrophilic areas. Without microstructures, the coating would be a comparatively uniform blend of styrene and unsaturated polyester. As such, it would be essentially impossible to detect any areas of increased conductivity. Therefore, further reducing the sample thickness to bring the dielectric breakdown potential into a range compatible with the instrument might prevent the microstructures from forming and any relevant data from being collected.

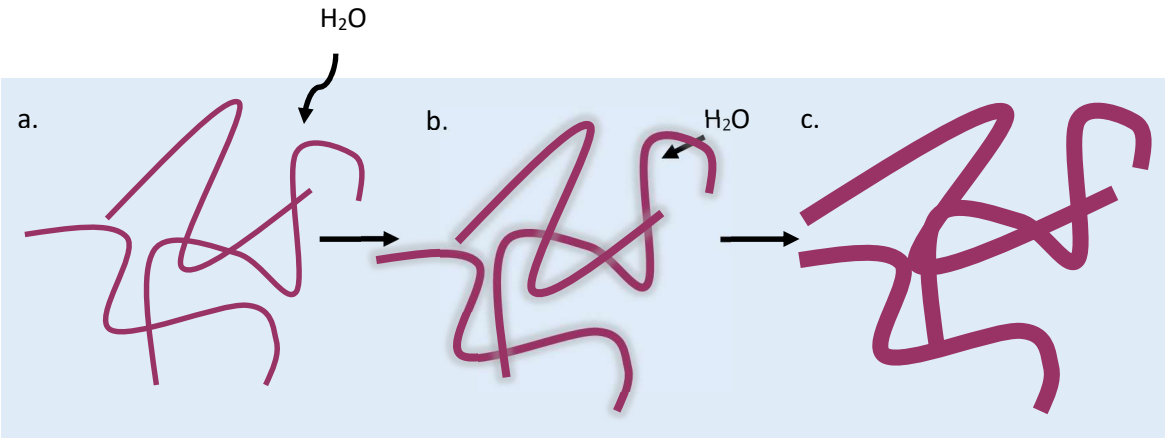

Figure 78: (compare with Figure 50, p83) Schematic visualising the way a thin film (around 5 µm) with an irregular polymer structure would not concentrate the water and ions, therefore absorbing less water and distributing it more evenly, thus not swelling microstructures visibly above the background polystyrene. In Figure 50, water is absorbed by the polyester microgels, the volume of the microstructures increases, eventually raising them above the surface of the polystyrene.

6.5 Summary

The CSAFM equipment and method were validated by scanning a sample of VHS tape. This produced a detectable increase in current as the voltage was increased. However, a change in current above the baseline was not detected for unsaturated polyester coating samples. It was shown that this unsaturated polyester coating does not obey Ohm's Law in the voltage range of 0 to -10 V.

Scale effects were shown for much larger thicknesses than previously reported. Thinner films exhibit greater hydrophobicity across a wide range of thicknesses. This may be due to significant changes in the microstructure formation during cure. The microstructure seen in the thick samples of clusters of polyester microgels surrounded by polystyrene branches is not seen in the thin films. However, the more uniform microstructure of the thin films has shown some advantages in hydrophobicity and resistance to ageing and deterioration.

6.6 SUPPLEMENTAL IMAGES

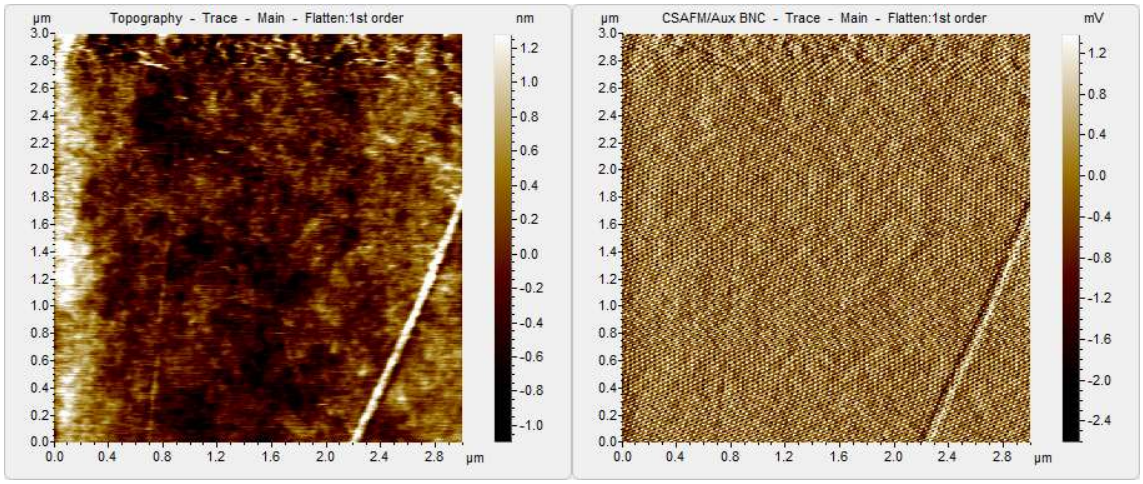

Figure 79: typical scan of cured unsaturated polyester resin, unexposed. Due to software issues, the CSAFM is reported as mV rather than mA. Keysight were contacted but were unable to provide a solution to this issue.

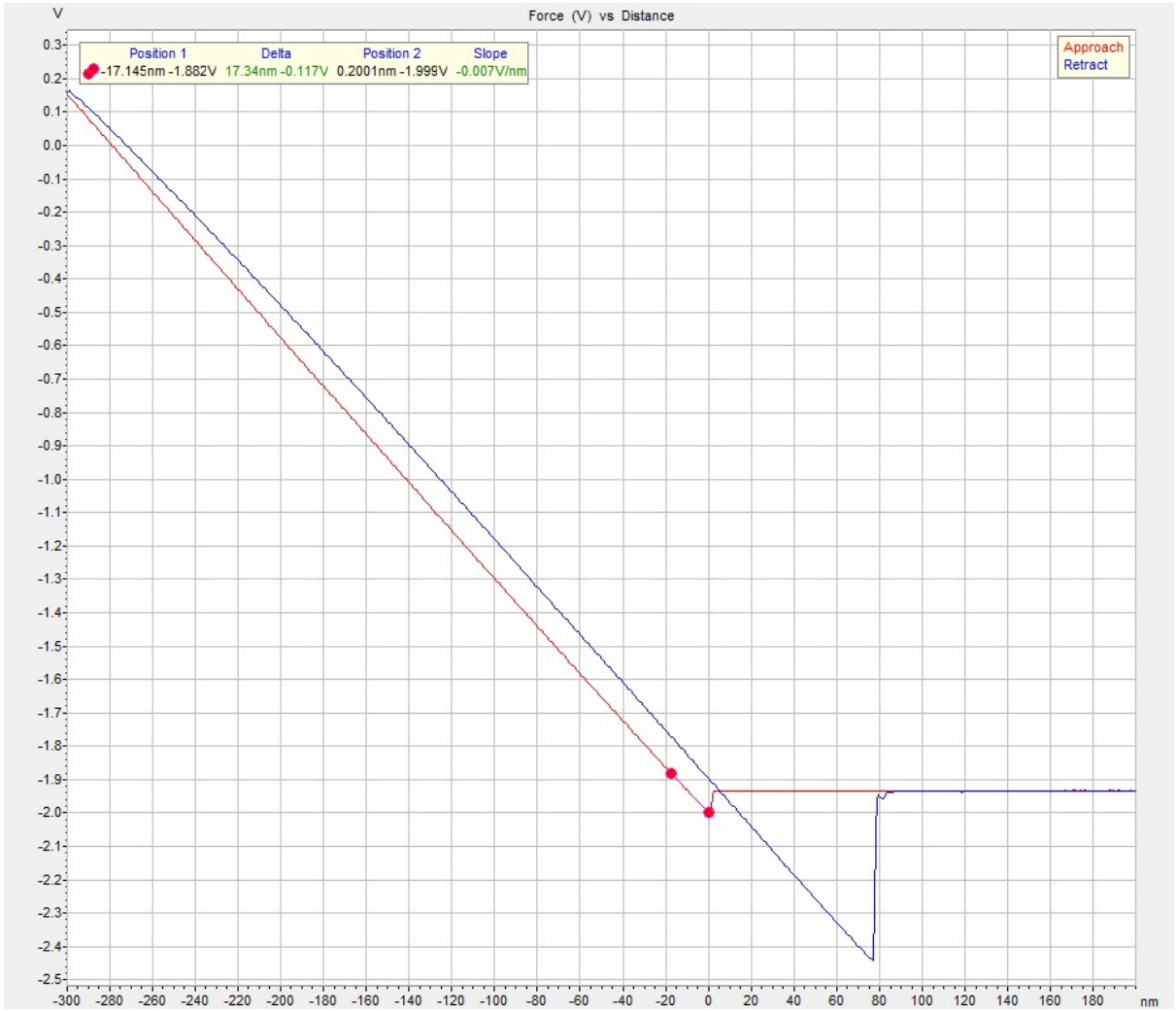

Figure 80: Force distance curve for the images in Figure 57. Deflection sensitivity was measured to be 148.4 nm V-1 (from -2V to -1.88V, in red). The hysteresis seen in this curve (compare to ideal force distance curve Figure 24, p52) may be due to viscoelastic deformation, piezo drift or both.

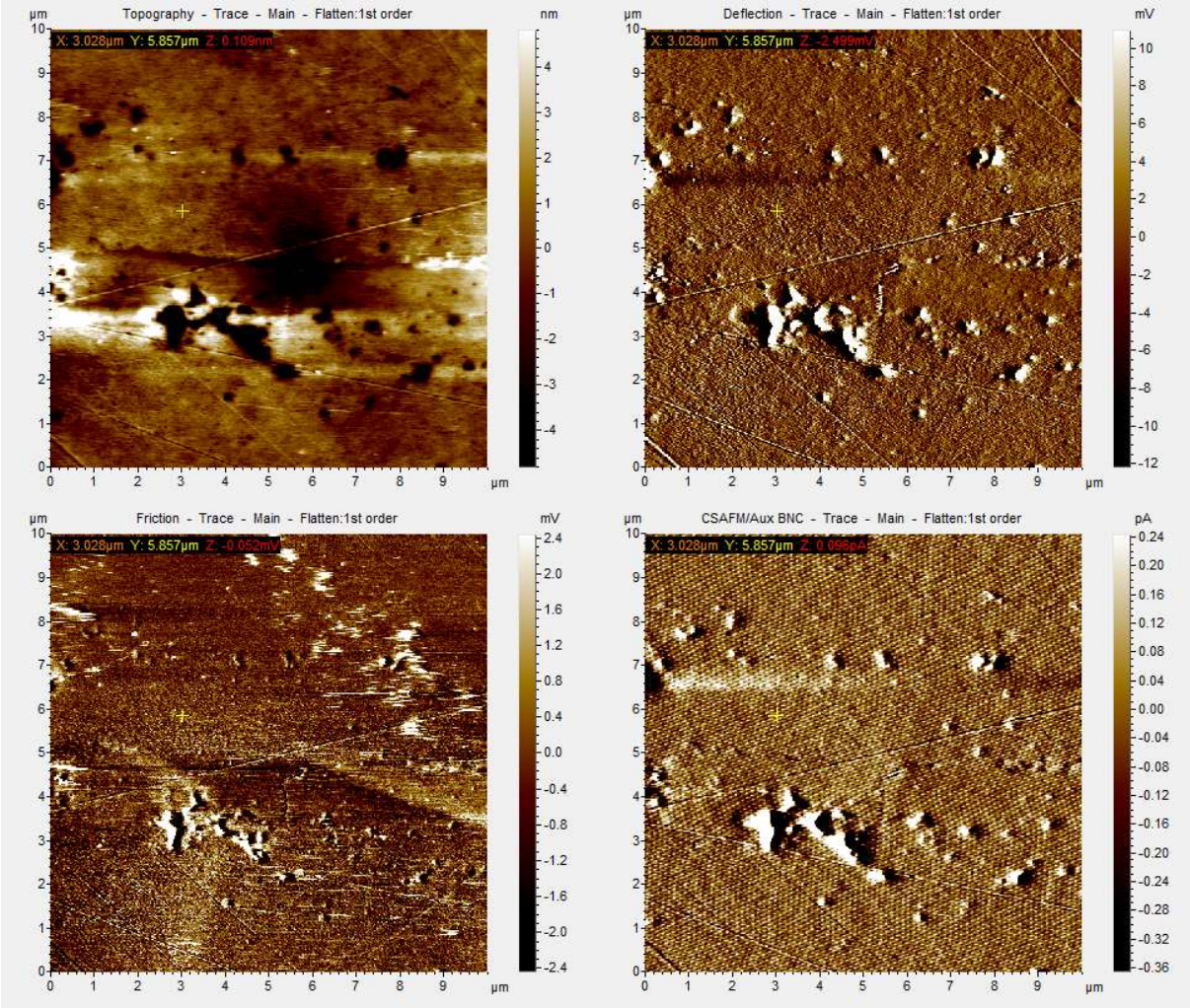

Figure 81: same as Figure 57, p90, but with different location indicated measuring topography

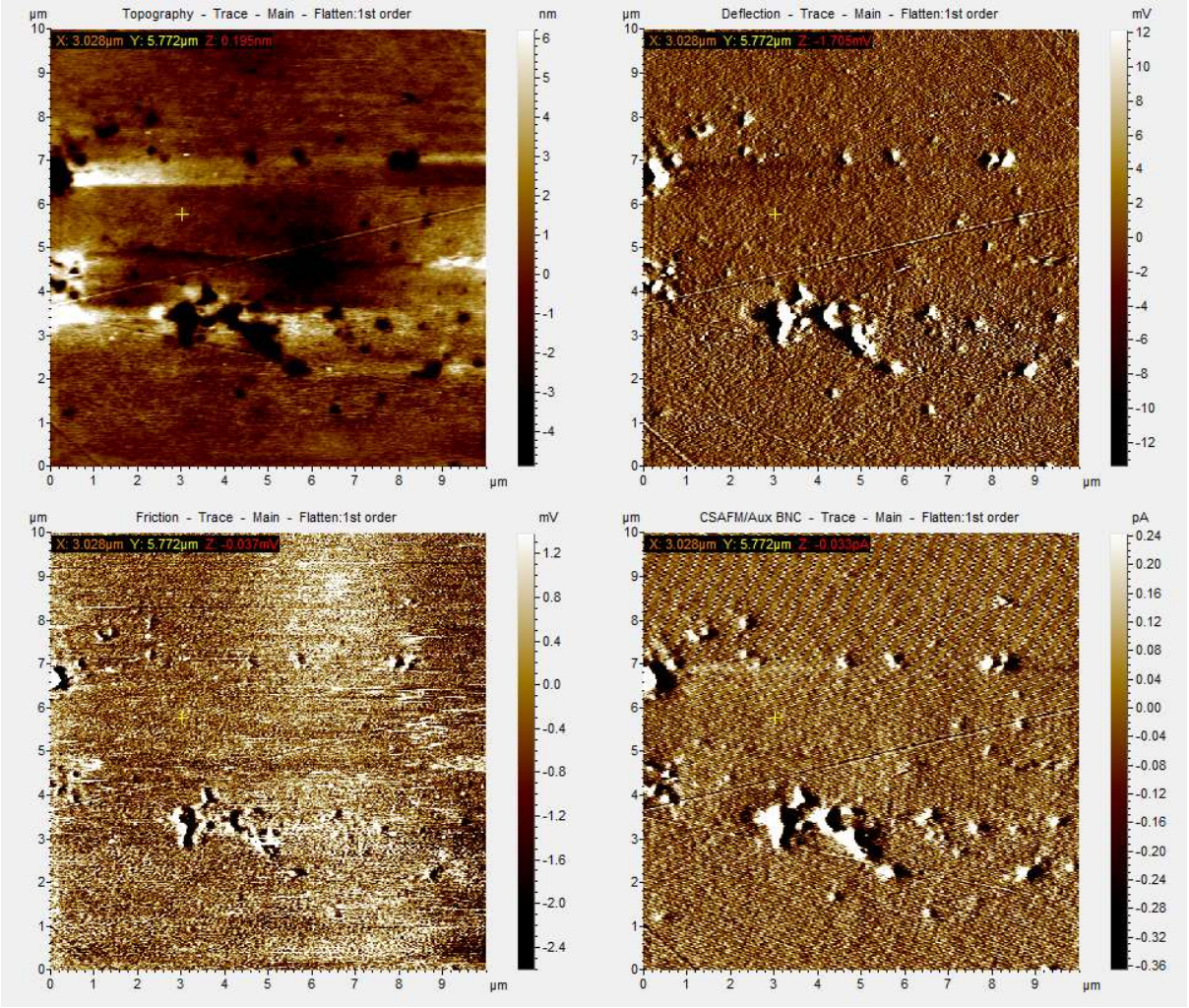

Figure 82: 0.2 V, same as Figure 58 - other location

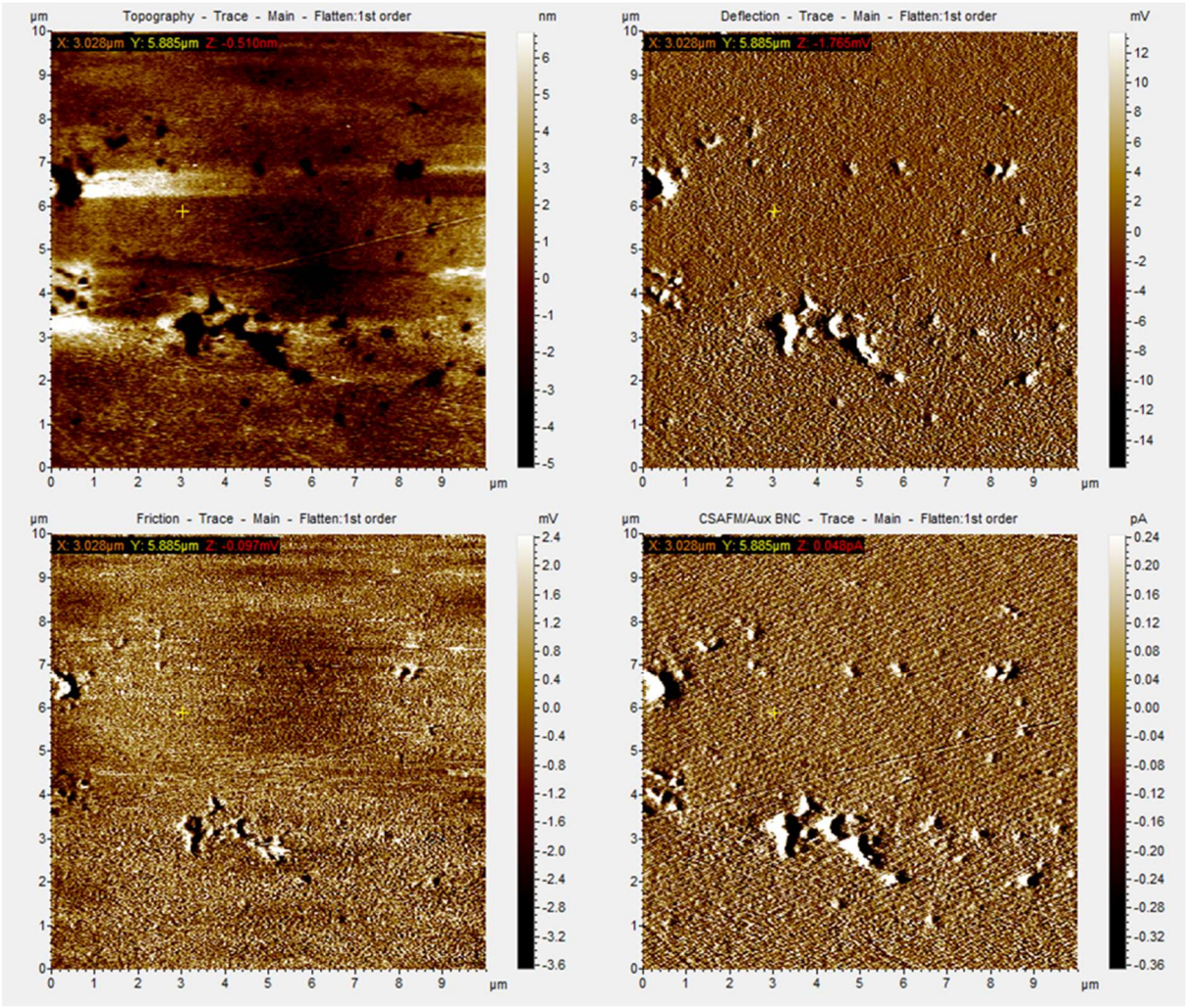

Figure 83: same as Figure 59 with other location highlighted (3V)

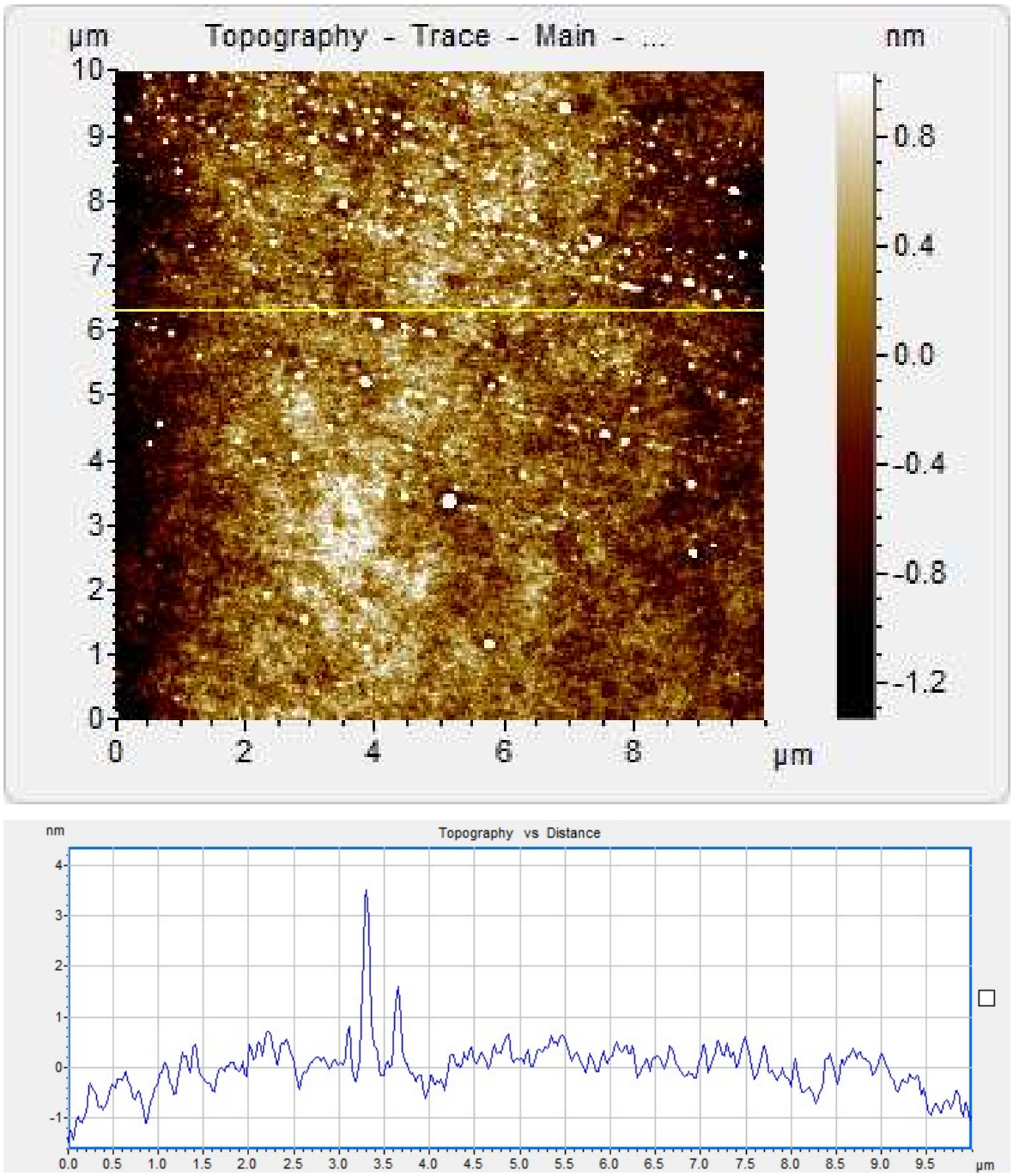

Figure 84: AFM topography and line profile of 15 µm thickness unsaturated polyester, unexposed

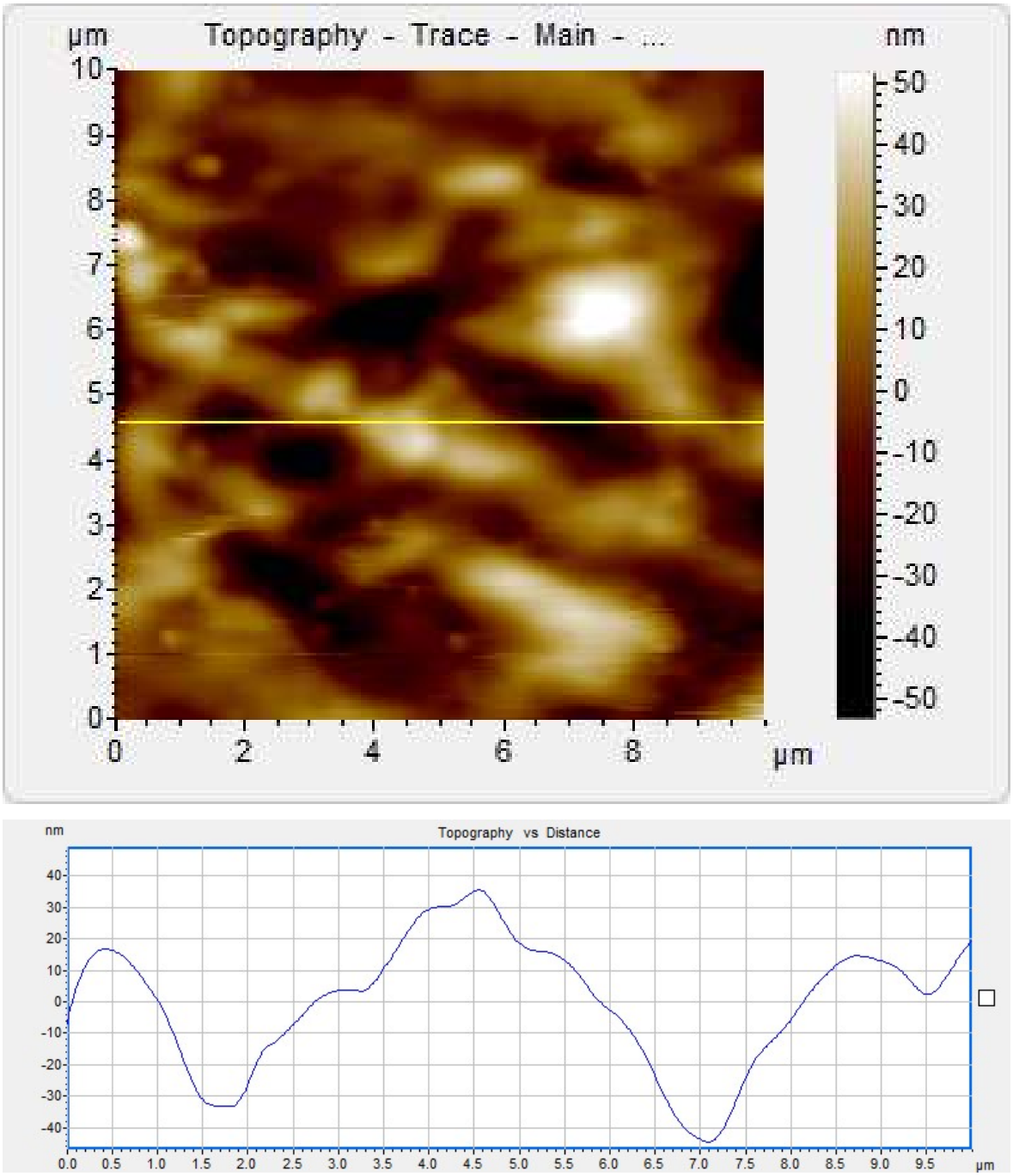

Figure 85: AFM topography and line profile of 15 µm thickness unsaturated polyester, 15 minute salt fog exposure

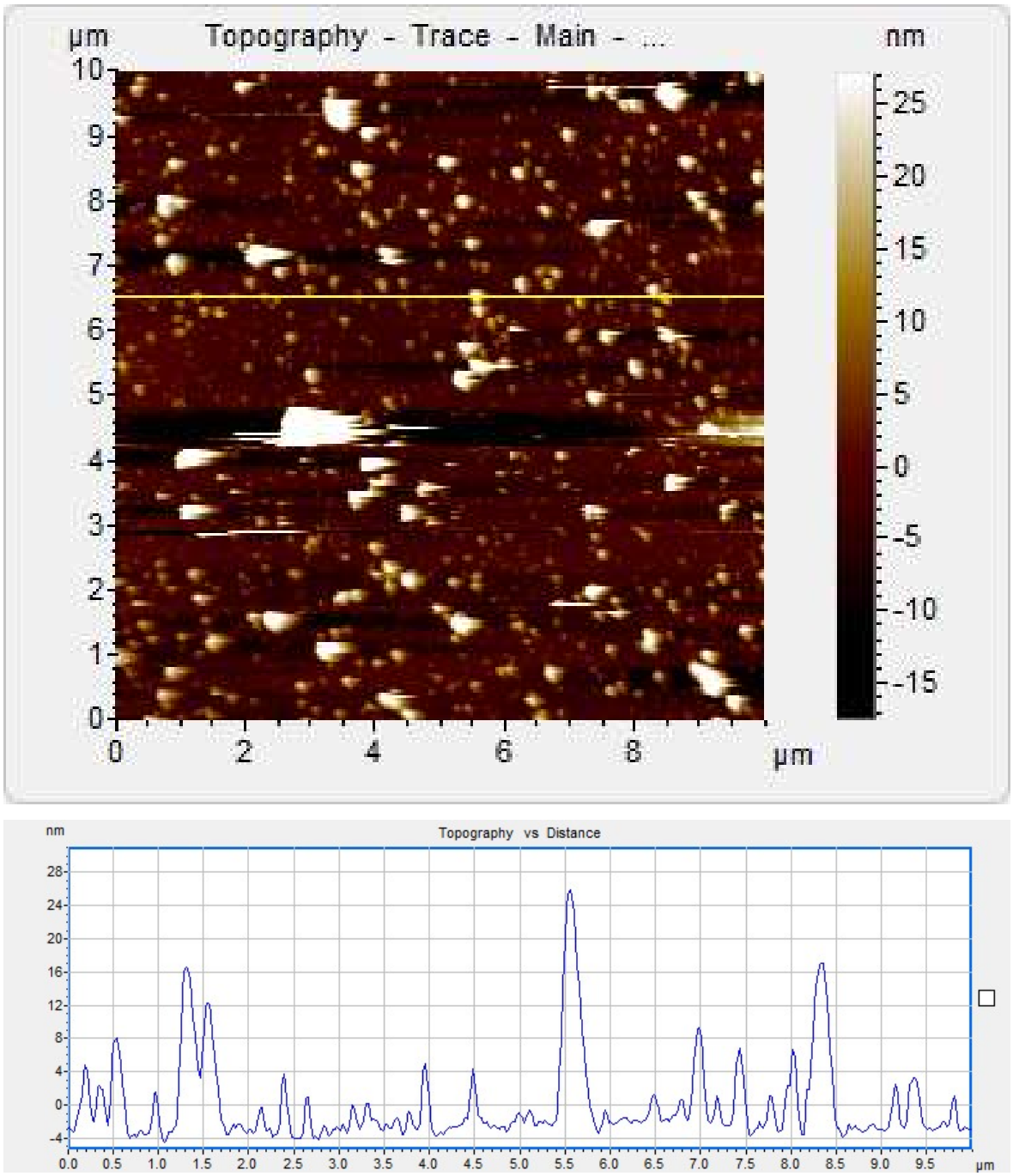

Figure 86: AFM topography and line profile of 15 µm thickness unsaturated polyester, 30 minute salt fog exposure

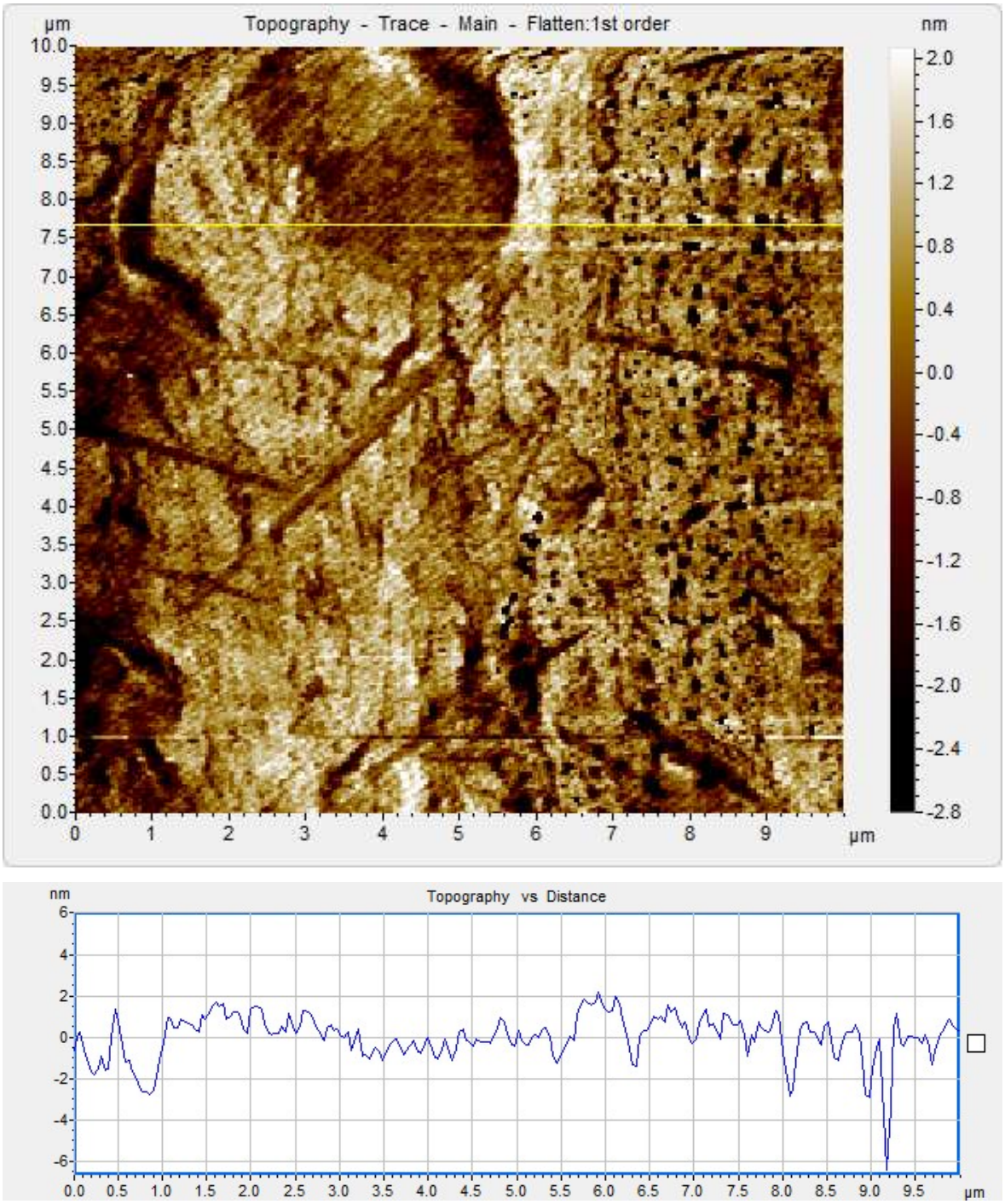

Figure 87: AFM topography and line profile of 5 µm thickness unsaturated polyester cured under coverglass, unexposed

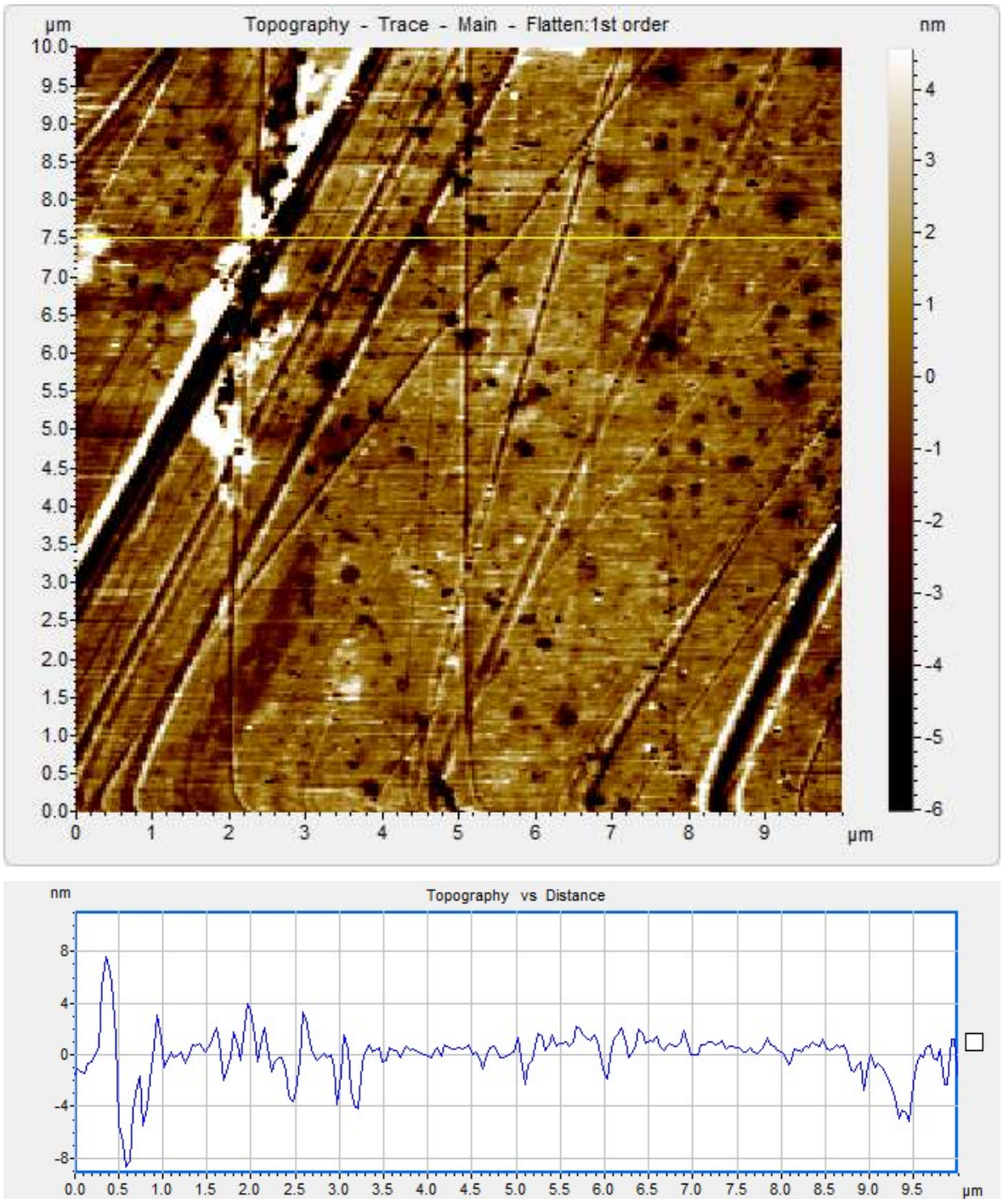

Figure 88: AFM topography and line profile of 5 µm thickness unsaturated polyester cured under coverglass, 15 min salt fog exposure

7 General Discussion

Unsaturated polyester coatings are still strong players in the marine and protective coating markets due to their long history of use and their comparatively cost-effective protection. Instrumentation that was not available when unsaturated polyester coatings were first commercialised has been used to investigate long-standing questions regarding the polymer morphology and mechanisms of corrosion protection.

Commercial unsaturated polyester coatings are comprised of unsaturated polyester polymer and styrene monomer. Styrene monomer is relatively non-polar while the unsaturated polyester contains polar chain ends. These differences lead to a phase separation where the unsaturated polyester forms coils and then microgels, which are surrounded and crosslinked with the styrene monomer or chains of polystyrene. Previous work has relied on fracturing, solvent washing, or laser ablating to reveal and confirm the two-phase microstructure. After only a short exposure to ASTM B117 salt fog, these microstructures were visible by optical microscopy and AFM. Although salt fog is also a treatment, it is designed to simulate conditions experienced in the field, whereas the previous treatments are wholly artificial.

The polymer provides the majority of the performance of a commercial coating and therefore the properties given by the microstructures are of great interest. Marine protective coatings prevent corrosion by baring the passage of ions through the coating to the surface. The migration of water and ions through the coating is governed by the electrical nature of the coating. Ions and water must have sufficient physical space to move, but transport is also enhanced by electrical current and polar regions in the polymer. Electrical current requires an electrical path using existing charge within the coating at short enough distances to jump. Freshly applied, defect-free coatings do not contain enough charges to make the electrical connection. However, after exposure to light, water, ions, etc, these charges become more prevalent in the coating – through migration or degradation of the polymer. Eventually, the ions reach the interface and the corrosion reaction proceeds.

In considering how the water and ions are likely to migrate through the coating, the electrical properties of the microstructures are relevant. KPFM measures the surface potential at high lateral resolution and has shown that polyester and polystyrene are detectably different. CSAFM has the ability to map current through a sample, as validated by standard VHS tape. However, the prevalence of charges was too low to complete the circuit for freshly prepared polymer samples at 15 µm thickness. Thinner samples (5 µm) were prepared and exposed to various treatments.

Thinner samples were expected to respond more quickly to exposure, following the traditional logic of barrier properties. However, these samples proved to be more highly hydrophobic than the thick films.

Increased hydrophobicity in thin films is an unexpected and interesting result. In addition to this surface effect, the microstructure visible previously, was no longer visible. Scale effects have previously been reported in polymers in the range of 10s to 100s of nanometres. Differences have not been previously reported for polymers between 15 µm and 5 µm. In practice, these coatings are not used in thicknesses of 5 µm or 15 µm, but 750-1000 µm. This work has produced some evidence that hydrophobicity decreases with increasing thickness and thus the ease of polymer degradation increases past 15 µm, though it is unclear how the effects scale to thicknesses 100x greater. In addition to the overall thickness, commercial formulations are not made up of resin alone (Section 2.1.3). The addition of liquid additives and solid particles gives rise to the possibility of countless microscopic interfaces throughout the coating. If these were to constrain the coating to a small dimension between these interfaces, it is unclear if the scale effects shown here would still apply.

8 CONCLUSIONS

Alicona optical microscopy and atomic force microscopy were able to produce images of the polymer microstructure without the potentially damaging methods of solvent washing, laser ablation, and cracking used in previous studies. These images are important direct corroboration of the predicted microstructure for the first time.

- It was confirmed that a branched network similar to those previously reported [19] could be seen in one commercially available, unaccelerated, non-thixotropic isophthalic unsaturated polyester resin after short-term exposure to salt fog when scanned by an Alicona InfiniteFocus 3D Optical microscope (Figure 40, p73) and an Atomic Force Microscope (Figure 44 and Figure 45, p76).
    - The features imaged by AFM are on a much smaller scale than the features and surface profile changes seen by the Alicona. This has shown that the structure formed contains clusters of microgels and globules in a wide range of sizes from nanometres to micrometres.
    - KPFM analysis indicated that differences in surface potential can also be detected after exposure to salt fog (Figure 47, p78).
    - CSAFM analysis (Chapter 6) showed that the microstructure does appear to have differences in electrical properties at 15 µm thickness. However, films of 5 µm lack the expected microstructure, but possess greater, more stable hydrophobicity. These previously unreported scale effects may have applications for commercial formulations.

After visual and AFM confirmation of the expected microstructure, attempts to correlate these structures with highly localised electrical properties were unsuccessful due to previously unreported scale effects. Based on the results and discussion contained herein, the following generalised theory of conductivity in polymers is suggested.

Unsaturated polyester resins form coils to shield the polar ends from the non-polar styrene. During curing, there is some additional movement due to increased temperature, but the free-radical curing timescale of around 30-60 minutes allows the phase separation to occur. Unreacted monomers, water, and ions are generally separated into the more polar phase. Initially, these polar regions are too far apart to facilitate conductivity through the polymer. However, as the coating is exposed to water and ions, these move preferentially towards the polar molecules, causing the swelling seen in Chapter 5. As water moves through the coating, it

hydrolyses polymer molecules at ester linkages (Section 5.3), increasing the number of chain ends in regions of previously non-polar character. This self-perpetuating effect increases the availability for charge transport as well as the ease of water and ion migration. At some point, a critical volume of charge is available, and the electrical path through the coating can be completed. Unfortunately, it is not yet possible to link any structures to higher probability of hydrolysis. Though reasons for the lack of conductivity cannot be conclusively determined from this work, it has added to the pool of scientific evidence surrounding theories of ion migration and conductivity in polymers.

In the samples where the curing was constrained, the influence of the glass interface may have caused a denser packing of polystyrene molecules. These are naturally more hydrophobic and account for some of the surface hydrophobicity seen by the contact angle measurements in Section 6.4.3. The effects of this interface must penetrate beyond the surface though, as the microstructure seen in Chapter 5 is not visible in these samples. It is unclear how this effect is passed through several microns of coating. However, it seems clear that the delocalised nature of the polar chain ends, residual water, ions, and monomers avoids the strongly polar regions that attract further water – causing hydrolysis. Methods of incorporating this into commercial development should be investigated further.

9 FUTURE WORK

There are several areas that this work could be expanded. Perhaps most simply, the electrical properties could be investigated with a higher bias voltage. Instrumentation is always improving and features on new machines that allow a greater field of vision while selecting areas to scan would also be of great interest. If features could be located repeatedly, it may be possible to confirm how the topographical and structural changes progress after exposure to salt fog or other environmental stressors.

The more interesting work, however, would be to further explore the scale effects. Polymer scale effects are widely reported for monolayers or thicknesses in the tens of nanometres. Significant behavioural changes in polymers have not been previously reported between 5 µm and 10 µm thickness. As it is unclear if this is a gradual change or there is a minimum volume for the structures to form. It would also be interesting to consider thicknesses below 5 µm. This could further advance the formulation of coatings by identifying a target microstructure which may be engineered through formulation or polymer design.

Formulation of a protective coating has always been a balance – of cost vs performance, of chemical resistance vs flexibility, of durability vs ease of use. A great deal of the assumptions these balances are based on come from long-standing, but ultimately unproven rules of thumb. Old theories of barrier properties have argued that thicker films give the water and ions a longer path to travel, increasing protective time. The work here challenges that long-held assumption. If thinner films are less prone to hydrolysis and degradation, it will be a challenge to bring that technology to the next generation of coatings.

10 REFERENCES

[1] D. Ebbing, *General Chemistry*, 5th ed. Houghton Mifflin Company, 1996.

[2] T. Mezger, *Applied Rheology*. Graz, Austria: Anton Paar, 2014.

[3] L. H. Sperling, *Physical Polymer Science*, 3rd ed. John Wiley & Sons, Inc, 2001.

[4] F. Mercier, T. Hijikata, and V. Burrai, "Steel Market Developments Q2 2020," 2020. [Online]. Available: https://www.oecd.org/sti/ind/steel-market-developments-Q2-2020.pdf.

[5] M. Pooler, "ArcelorMittal Offers Bullish Assessment of Global Steel Market," *Financial Times*, Nov. 2017.

[6] R. Bhaskaran *et al.*, "An Analysis of the Updated Cost of Corrosion in India," *Mater. Perform.*, vol. 53, no. 8, pp. 56–65, 2014.

[7] E. Armelin, R. Oliver, F. Liesa, J. I. Iribarren, F. Estrany, and C. Aleman, "Marine Paint Fomulations: Conducting Polymers as Anticorrosive Additives," *Prog. Org. Coatings*, vol. 59, no. 1, pp. 46–52, 2007, doi: 10.1016/j.porgcoat.2007.01.013.

[8] S. Mazumdar, "Opportunities for Thermoset Resins in the Composites Industry," 2008, [Online]. Available: https://www.trfa.org/erc/docretrieval/uploadedfiles/Technical Papers/2008 Meeting/Mazumdar-Lucintel_ppt-Composites_industry.pdf.

[9] "Unsaturated Polyester Resin Market - Global Industry Analysis, Size, Share, Growth, Trends And Forecast, 2013 - 2019," Albany, NY, USA, 2015. Accessed: May 22, 2015. [Online]. Available: http://www.transparencymarketresearch.com/pressrelease/unsaturated-polyester-resin.htm.

[10] V. A. Davis, "Rheological and Curing Properties of Unsaturated Polyester Resin Nanocomposites," in *Unsaturated Polyester Resins: Fundamentals, Design, Fabrication, and Applications*, Elsevier Inc., 2019, pp. 471–488.

[11] A. Jacob, "Vinyl Esters Lead the Corrosion Challenge," *Reinf. Plast.*, vol. 47, no. 6, pp. 32–35, Jun. 2003, doi: 10.1016/S0034-3617(03)00631-3.

[12] C.-I. Wu, X. Zhou, and Y. Tan, "A Study on the Electrochemical Inhomogeneity of Organic Coatings," *Prog. Org. Coatings*, vol. 25, no. 4, pp. 379–389, May 1995, doi: 10.1016/0300-9440(95)00553-Q.

[13] R. C. Bacon, J. J. Smith, and F. M. Rugg, "Electrolytic Resistance in Evaluating Protective Merit of Coatings on Metals," *Ind. Eng. Chem.*, vol. 40, no. 1, pp. 161–167, 1948, doi: 10.1021/ie50457a041.

[14] J. V Standish, H. Leidheiser, and H. Leidheiser Jr, "The Electrical Properties of Organic Coatings on a Local Scale-Relationship to Corrosion," *Corrosion*, vol. 36, no. 8, pp. 390–395,

1980.

[15] J. M. Sykes, E. P. Whyte, X. Yu, and Z. Sharer Sahir, “Does ‘Coating Resistance’ Control Corrosion?,” *Prog. Org. Coatings*, pp. 1–6, 2016, doi: 10.1016/j.porgcoat.2016.04.015.

[16] M. Dornbusch, “The Use of Modern Electrochemical Methods in the Development of Corrosion Protective Coatings,” *Prog. Org. Coatings*, vol. 61, no. 2008, pp. 240–244, 2008, doi: 10.1016/j.porgcoat.2007.09.035.

[17] S. R. Taylor, “Assessing the Moisture Barrier Properties of Polymeric Coatings Using Electrical and Electrochemical Methods,” *IEEE Trans. Electr. Insul.*, vol. 24, pp. 787–806, 1989.

[18] F. Zou and D. Thierry, “Localized Electrochemical Impedance Spectroscopy for Studying the Degradation of Organic Coatings,” *Electrochim. Acta*, vol. 42, no. 97, pp. 3293–3301, 1997, doi: 10.1016/S0013-4686(97)00180-1.

[19] Y. S. Yang and L. J. Lee, “Microstructure Formation in the Cure of Unsaturated Polyester Resins,” *Polymer (Guildf).*, vol. 29, no. 10, pp. 1793–1800, Oct. 1988, doi: 10.1016/0032-3861(88)90393-X.

[20] E. Kropa and T. Bradley, “Maleic Anhydride-Ethylene Glycol Methallyl Alcohol Resin,” 2,280,242, Apr. 21, 1942.

[21] G. Harris, “Unsaturated Polyesters Continue Their Reign,” *Reinf. Plast.*, vol. 40, no. 9, pp. 62–66, Sep. 1996, doi: 10.1016/S0034-3617(98)80195-1.

[22] E. Grazul, “History and Future of Unsaturated Polyesters,” in *Unsaturated Polyester Technology*, P. F. Bruins, Ed. Gordon and Breach Science Publishers Ltd, 1976, pp. 3–10.

[23] I. E. Muskat and F. Strain, “Polybasic Acid-Polyhydric Alcohol Esters and Polymers Thereof,” 2,384,115, Sep. 04, 1945.

[24] I. E. Muskat and F. Strain, “Unsaturated Esters and Polymers Thereof,” 2,401,581, 1946.

[25] M. Mallik, V. Choudhary, and I. K. Varma, “Current Status of Unsaturated Polyester Resins,” *J. Macromol. Sci. Part C Polym. Rev.*, vol. 40, no. 2–3, pp. 139–165, Jul. 2000, doi: 10.1081/MC-100100582.

[26] B. Mortaigne, B. Feltz, and P. Laurens, “Study of Unsaturated Polyester and Vinylester Morphologies Using Excimer Laser Surface Treatment,” *J. Appl. Polym. Sci.*, vol. 66, pp. 1703–1714, 1997.

[27] E. J. Carlson, “Copolymers of Vinyl Esters of Aliphatic Acids with Dialkenyl-Carbonate Esters of Alkylene Bis-Phenols,” 2,529,867, 1950.

[28] R. A. Franz, “Stabilization of Vinyl Compounds,” 2,361,538, 1944.

[29] A. M. Visco, L. Calabrese, and P. Cianciafara, “Modification of Polyester Resin Based Composites Induced by Seawater Absorption,” *Compos. Part A Appl. Sci. Manuf.*, vol. 39,

no. 5, pp. 805–814, May 2008, doi: 10.1016/j.compositesa.2008.01.008.

[30] "Phthalic Acid," *Sigma Aldrich*. https://www.sigmaaldrich.com/catalog/product/mm/822298?lang=en&region=GB&gclid=Cj0KCQjw4cOEBhDMARIsAA3XDRhDalOplFOmGo1g7QNM1mIFzwpxRdy8sI6zHh5cQ-6XRUR94gwzMfYaAkNIEALw_wcB (accessed May 04, 2021).

[31] "Isophthalic Acid," *ECHA*. https://echa.europa.eu/registration-dossier/-/registered-dossier/15373/4/9 (accessed May 04, 2021).

[32] E. M. Redline, L. F. Francis, and F. S. Bates, "Radical-Cured Block Copolymer-Modified Thermosets," *J. Polym. Sci. Part B Polym. Phys.*, vol. 49, no. 7, pp. 540–550, Apr. 2011, doi: 10.1002/polb.22196.

[33] A. S. Nyqnlst, C. Cob, and E. L. Kropa, "Unsaturated Alkyd Reacted with Unsaturated Isocyanate," 2,503,209, 1950.

[34] M. Lin, C. Liu, and C. Lee, "Toughened Interpenetrating Polymer Network Materials," *J. Appl. Polym. Sci.*, vol. 72, no. May 1998, pp. 585–592, 1999.

[35] "SafeCom," 2016.

[36] *Regulation 1907/2006/EC concerning the Registration, Evaluation, Authorisation and Restriction of Chemicals (REACH), establishing a European Chemicals Agency*. THE EUROPEAN PARLIAMENT AND OF THE COUNCIL, 2006.

[37] ECHA, "Candidate List of Substances of Very High Concern." http://echa.europa.eu/web/guest/candidate-list-table (accessed Jun. 08, 2015).

[38] J. F. G. A. Jansen and R. I. Kraeger, "Unsaturated Polyester Resin Compositions," US20140128553 A1, May 08, 2014.

[39] "Cobalt Free Accelerators," *AkzoNobel website*. https://www.akzonobel.com/polymer/our_products/thermoset_chemicals/accelerators_and_promoters/cobalt_free_accelerators.aspx (accessed Jun. 11, 2015).

[40] R. Committee for Risk Assessment, "Opinion Proposing Harmonised Classification and Labelling at EU Level of Styrene," no. November. European Chemicals Agency (ECHA), pp. 0–49, 2012.

[41] C.-P. Hsu, M. Y. Zhao, and S. L. Voeks, "Styrene-Free Unsaturated Polyester," US 8,906,999, 2014.

[42] K. Dusek, "Are Cured Thermoset Resins Inhomogeneous?," *Die Angew. Makromol. Chemie*, vol. 240, pp. 1–15, 1996, doi: 10.1002/apmc.1996.052400101.

[43] Y.-J. Huang and W.-C. Jiang, "Effects of Chemical Composition and Structure of Unsaturated Polyester Resins on the Miscibility, Cured Sample Morphology and Mechanical Properties for Styrene/Unsaturated Polyester/Low-Profile Additive Ternary Systems. 1: Miscibility and Cured Sample Mor," *Polymer (Guildf).*, vol. 39, no. 25, pp. 6631–

6641, Dec. 1998, doi: 10.1016/S0032-3861(98)00164-5.

[44] M. Shah, E. Zondervan, M. L. Oudshoorn, and A. B. de Haan, "A Novel Process for the Synthesis of Unsaturated Polyester," *Chem. Eng. Process. Process Intensif.*, vol. 50, no. 8, pp. 747–756, Aug. 2011, doi: 10.1016/j.cep.2011.06.009.

[45] C. King, "Polyesters for Use in Fiberglass Industry," 2010. [Online]. Available: http://nzic.org.nz/ChemProcesses/polymers/10B.pdf.

[46] E. M. S. Sanchez, C. A. C. Zavaglia, and M. I. Felisberti, "Unsaturated Polyester Resins: Influence of the Styrene Concentration on the Miscibility and Mechanical Properties," *Polymer (Guildf).*, vol. 41, no. 2, pp. 765–769, Jan. 2000, doi: 10.1016/S0032-3861(99)00184-6.

[47] E. Bureau *et al.*, "Fragility of Unsaturated Polyester Resins Cured with Styrene: Influence of the Styrene Concentration," *Eur. Polym. J.*, vol. 37, no. 11, pp. 2169–2176, Nov. 2001, doi: 10.1016/S0014-3057(01)00114-8.

[48] E. Rodriguez, M. Larrañaga, I. Mondragón, and A. Vázquez, "Relationship between the Network Morphology and Properties of Commercial Vinyl Ester Resins," *J. Appl. Polym. Sci.*, vol. 100, no. 5, pp. 3895–3903, Jun. 2006, doi: 10.1002/app.22732.

[49] F. Lionetto, R. Rizzo, V. A. M. Luprano, and A. Maffezzoli, "Phase Transformations during the Cure of Unsaturated Polyester Resins," *Mater. Sci. Eng. A*, vol. 370, no. 1–2, pp. 284–287, Apr. 2004, doi: 10.1016/j.msea.2003.07.025.

[50] "Palatal P 69-02 Product Data Sheet," vol. 010544/7.0, no. February 12.

[51] "Synolite 1717-N-1 Product Data Sheet," no. 006317/6.0.

[52] "Synolite™ 0288-I-1," no. 002588/12.0, 2016.

[53] R. Lambourne and T. Strivens, Eds., *Paint and Surface Coatings: Theory and Practice*, 2nd ed. Woodhead Publishing Limited, 1999.

[54] P. Penczek, P. Czub, and J. Pielichowski, "Unsaturated Polyester Resins: Chemistry and Technology," in *Crosslinking in Materials Science*, Springer Berlin Heidelberg, 2005, pp. 1–95.

[55] Health and Safety Executive, *The storage and handling of organic peroxides*. 1998.

[56] R. Toorkey, K. Rajanna, and P. Sai Prakash, "Curing of Unsaturated Polyester: Network Formation," *J. Chem. Educ.*, vol. 73, no. 4, pp. 372–373, 1996.

[57] H. Yang and L. J. Lee, "Comparison of Unsaturated Polyester and Vinylester Resins in Low Temperature Polymerization," *J. Appl. Polym. Sci.*, vol. 79, no. 7, pp. 1230–1242, 2001, doi: 10.1002/1097-4628(20010214)79:7<1230::AID-APP100>3.0.CO;2-2.

[58] C. P. Hsu and L. J. Lee, "Free-Radical Crosslinking Copolymerization of Styrene/Unsaturated Polyester Resins 3. Kinetics-Gelation Mechanism," *Polymer (Guildf).*, vol. 34, no. 21, pp.

4516–4523, 1993.

[59] H. Yang and L. J. Lee, “Effects of Resin Chemistry on Redox Polymerization of Unsaturated Polyester Resins,” *J. Appl. Polym. Sci.*, vol. 84, no. 1, pp. 211–227, 2002, doi: 10.1002/app.10317.

[60] C. P. Hsu and L. J. J. Lee, “Structure Formation during the Copolymerization of Styrene and Unsaturated Polyester Resin,” *Polymer (Guildf).*, vol. 32, no. 12, pp. 2263–2271, Jan. 1991, doi: 10.1016/0032-3861(91)90057-P.

[61] C. P. Hsu and L. J. Lee, “Free-Radical Crosslinking Copolymerization of Styrene/ Unsaturated Polyester Resins: 1. Phase Separation and Microgel Formation,” *Polymer (Guildf).*, vol. 34, no. 21, pp. 4496–4505, 1993.

[62] S. Ziaee and G. R. Palmese, “Effects of Temperature on Cure Kinetics and Mechanical Properties of Vinyl – Ester Resins,” *J. Polym. Sci. Part B Polym. Phys.*, vol. 37, pp. 725–744, 1999.

[63] M. Skrifvars, P. Niemelä, R. Koskinen, and O. Hormi, “Process Cure Monitoring of Unsaturated Polyester Resins, Vinyl Ester Resins, and Gel Coats by Raman Spectroscopy,” *J. Appl. Polym. Sci.*, vol. 93, no. 3, pp. 1285–1292, 2004, doi: 10.1002/app.20584.

[64] N. Brun *et al.*, “In Situ Monitoring of Styrene Polymerization Using Raman Spectroscopy. Multi-Scale Approach of Homogeneous and Heterogeneous Polymerization Processes,” *J. Raman Spectrosc.*, vol. 44, no. 6, pp. 909–915, 2013, doi: 10.1002/jrs.4279.

[65] H.-T. Chiu and S.-C. Chen, “Curing Reaction of Unsaturated Polyesters Modified with DCPD,” *J. Polym. Res.*, vol. 8, no. 3, pp. 183–190, 2001.

[66] C. Serré, M. Vayer, R. Erre, N. Boyard, and C. Ollive, “Atomic Force Microscopy, a Powerful Tool to Study Blend Morphologies Based on Polyester Resins,” *J. Mater. Sci.*, vol. 36, no. 1, pp. 113–122, 2001, doi: 10.1023/A:1004859303504.

[67] B. W. a Sherar, P. G. Keech, Z. Qin, F. King, and D. W. Shoesmith, “Nominally Anaerobic Corrosion of Carbon Steel in Near-Neutral PH Saline Environments,” *Corrosion*, vol. 66, pp. 0450011–04500111, 2010, doi: 10.5006/1.3381566.

[68] “BS EN 10130:2006 Cold Rolled Low Carbon Steel Flat Products for Cold Forming — Technical Delivery Conditions.” British Standards Institution, 2006.

[69] H. E. Townsend, “Effects of Alloying Elements on the Corrosion of Steel in Industrial Atmospheres,” *Corrosion*, vol. 57, no. 6, pp. 497–501, 2001.

[70] M. Morcillo, D. De la Fuente, I. Díaz, and H. Cano, “Atmospheric Corrosion of Mild Steel,” *Rev. Metal.*, vol. 47, no. 5, pp. 426–444, 2011, doi: 10.3989/revmetalm.1125.

[71] D. Bayliss and D. H. Deacon, *Steelwork Corrosion Control*, Second. Taylor & Francis, 2002.

[72] N. R. Smart, D. J. Blackwood, and L. Werme, “Anaerobic Corrosion of Carbon Steel and Cast

Iron in Artificial Groundwaters: Part 1—Electrochemical Aspects," *Corrosion*, vol. 58, no. 7, pp. 547–559, Jul. 2002, doi: 10.5006/1.3277646.

[73] D. R. Lide and H. Frederikse, Eds., *Handbook of Chemistry and Physics*, Student Ed. CRC Press Inc, 1996.

[74] C. Edeleanu, "Corrosion Control by Anodic Protection," *Platin. Met. Rev.*, vol. 4, no. 3, pp. 86–91, 1960.

[75] C. Wagner, "Contribution to the Theory of Cathodic Protection," *J. Electrochem. Soc.*, vol. 99, no. 1, p. 1, 1952, doi: 10.1149/1.2779653.

[76] P. Delahay and M. Pourbaix, "POTENTIAL-PH DIAGRAMS," *J. Chem. Educ.*, pp. 683–688, 1950.

[77] *ISO 12944-2 Paints and varnishes - Corrosion protection of steel structures by protective paint systems*, 2017th ed. International Organization for Standardization, 2017.

[78] W. H. J. Vernon, "A Laboratory Study of the Atmospheric Corrosion of Metals. Part II.-Iron: The Primary Oxide Film. Part III.-The Secondary Product or Rust (Influence of Sulphur Dioxide, Carbon Dioxide, and Suspended Particles on the Rusting of Iron)," *Trans. Faraday Soc.*, vol. 31, p. 1668, 1935, doi: 10.1039/tf9353101668.

[79] I. Matsushima, "Carbon Steel Corrosion by Seawater, Chapter 45," in *Uhlig's Corrosion Handbook*, 3rd ed., R. W. Revie, Ed. Wiley & Sons, 2011.

[80] G. Grundmeier, W. Schmidt, and M. Stratmann, "Corrosion Protection by Organic Coatings: Electrochemical Mechanism and Novel Methods of Investigation," *Electrochim. Acta*, vol. 45, no. 15–16, pp. 2515–2533, 2000, doi: 10.1016/S0013-4686(00)00348-0.

[81] M. W. Kendig and H. Leidheiser, "The Electrical Properties of Protective Polymer Coatings as Related to Corrosion of the Substrate," *J. Electrochem. Soc.*, vol. 123, p. 982, 1976, doi: 10.1149/1.2133017.

[82] C. H. Hare, "Corrosion Control of Steel By Organic Coatings," in *Uhlig's Corrosion Handbook*, 3rd ed., R. W. Revie, Ed. Wiley & Sons, 2011.

[83] T. P. Chou, C. Chandrasekaran, S. J. Limmer, S. Seraji, and Y. Wu, "Organic - Inorganic Hybrid Coatings for Corrosion Protection," *J. Non. Cryst. Solids*, vol. 290, pp. 153–162, 2001.

[84] J. E. O. Mayne, "How Paints Prevent Corrosion," *Anti-Corrosion Methods Mater.*, vol. 1, no. 8, pp. 286–290, 1954, doi: http://dx.doi.org/10.1108/eb018973 Downloaded.

[85] H. Hojo, K. Tsuda, and K. Ogasawara, "Form and Rate of Corrosion of Corrosion-Resistant FRP Resins," *Adv. Compos. Mater.*, vol. 1, no. 1, pp. 55–67, Jan. 1991, doi: 10.1163/156855191X00063.

[86] P. Moongkhamklang and S. . Taylor, "The Delineation of Ionic Pathways in Organic Coatings

Using a Molecular Probe Technique," *Prog. Org. Coatings*, vol. 46, no. 2003, pp. 259–265, 2003, doi: 10.1016/S0300-9440(02)00196-0.

[87] S. R. Taylor, F. Contu, R. Santhanam, and P. Suwanna, "The Use of Cationic Fluoroprobes to Characterize Ionic Pathways in Organic Coatings," *Prog. Org. Coatings*, vol. 73, no. 2–3, pp. 169–172, 2012, doi: 10.1016/j.porgcoat.2011.10.010.

[88] R. Norsworthy, "Coatings Used in Conjuction With Cathodic Protection – Shielding vs Non-Shielding Pipeline Coatings," in *Corrosion*, 2009, no. 09043, pp. 1–11.

[89] M. Nonnenmacher, M. P. O'Boyle, and H. K. Wickramasinghe, "Kelvin Probe Force Microscopy," *Appl. Phys. Lett.*, vol. 58, no. 25, p. 2921, Jun. 1991, doi: 10.1063/1.105227.

[90] R. a Dickie, J. S. Hammond, and J. W. Holubka, "Interfacial Chemistry of the Corrosion of Polybutadiene-Coated Steel," *Ind. Eng. Chem.*, vol. 20, pp. 339–343, 1981, doi: 10.1021/i300002a021.

[91] E. L. Koehler, "Technical Note: The Mechanism of Cathodic Disbondment of Protective Organic Coatings—Aqueous Displacement at Elevated PH," *Corrosion*, vol. 40, no. 1, pp. 5–8, 1984, doi: 10.5006/1.3579295.

[92] N. Sridhar, D. S. Dunn, and M. Seth, "Application of a General Reactive Transport Model to Predict Environment Under Disbonded Coatings," *Corros. Sci.*, no. July, pp. 598–613, 2001, doi: 10.5006/1.3290387.

[93] R. A. Dickie, "Paint Adhesion, Corrosion Protection, and Interfacial Chemistry," *Prog. Org. Coatings*, vol. 25, no. 1, pp. 3–22, 1994, doi: 10.1016/0300-9440(94)00500-1.

[94] S. B. Lyon, R. Bingham, and D. J. Mills, "Advances in Corrosion Protection by Organic Coatings: What We Know and What We Would like to Know," *Prog. Org. Coatings*, 2016, doi: 10.1016/j.porgcoat.2016.04.030.

[95] W. . van Ooij, A. Sabaata, and A. D. Appelhans, "Application of Surface Analysis Techniques to the Study of Paint/Matal Interfaces Related to Adhesion and Corrosion Performance," *Surf. Interface Anal.*, vol. 17, no. 7, pp. 403–420, 1991.

[96] "ISO 21809-3 Petroleum and Natural Gas Industries — External Coatings for Buried or Submerged Pipelines Used in Pipeline Transportation Systems — Part 3: Field Joint Coatings," vol. 2016. International Organization for Standardization, 2016.

[97] J. L. Martín, "Kinetic Analysis of an Asymmetrical DSC Peak in the Curing of an Unsaturated Polyester Resin Catalysed with MEKP and Cobalt Octoate," *Polymer (Guildf).*, vol. 40, no. 12, pp. 3451–3462, Jun. 1999, doi: 10.1016/S0032-3861(98)00556-4.

[98] X. Ramis and J. M. Salla, "Time-Temperature Transformation (TTT) Cure Diagram of an Unsaturated Polyester Resin," *J. Polym. Sci. Part B Polym. Phys.*, vol. 35, no. 2, pp. 371–388, 1997, doi: 10.1002/(SICI)1099-0488(19970130)35:2<371::AID-POLB13>3.3.CO;2-6.

[99] *Regulation (EC) 1278/2008 of the European Parliament and of the council on the*

classification, labelling and packaging of substances and mixtures, vol. L 353, no. 31.12.2008. European Union, 2008, pp. 1–2023.

[100] Transocean Coatings, "Surface Preparation," *Transocean*, 2010. http://www.transocean-coatings.com/en/services/general-information/ (accessed Jul. 15, 2016).

[101] "Chlor-Rid." http://www.chlor-rid.com/ (accessed May 20, 2020).

[102] "HoldTight." https://holdtight.com/ (accessed May 20, 2020).

[103] J. Ahlström, J. Tidblad, L. Tang, B. Sederholm, and S. Leijonmarck, "Electrochemical Properties of Oxide Scale on Steel Exposed in Saturated Calcium Hydroxide Solutions with or without Chlorides," *Int. J. Corros.*, vol. 2018, 2018, doi: 10.1155/2018/5623504.

[104] R. Naderi, M. Mahdavian, and a. Darvish, "Electrochemical Examining Behavior of Epoxy Coating Incorporating Zinc-Free Phosphate-Based Anticorrosion Pigment," *Prog. Org. Coatings*, vol. 76, no. 1, pp. 302–306, Jan. 2013, doi: 10.1016/j.porgcoat.2012.09.026.

[105] "NACE Coating Inspector Program Level 1 Student Manual." NACE International, 2013.

[106] "TG 546 Soluble Salts Based on Service Environments."

[107] "TEG 423X Non-Visible, Non-Water Soluble Contaminants Affecting Corrosion Protection."

[108] "Assessing the Risk of Coating Failure from Residual Soluble Salts," *Materials Performance*, 2020. http://www.materialsperformance.com/articles/coating-linings/2017/03/assessing-the-risk-of-coating-failure-from-residual-soluble-salts (accessed May 20, 2020).

[109] C. H. Hare, "Blistering of Paint Films on Metal, Part 1: Osmotic Blistering," *J. Prot. Coatings Linings*, no. February, pp. 45–63, 1998.

[110] D. de la Fuente, B. Chico, and M. Morcillo, "Soluble Salts and the Durability of Paint Coatings: A New Laboratory Method for Dosing Chlorides and Sulphates over Steel Surfaces," *Anti-Corrosion Methods Mater.*, vol. 50, no. 3, pp. 208–216, 2003, doi: 10.1108/00035590310471787.

[111] M. S. Schilling, "Osmotic Blistering - Coatings under Pressure," 2009, no. 09023, pp. 1–29.

[112] R. Kean and K. Davies, Eds., "Cathodic Protection." National Physical Laboratory, [Online]. Available: http://www.npl.co.uk/science-technology/advanced-materials/national-corrosion-service/publications/corrosion-guides.

[113] J. E. O. Mayne, J. Menter, and M. Pryor, "The Mechanism of Inhibition of the Corrosion of Iron by Sodium Hydroxide Solution," *J. Chem. Soc.*, pp. 3229–3236, 1950.

[114] H. Leidheiser, "Towards a Better Understanding of Corrosion Beneath Organic Coatings.," *Corrosion*, vol. 39, pp. 189–201, 1983, doi: 10.5006/1.3580835.

[115] J. Thomas and G. Hinds, "The Electrochemistry of Corrosion," National Physical Laboratory. [Online]. Available: orrosion-service/publications/corrosion-guides.

[116] P. Taheri, J. H. W. De Wit, H. Terryn, and J. M. C. Mol, "In Situ Study of Buried Metal-

Polymer Interfaces Exposed to an Aqueous Solution by an Integrated ATR-FTIR and Electrochemical Impedance Spectroscopy System," *J. Phys. Chem. C*, vol. 117, no. 40, pp. 20826–20832, 2013, doi: 10.1021/jp409288a.

[117] S. H. Mansour, E. Gomaa, and I. K. Bishay, "Effect of Metal Type and Content on Mechanical, Electrical and Free-Volume Properties of Styrenated Polyesters," *J. Mater. Sci.*, vol. 42, no. 20, pp. 8473–8480, 2007, doi: 10.1007/s10853-007-1762-z.

[118] G. Binnig and H. Rohrer, "Scanning Tunneling Microscope," Aug. 10, 1982.

[119] G. Binnig, C. F. Quate, and C. Gerber, "Atomic Force Microscopy," *Phys. Rev. Lett.*, vol. 56, no. 9, p. 930, 1986.

[120] "Agilent Technologies 5500 Scanning Probe Microscope User's Guide," no. Rev B. Agilent Technologies, 2008.

[121] C. M. Mate, G. M. McClelland, R. Erlandsson, and S. Chiang, "Atomic-Scale Friction of a Tungsten Tip on a Graphite Surface," *Phys. Rev. Lett.*, vol. 59, no. 17, pp. 1942–1946, 1987, [Online]. Available: https://journals.aps.org/prl/abstract/10.1103/PhysRevLett.59.1942.

[122] B. Cappella and G. Dietler, "Force-Distance Curves by Atomic Force Microscopy," *Surf. Sci. Rep.*, vol. 34, no. 1–3, pp. 1–104, 1999, doi: 10.1016/S0167-5729(99)00003-5.

[123] "A Practical Guide to AFM Force Spectroscopy and Data Analysis." JPK Instruments, pp. 1–8.

[124] "Advanced Force Distance Curves," no. version 1.0. AFM Workshop, pp. 1–2, [Online]. Available: http://www.afmworkshop.com/afm-advanced-force-distance-curves.html.

[125] H. Takano, J. R. Kenseth, S. S. Wong, J. C. O'Brien, and M. D. Porter, "Chemical and Biochemical Analysis Using Scanning Force Microscopy," *Chem. Rev.*, vol. 99, no. 515, pp. 2845–90, 1999, doi: 10.1021/cr9801317.

[126] R. N. Jagtap and a. H. Ambre, "Overview Literature on Atomic Force Microscopy (AFM): Basics and Its Important Applications for Polymer Characterization," *Indian J. Eng. Mater. Sci.*, vol. 13, no. 4, pp. 368–384, 2006.

[127] H.-J. Butt, B. Cappella, and M. Kappl, "Force Measurements with the Atomic Force Microscope: Technique, Interpretation and Applications," *Surf. Sci. Rep.*, vol. 59, no. 1–6, pp. 1–152, Oct. 2005, doi: 10.1016/j.surfrep.2005.08.003.

[128] "Windsor Scientific AFM Probe Catalogue." http://afm-probes.windsorscientific.co.uk/ (accessed Sep. 25, 2015).

[129] G. K. H. Pang, K. Z. Baba-Kishi, and a. Patel, "Topographic and Phase-Contrast Imaging in Atomic Force Microscopy," *Ultramicroscopy*, vol. 81, pp. 35–40, 2000, doi: 10.1016/S0304-3991(99)00164-3.

[130] Y. Martin, C. C. Williams, H. K. Wickramasinghe, and W. Martin, Williams, "Atomic Force Microscope–Force Mapping and Profiling on a Sub 100-Å Scale," *J. Appl. Phys.*, vol. 61, no.

10, p. 4723, May 1987, doi: 10.1063/1.338807.

[131] S. R. Cohen and A. Bitler, “Use of AFM in Bio-Related Systems,” *Curr. Opin. Colloid Interface Sci.*, vol. 13, no. 5, pp. 316–325, 2008, doi: 10.1016/j.cocis.2008.02.002.

[132] D. Raghavan, X. Gu, T. Nguyen, and M. Vanlandingham, “Characterization of Chemical Heterogeneity in Polymer Systems Using Hydrolysis and Tapping-Mode Atomic Force Microscopy,” *J. Polym. Sci. Part B Polym. Phys.*, vol. 39, pp. 1460–1470, 2001.

[133] X. Gu, D. Raghavan, T. Nguyen, M. . VanLandingham, and D. Yebassa, “Characterization of Polyester Degradation Using Tapping Mode Atomic Force Microscopy: Exposure to Alkaline Solution at Room Temperature,” *Polym. Degrad. Stab.*, vol. 74, no. 1, pp. 139–149, Jan. 2001, doi: 10.1016/S0141-3910(01)00138-0.

[134] Y. Martin, D. W. Abraham, and H. K. Wickramasinghe, “High-Resolution Capacitance Measurement and Potentiometry by Force Microscopy,” *Appl. Phys. Lett.*, vol. 52, no. 13, pp. 1103–1105, 1988, doi: 10.1063/1.99224.

[135] G. Neubauer, S. R. Cohen, G. M. McClelland, D. Horne, and C. M. Mate, “Force Microscopy with a Bidirectional Capacitance Sensor,” *Rev. Sci. Instrum.*, vol. 61, no. 9, pp. 2296–2308, 1990, doi: 10.1063/1.1141354.

[136] V. Palermo, M. Palma, and P. Samorì, “Electronic Characterization of Organic Thin Films by Kelvin Probe Force Microscopy,” *Adv. Mater.*, vol. 18, no. 2, pp. 145–164, Jan. 2006, doi: 10.1002/adma.200501394.

[137] T. Takahashi and S. Ono, “Tip-to-Sample Distance Dependence of an Electrostatic Force in KFM Measurements.,” *Ultramicroscopy*, vol. 100, no. 3–4, pp. 287–92, Aug. 2004, doi: 10.1016/j.ultramic.2004.01.017.

[138] H. O. Jacobs, P. Leuchtmann, O. J. Homan, and A. Stemmer, “Resolution and Contrast in Kelvin Probe Force Microscopy,” *J. Appl. Phys.*, vol. 84, no. 3, pp. 1168–1173, 1998.

[139] “Qantitative Surface Potential Measurement Using KFM : Effects of Imaging Parameters and Experimental Conditions.” Keysight Technologies, pp. 1–4, 2014.

[140] T. Glatzel, S. Sadewasser, and M. C. Lux-Steiner, “Amplitude or Frequency Modulation-Detection in Kelvin Probe Force Microscopy,” *Appl. Surf. Sci.*, vol. 210, no. 1–2, pp. 84–89, 2003, doi: 10.1016/S0169-4332(02)01484-8.

[141] G. M. Sacha, E. Sahagún, and J. J. Sáenz, “A Method for Calculating Capacitances and Electrostatic Forces in Atomic Force Microscopy,” *J. Appl. Phys.*, vol. 101, no. 2, p. 024310, 2007, doi: 10.1063/1.2424524.

[142] S. Hudlet, M. Saint Jean, C. Guthmann, and J. Berger, “Evaluation of the Capacitive Force between an Atomic Force Microscopy Tip and a Metallic Surface,” *Eur. Phys. J. B - Condens. Matter Complex Syst.*, vol. 2, no. 1, pp. 5–10, 1998, doi: 10.1007/s100510050219.

[143] S. R. Taylor, “Incentives for Using Local Electrochemical Impedance Methods in the Investigation of Organic Coatings,” *Prog. Org. Coatings*, vol. 43, pp. 141–148, 2001, doi: 10.1016/S0300-9440(01)00183-7.

[144] Y. Liu, J. He, O. Kwon, and D.-M. Zhu, “Probing Local Surface Conductance Using Current Sensing Atomic Force Microscopy.,” *Rev. Sci. Instrum.*, vol. 83, no. 1, 2012, doi: 10.1063/1.3673476.

[145] J. Zhao and K. Uosaki, “Dielectric Properties of Organic Monolayers Directly Bonded on Silicon Probed by Current Sensing Atomic Force Microscope,” *Appl. Phys. Lett.*, vol. 83, no. 10, p. 2034, 2003, doi: 10.1063/1.1609237.

[146] W. Deng, G.-M. Zhang, M. F. Murphy, F. Lilley, D. M. Harvey, and D. R. Burton, “Analysis of Dynamic Cantilever Behavior in Tapping Mode Atomic Force Microscopy,” *Microsc. Res. Tech.*, vol. 78, no. 10, pp. 935–946, 2015, doi: 10.1002/jemt.22558.

[147] D. Michel, S. Kopp-Marsaudon, and J. P. Aimé, “Tribology of a Polystyrene Polymer Film Investigated with an AFM,” *Tribol. Lett.*, vol. 4, no. 1, pp. 75–80, 1998, doi: 10.1023/A:1019130516466.

[148] “Elcometer Coating Thickness Gauge.” https://www.elcometer.com/en/coating-thickness-gauge.html (accessed May 16, 2021).

[149] “How Sample Preparation Can Help Sputter Coating for SEM?” https://www.azom.com/article.aspx?ArticleID=17025 (accessed Sep. 14, 2020).

[150] S. Ravi-Kumar, B. Lies, X. Zhang, H. Lyu, and H. Qin, “Laser Ablation of Polymers: A Review,” *Polym. Int.*, vol. 68, no. 8, pp. 1391–1401, 2019, doi: 10.1002/pi.5834.

[151] N. S. Sangaj and V. C. Malshe, “Permeability of Polymers in Protective Organic Coatings,” *Prog. Org. Coatings*, vol. 50, no. 1, pp. 28–39, 2004, doi: 10.1016/j.porgcoat.2003.09.015.

[152] J. Eiler, S. B. Simonsen, D. Hansen, B. Bingöl, K. Hansen, and E. Thormann, “Water Transport in Polymer Composites through Swelling-Induced Networks of Hydrogel Particles,” *Soft Matter*, vol. 16, no. 35, pp. 8254–8261, 2020, doi: 10.1039/d0sm01103g.

[153] B. Sarkar, M. Jaiswal, and D. K. Satapathy, “Swelling Kinetics and Electrical Charge Transport in PEDOT:PSS Thin Films Exposed to Water Vapor,” *J. Phys. Condens. Matter*, vol. 30, no. 22, 2018, doi: 10.1088/1361-648X/aabe51.

[154] P. Eisenberg, J. C. Lucas, and R. J. J. Williams, “Unsaturated Polyesters: Influence of the Molar Mass on the Cure with Styrene and the Properties of the Resulting Networks,” *J. Appl. Polym. Sci.*, vol. 65, no. 4, pp. 755–760, Jul. 1997, doi: 10.1002/(SICI)1097-4628(19970725)65:4<755::AID-APP13>3.3.CO;2-N.

[155] E. Richaud and J. Verdu, *Aging behavior and modelling studies of unsaturated polyester resin and unsaturated polyester resin-based blends*. Elsevier Inc., 2019.

[156] P. Nogueira *et al.*, “Effect of Water Sorption on the Structure and Mechanical Properties of

an Epoxy Resin System," *J. Appl. Polym. Sci.*, vol. 80, no. 1, pp. 71–80, 2001, doi: 10.1002/1097-4628(20010404)80:1<71::AID-APP1077>3.0.CO;2-H.

[157] D. Turnbull and M. H. Cohen, "Free-Volume Model of the Amorphous Phase: Glass Transition," *J. Chem. Phys.*, vol. 34, no. 1, pp. 120–125, Jan. 1961, doi: 10.1063/1.1731549.

[158] S.-B. B. Lee, T. J. J. Rockett, and R. D. D. Hoffman, "Interactions of Water with Unsaturated Polyester, Vinyl Ester and Acrylic Resins," *Polymer (Guildf).*, vol. 33, no. 17, pp. 3691–3697, Jan. 1992, doi: 10.1016/0032-3861(92)90657-I.

[159] D. de la Fuente, M. Bohm, C. Houyoux, M. Rohwerder, and M. Morcillo, "The Settling of Critical Levels of Soluble Salts for Painting," *Prog. Org. Coatings*, vol. 58, no. 1, pp. 23–32, 2007, doi: 10.1016/j.porgcoat.2006.11.003.

[160] M. Abder-Razzaq, D. W. Auckland, and B. R. Varlow, "Investigation of the Factors Governing Water Absorption in HV Composite Insulation," *IEEE Trans. Dielectr. Electr. Insul.*, vol. 5, no. 6, pp. 922–928, 1998, doi: 10.1109/94.740777.

[161] S. Morsch, S. Lyon, P. Greensmith, S. D. Smith, and S. R. Gibbon, "Mapping Water Uptake in Organic Coatings Using AFM-IR," *Faraday Discuss.*, vol. 180, pp. 527–542, 2015, doi: 10.1039/c4fd00229f.

[162] H. W. Starkweather, "Some Aspects of Water Clusters in Polymers," *Macromolecules*, vol. 8, no. 4, pp. 476–479, 1975, doi: 10.1021/ma60046a020.

[163] M. Kawagoe, Y. Doi, N. Fuwa, T. Yasuda, and K. Takata, "Effects of Absorbed Water on the Interfacial Fracture between Two Layers of Unsaturated Polyester and Glass," *J. Mater. Sci.*, vol. 36, no. 21, pp. 5161–5167, 2001, doi: 10.1023/A:1012437626988.

[164] L. A. McDonough, V. Chikan, Z. Hwan Kim, S. R. Leone, and W. D. Hinsberg, "Fourier Transform Infrared Spectroscopy Studies of Water-Polymer Interactions in Chemically Amplified Photoresists," *J. Vac. Sci. Technol. B Microelectron. Nanom. Struct.*, vol. 23, no. 2, p. 344, 2005, doi: 10.1116/1.1861034.

[165] T. Souier, F. Martin, C. Bataillon, and J. Cousty, "Local Electrical Characteristics of Passive Films Formed on Stainless Steel Surfaces by Current Sensing Atomic Force Microscopy," *Appl. Surf. Sci.*, vol. 256, no. 8, pp. 2434–2439, 2010, doi: 10.1016/j.apsusc.2009.10.083.

[166] "Article 601." www.azom.com (accessed Sep. 24, 2019).

[167] M. G. Rakotomanana, I. A. Rakotomanana, D. A. Rakotomanana, C. R. Rakotomanana, and J. A. Randriamorasata, "Theoretical Variation of the Elastic Constraints of a Unidirectional Bamboo/Polyester Lamina Composite According to the Orientation of the Fibers," *Int. J. Adv. Res. Innov. Ideas Educ.*, vol. 5, no. 5, pp. 279–287, 2019.

[168] "ASTM D149 Standard Test Method for Dielectric Breakdown Voltage and Dielectric Strength of Solid Electrical Insulating Materials at Commercial Power Frequencies." ASTM.

[169] D. Halliday, R. Resnick, and J. Walker, *Fundamentals of Physics*, Fifth. John Wiley & Sons, Inc, 1997.

[170] "Magnetic Carriers." [Online]. Available: https://archive.ifla.org/VI/6/dswmedia/en/pdf/txt_magn.pdf.

[171] R. Razavi, Y. Zare, and K. Y. Rhee, "The Roles of Interphase and Filler Dimensions in the Properties of Tunneling Spaces between CNT in Polymer Nanocomposites," *Polym. Compos.*, vol. 40, no. 2, pp. 801–810, 2019, doi: 10.1002/pc.24739.

[172] R. W. Warfield and M. C. Petree, "Electrical Resistivity of Polymers," *SPE Trans.*, vol. April, pp. 80–85, 1961.

[173] L. S. Faiq and Z. F. Attiyah, "Thermo-Physical and Mechanical Properties of Unsaturated Polyester / Cobalt Ferrite Composites," vol. 23, no. 4, pp. 88–99, 2017.

[174] G. Reiter and S. Napolitano, "Possible Origin of Thickness-Dependent Deviations from Bulk Properties of Thin Polymer Films," *J. Polym. Sci. Part B-Polymer Phys.*, vol. 48, pp. 2544–2547, 2010, doi: 10.1002/polb.22134.

[175] S. Kim and J. M. Torkelson, "Distribution of Glass Transition Temperatures in Free-Standing Nanoconfined Polystyrene Films: A Test of de Gennes Sliding Motion Mechanism," *Macromolecules*, vol. 44, no. 11, pp. 4546–4553, 2011, doi: 10.1021/ma200617j.

[176] K. Seo, M. Kim, and D. H. Kim, "Re-Derivation of Young's Equation, Wenzel Equation, and Cassie-Baxter Equation Based on Energy Minimization," in *Surface Energy*, InTech, 2015.

[177] A. J. B. Milne and A. Amirfazli, "The Cassie Equation: How It Is Meant to Be Used," *Adv. Colloid Interface Sci.*, vol. 170, no. 1–2, pp. 48–55, 2012, doi: 10.1016/j.cis.2011.12.001.

[178] E. Bormashenko, "Why Does the Cassie-Baxter Equation Apply?," *Colloids Surfaces A Physicochem. Eng. Asp.*, vol. 324, no. 1–3, pp. 47–50, 2008, doi: 10.1016/j.colsurfa.2008.03.025.